



**Tiago Lima d'Albuquerque e Castro**

**Elliptical curve method for fatigue life  
prediction of structural steels under  
multiaxial loadings**

**Tese de Doutorado**

Thesis presented to the Programa de Pós-graduação em Engenharia de Materiais e de Processos Químicos e Metalúrgicos of PUC-Rio in partial fulfillment of the requirements for the degree of Doutor em Engenharia de Materiais e de Processos Químicos e Metalúrgicos.

Advisor: Prof. Marcos Venicius Soares Pereira

Rio de Janeiro  
April 2023



**Tiago Lima d'Albuquerque e Castro**

**Elliptical curve method for fatigue life prediction of structural steels under multiaxial loadings**

Thesis presented to the Programa de Pós-graduação em Engenharia de Materiais e de Processos Químicos e Metalúrgicos of PUC-Rio in partial fulfillment of the requirements for the degree of Doutor em Engenharia de Materiais e de Processos Químicos e Metalúrgicos. Approved by the Examination Committee.

**Prof. Dr.-Ing. Marcos Venicius Soares Pereira**

**Advisor**

Departamento de Engenharia Química e de Materiais - PUC-Rio

**Ph.D. Paulo José da Silva Tavares**

INEGI – University of Porto

**Prof. Ph.D. José Alexander Araújo**

Departamento de Engenharia Mecânica - UnB

**Dr. Arnaldo Freitas Camarão**

SAE Brasil

**Ph.D. Fathi Aref Ibrahim Darwish**

Pesquisador Autônomo

Rio de Janeiro, 25<sup>th</sup> April 2023.

All rights reserved. Total or partial reproduction of the work without authorisation of the university, the author and adviser are strictly forbidden.

### **Tiago Lima d'Albuquerque e Castro**

Received both bachelor's degree in electrical engineering with emphasis in electronics (2011) and master's degree in materials science and engineering (2019) from Pontifícia Universidade Católica do Rio de Janeiro.

#### Bibliographic data

Castro, Tiago Lima d'Albuquerque e

Elliptical curve method for fatigue life prediction of structural steels under multiaxial loadings / Tiago Lima d'Albuquerque e Castro; adviser: Marcos Venicius Soares Pereira. – 2023.

96 f. ; 30 cm

Tese (doutorado)–Pontifícia Universidade Católica do Rio de Janeiro, Departamento de Engenharia Química e de Materiais, 2023.

Inclui bibliografia

1. Engenharia Química e de Materiais – Teses. 2. Fadiga de alto ciclo. 3. Carregamentos combinados de flexão e torção. 4. Critérios baseados no plano crítico. 5. Condições síncronas de carregamento em fase e fora de fase. 6. Eixo virabrequim. I. Pereira, Marcos Venicius Soares. II. Pontifícia Universidade Católica do Rio de Janeiro. Departamento de Engenharia Química e de Materiais. III. Título.

CDD: 620.11

## **Acknowledgements**

I would like to express my sincere gratitude to my adviser, Marcos Pereira, for his invaluable guidance and support. His expertise and encouragement helped me to complete this research and write this thesis.

I would also like to thank Paulo Tavares, José Alexander Araújo, Arnaldo Camarão and Fathi Darwish for serving on my thesis examination committee, as well as for providing helpful feedback and suggestions.

I am grateful to Pontifícia Universidade Católica do Rio de Janeiro for the opportunity of conducting my research and for all the resources and support that the university and my department have provided. I would also like to acknowledge and express my gratitude to CAPES and FAPERJ for the funding and financial support.

I am deeply thankful to my family, Tânia, José, Tatiana and Bruno, for their love and encouragement during this process. I am also extremely grateful to Rayane, my love, for being part of my life, whose affection and solid companionship were decisive for the development of this work.

Furthermore, I thank my friends and colleagues Thiago Peixoto, Francisco José and Maria Clara and Lucas Araujo for all the time we have been working together and for your always valuable contributions. This gratitude is extended to all my colleagues at University of Brasília, for providing me the opportunity of conducting a large set of experiments in their lab, as well as to everyone who has been there for me emotionally and intellectually throughout this journey.

This study was financed in part by the Coordenação de Aperfeiçoamento de Pessoal de Nível Superior - Brasil (CAPES) - Finance Code 001.

## Abstract

Castro, Tiago Lima d'Albuquerque e; Pereira, Marcos Venicius Soares (Advisor). **Elliptical curve method for fatigue life prediction of structural steels under multiaxial loadings**. Rio de Janeiro, 2023. 96p. Tese de Doutorado - Departamento de Engenharia Química e de Materiais, Pontifícia Universidade Católica do Rio de Janeiro.

A direct relation where fatigue life  $N_f$  can be determined as function of macroscopic normal and shear stress amplitudes  $\sigma_a$  and  $\tau_a$  is established. Using the Carpinteri & Spagnoli (C&S) criterion as a survey tool, elliptical level curves in the  $\sigma_a \times \tau_a$  domain were revealed and further generalised, providing means to determine the number of cycles to failure  $N_f$  for any given  $(\sigma_a, \tau_a)$  combination. Predictions obtained through the elliptical curve method (E) were compared to experimental observations, as well as to predictions obtained from adapted versions of popular fatigue criteria, namely Findley (F), Matake (M), McDiarmid (McD), Susmel & Lazzarin (S&L), Carpinteri & Spagnoli (C&S) and Papadopoulos (P). The proposed model delivered predictions in fair agreement with experimental observations and its predictive capability was seen to be the best among all the considered criteria. Finally, a slight bias towards conservativeness was attenuated with the introduction of an adjusting parameter, further improving the predictive capability of the model.

## Keywords

High-cycle fatigue; Combined bending and torsion loadings; Critical plane-based criteria; Synchronous in-phase and out-of-phase loadings; Crankshaft; Thermoelectric power plants

## Resumo

Castro, Tiago Lima d'Albuquerque e; Pereira, Marcos Venicius Soares (orientador). **Método da curva elíptica para previsão da vida em fadiga de aços estruturais sob carregamentos multiaxiais**. Rio de Janeiro, 2023. 96p. Tese de Doutorado - Departamento de Engenharia Química e de Materiais, Pontifícia Universidade Católica do Rio de Janeiro.

Uma relação direta onde a vida em fadiga  $N_f$  pode ser descrita como função das amplitudes macroscópicas de tensão normal e cisalhante,  $\sigma_a$  e  $\tau_a$ , é obtida. Utilizando o critério de Carpinteri & Spagnoli (C&S) como uma ferramenta de inspeção, foram obtidas curvas de nível elípticas sobre um domínio  $\sigma_a \times \tau_a$ . A expressão das curvas de nível obtidas foi generalizada, proporcionando uma ferramenta capaz de prever o número de ciclos para falha  $N_f$  associado a qualquer combinação  $(\sigma_a, \tau_a)$ . As previsões obtidas através do método da curva elíptica foram comparadas às observações experimentais, bem como a previsões obtidas a partir de versões adaptadas de modelos consagrados na literatura, a saber: Findley (F), Matake (M), McDiarmid (McD), Susmel & Lazzarin (S&L), Carpinteri & Spagnoli (C&S) e Papadopoulos (P). O modelo proposto forneceu previsões em boa concordância com as observações experimentais, e sua capacidade de avaliar o comportamento em fadiga se revelou o melhor dentro todos os critérios considerados. Por fim, uma leve tendência conservadora do modelo foi atenuada através da introdução de um parâmetro de ajuste, melhorando ainda mais sua capacidade de avaliação de comportamento em fadiga.

## Palavras-chave

Fadiga de alto ciclo; carregamentos combinados de flexão e torção; critérios baseados no plano crítico; condições síncronas de carregamento em fase e fora de fase; eixo virabrequim; usinas termoelétricas

# Contents

<b>1. Introduction.....</b>	<b>8</b>
1.1. Background and mechanical component description .....	8
1.2. Preliminary considerations on stress-based criteria .....	11
1.3. Motivation and objectives .....	12
<b>2. Overview of basic concepts .....</b>	<b>14</b>
2.1. Relevant concepts of tensor algebra .....	14
2.1.1. Vectors and bases .....	14
2.1.2. Index notation.....	15
2.1.3. Second-order tensors .....	17
2.1.4. Components of a vector and a second-order tensor .....	18
2.1.5. Product between tensors .....	19
2.1.6. Transpose tensor and change of basis.....	19
2.1.7. Dyadic product.....	22
2.2. Additional mathematical concepts.....	23
2.2.1. Considerations on several-variable function.....	23
2.2.2. Eigenvalues and eigenvectors.....	25
2.3. Relevant concepts of mechanical behaviour of solids.....	26
2.3.1. Cauchy's postulate.....	27
2.3.2. Cauchy's theorem .....	28
2.3.3. Principal stresses and spectral decomposition.....	36
2.3.4. Hydrostatic and deviatoric stresses.....	37
2.4. Relevant concepts of fatigue .....	38
2.4.1. Uniaxial fatigue .....	38
2.4.2. Multiaxial fatigue .....	41
<b>3. Methods .....</b>	<b>55</b>
3.1. Proposition of the elliptical curve method .....	55
3.2. Adaptation of other stress-based criteria for fatigue-life prediction...	57
3.3. Material and experimental approach .....	59
3.4. Influence of phase difference .....	62

<b>4. Results.....</b>	<b>65</b>
4.1. Uniaxial fatigue tests.....	65
4.2. Multiaxial fatigue predictions .....	66
<b>5. Discussion.....</b>	<b>71</b>
5.1. Adjusting parameter .....	73
5.2. Additional results and discussion .....	77
<b>6. Conclusions.....</b>	<b>79</b>
<b>Appendix I – Exemplifying the use of critical plane-based criteria.....</b>	<b>83</b>

## List of Figures

Figure 1 – Crankshafts used in the thermoelectric power plant environments .....	9
Figure 2 – Illustration of the crankshaft .....	10
Figure 3 – Firing sequence .....	10
Figure 4 – Crankshaft failure: (a) crack nucleation site and (b) crack extension .....	11
Figure 5 – (a) Detailed illustration of a crankpin journal; (b) generic crankshaft (source: turbosquid.com) .....	11
Figure 6 – Anticlockwise rotation of $\theta$ to the reference system .....	22
Figure 7 – Level curves relative to an arbitrary function .....	24
Figure 8 – (a) Contact and body forces; (b) equilibrium of part p due to internal forces $t$ .....	26
Figure 9 – Cauchy’s hypothesis .....	27
Figure 10 – (a) Entire solid in equilibrium; (b) part in equilibrium .....	28
Figure 11 – Forces acting on elementary volume (a) contact forces and (b) body forces .....	30
Figure 12 – Moments produced by body forces (a) general view and (b) top view .....	31
Figure 13 – Moments produced by normal forces (a) general view and (b) top view ...	32
Figure 14 – Moments produced by shear forces acting on z planes (a) general view and (b) top view .....	32
Figure 15 – Moments produced by shear forces acting on x and y planes (a) general view and (b) top view .....	33
Figure 16 – Solid body where part p and corresponding forces are evidenced .....	35
Figure 17 – Loading histories $\sigma(t)$ as sinusoidal curves, with and without mean stress .....	39
Figure 18 – Goodman plot .....	40
Figure 19 – Time-varying stresses acting on a small volume of material .....	41
Figure 20 – (a) Material plane $\Delta$ ; (b) Normal and shear stress vectors .....	42
Figure 21 – (a) Rotations applied to the reference system; (b) final orientation of the reference system .....	42
Figure 22 – Closed path described by the shear stress vector on material plane $\Delta$ within a loading cycle .....	45

Figure 23 – Determination of the shear stress amplitude: (a) MCC; (b) MRH .....	45
Figure 24 – (a) Drawback on shear stress amplitude estimation; (b) sensitivity to non-proportionality .....	46
Figure 25 – Positioning of the reference system relative to an hourglass specimen ....	47
Figure 26 – Material plane $\Delta$ and free surface of the specimen: (a) free view; (b) top view .....	48
Figure 27 - Critical plane orientation.....	51
Figure 28 – Solution to the modified C&S expression.....	53
Figure 29 – (a) Newton-Raphson method; (b) bisection method .....	54
Figure 30 – Elliptical level curve associated with a constant fatigue-life.....	56
Figure 31 – Adopted specimen geometry .....	<b>Error! Bookmark not defined.</b>
Figure 32 – Loading conditions selected for testing.....	61
Figure 33 – Influence of phase difference for a given constant fatigue-life .....	63
Figure 34 – Comparison of the predictive capability of $\beta$ -dependent and $\beta$ -independent criteria .....	64
Figure 35 – Resulting Wöhler curves and corresponding Basquin expressions.....	66
Figure 36 – Fatigue-life prediction compared to experimental observations .....	68
Figure 37 – Frequency histograms of the error indices obtained from each multiaxial fatigue criterion (data in Table 8).....	69
Figure 38 – Percentage of error indices located within the ranges of interest .....	73
Figure 39 – C, D and E shifted along constant $\tau_a/\sigma_a$ ratios, while A and G are held fixed.....	74
Figure 40 – Generic plot of a band-pass filter function both in linear and log scale .....	75
Figure 41 – Curve fitting of $H(s)$ using residues to obtain the corresponding values of $c_1$ and $c_2$ .....	77
Figure 42 – Life diagram and frequency history relative to the adjusted elliptical curve method .....	78

## List of Tables

Table 1 – Mechanical properties of the DIN 42CrMo4 steel.....	60
Table 2 – Selected stress amplitudes relative to the 40,000 cycle level curve.....	60
Table 3 – Additional loading conditions not associated with any particular $N_f$ .....	61
Table 4 – Stress levels as function of $\beta$ for a $\tau_a/\sigma_a$ ratio of 1 relative to a constant value of fatigue life.....	62
Table 5 – Stress levels $\beta$ corresponding to $90^\circ$ for a $\tau_a/\sigma_a$ ratio of 1.....	64
Table 6 – Results for uniaxial fully reversed tests.....	65
Table 7 – Comparison of predictions obtained via elliptical curve method vs. experimental results.....	67
Table 8 – Deviation of each prediction relative to its corresponding experimental observation.....	70
Table 9 – Statistics relative to each criterion.....	72
Table 10 – Residues obtained from the experiments associated with a 40,000 cycle fatigue-life.....	76
Table 11 – Error indices relative to the adjusted version of the elliptical curve method.....	77
Table 12 – Statistics relative to the adjusted version of the elliptical curve method....	78

## Nomenclature

$A$	Basquin's coefficient for fully reversed uniaxial normal testing condition
$A'$	Basquin's coefficient for fully reversed uniaxial shear testing condition
C&S	Carpinteri & Spagnoli's criterion
$c_1$	Constant for the adjusting parameter of the elliptical curve method
$c_2$	Constant for the adjusting parameter of the elliptical curve method
$C_a$	Shear stress amplitude acting on the critical plane
E	Elliptical curve method
F	Findley's criterion
$f^*$	Parameter for Findley's criterion
$f_{-1}$	Fatigue resistance limit for fully reversed uniaxial normal testing condition in the case of infinite fatigue life
$f'_{-1}$	Fatigue resistance limit for fully reversed uniaxial normal testing condition in the case of finite fatigue life
$G$	Function relating the number of cycles to failure to the normal and shear stress amplitudes
$H$	Adjusting parameter of the elliptical curve method
$I$	Error index measuring the deviation between predicted and experimentally observed fatigue life
$k$	Parameter for Findley's criterion
M	Matake's criterion
$m$	Basquin's exponent for fully reversed uniaxial normal testing condition
$m^*$	Basquin's exponent for fully reversed uniaxial shear testing condition
MCC	Minimum circumscribed circumference
McD	McDiarmid's criterion
MRH	Maximum rectangular hull
$N_0$	Reference number of loading cycles taken as $2 \times 10^6$ cycles
$N_a$	Normal stress amplitude acting on the critical plane
$N_f$	Number of cycles to failure
$N_{f,exp}$	Experimentally determined number of cycles to failure
$N_{f,th}$	Theoretically predicted number of cycles to failure
$N_m$	Mean normal stress acting on the critical plane
$N_{max}$	Maximum value attained by the normal stress acting on the critical plane
P	Papadopoulos' criterion
$s$	Ratio between shear and normal stress amplitudes
S&L	Susmel & Lazzarin's criterion
$t_{-1}$	Fatigue resistance limit for fully reversed uniaxial normal testing condition in the case of infinite fatigue life
$t'_{-1}$	Fatigue resistance limit for fully reversed uniaxial normal testing condition in the case of finite fatigue life
$\alpha$	Parameter for Papadopoulos' criterion
$\beta$	Phase difference between cyclic normal and shear stresses
$\Delta$	Generic material plane within the specimen
$\delta$	C&S
$\theta$	Euler's angle in spherical coordinates
$\mu$	Parameter for Matake's criterion
$\sigma_a$	Macroscopic normal stress amplitude
$\sigma_{H,max}$	Maximum value attained by the hydrostatic stress
$\sigma_u$	Ultimate tensile strength
$\sigma_y$	Yield strength
$\tau_a$	Macroscopic shear stress amplitude
$\varphi$	Euler's angle in spherical coordinates
$\varphi_c$	Euler's angle in spherical coordinates associated with the critical plane's orientation

## **1. Introduction**

Fatigue is a mechanism of failure where mechanical components accumulate damage due to the application of time-varying loads. Even though engineering designs are conceived to maintain structures within the elastic regime, defects and geometrical features of the components introduce stress concentrators that may locally raise stress levels, thus promoting fatigue damage. Considering that mechanical components such as railroad wheels, crankshafts, axles and turbine blades are subjected to cyclic loadings throughout long service lives, repetition of such stress levels contributes to accumulation of damage, eventually leading to crack nucleation [1], [2].

In engineering applications, mechanical components are commonly subjected to time-varying multiaxial stress-states. As such, evaluation of high cycle fatigue behaviour of metallic materials under time-varying multiaxial stresses can be achieved by using appropriate fatigue damage criteria. These criteria can be typically divided into three different groups: stress-based, strain-based and energy-based models [3]. While each group presents its own characteristics and applications, stress-based approach has been popularly adopted in high-cycle fatigue analysis. The large number of models pertaining to this approach can be typically classified into four divisions based on: empirical equivalent stress, stress invariants, average stress and critical plane stress. Several reviews of these models can be found in the literature [4]–[8].

### **1.1. Background and mechanical component description**

Fatigue failures of motor crankshafts operating in thermoelectric power plant environments are being recently reported, where some of the failures were revealed to take place within less than one year of operation. Since thermoelectric power corresponds to a significant share of the Brazilian energetic matrix [9], the ability to properly assess the fatigue behaviour of components as well as the capability of adequately designing against such phenomenon becomes of great importance.

The crankshafts in question (Fig. 1) are large components used to generate power from the combustion of fossil fuels. The energy released from the combustion reaction inside

the cylinder bores is converted into rotary motion, which is in turn further converted electromechanically into electrical power.



Figure 1 – Crankshafts used in the thermoelectric power plant environments

Such crankshafts present a total of ten crankpin journals, each one containing a couple of connecting rods. One extreme of the connecting rod is clamped to its corresponding crankpin journal while the other end is connected to its piston. The crankpin journals are offset to the main journal's centreline in such a way that, when the entire crankshaft is subjected to rotary motion, the crankpin journals revolve describing circles of their own.

Each crankpin journal is positioned according to a given angular position in order to establish a certain firing sequence, designed to better distribute the stresses along the crankshaft's length within a loading cycle. Fig. 2 illustrates the crankshafts in question evidencing the different angular position of the crankpin journals, each with their respective counterweights. The firing sequence is displayed in Fig. 3.

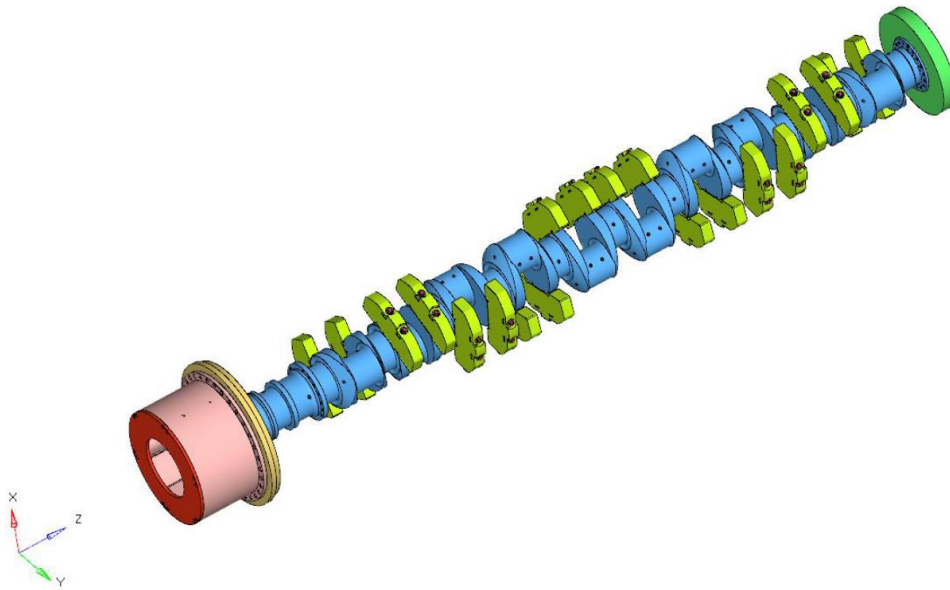


Figure 2 – Illustration of the crankshaft

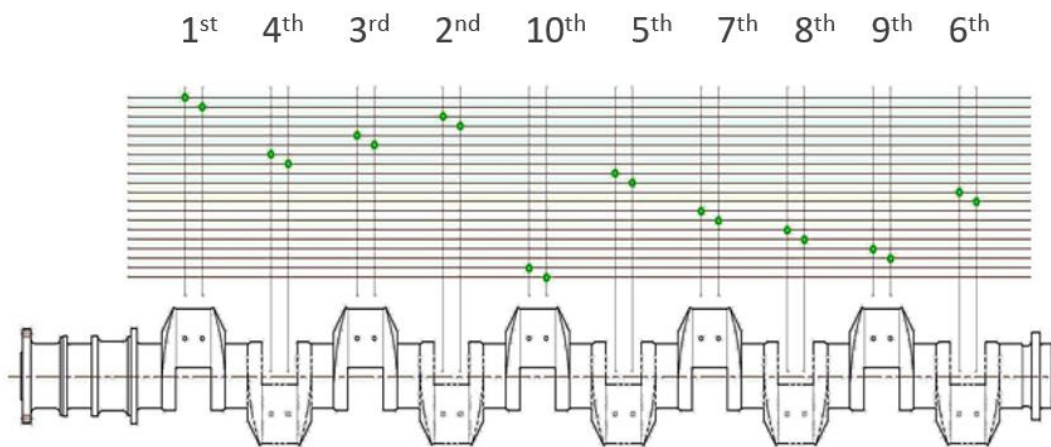


Figure 3 – Firing sequence

It was revealed that all the failed crankshafts presented similar cracking patterns, as all cracks were initiated at critical points of the crankpin journals where geometric features of the component introduced stress concentration, as depicted in Fig. 4. In addition, Fig. 5(a) further details the crankpin journals, evidencing the location of the critical points, while Fig. 5(b) exemplifies the aesthetics of a generic crankshaft, assembled with one connecting rod per crankpin journal.

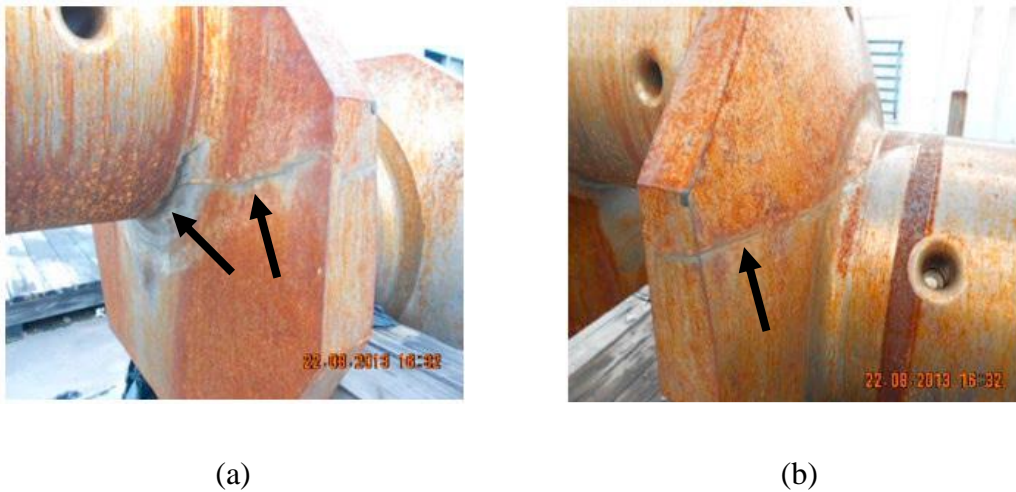


Figure 4 – Crankshaft failure: (a) crack nucleation site and (b) crack extension

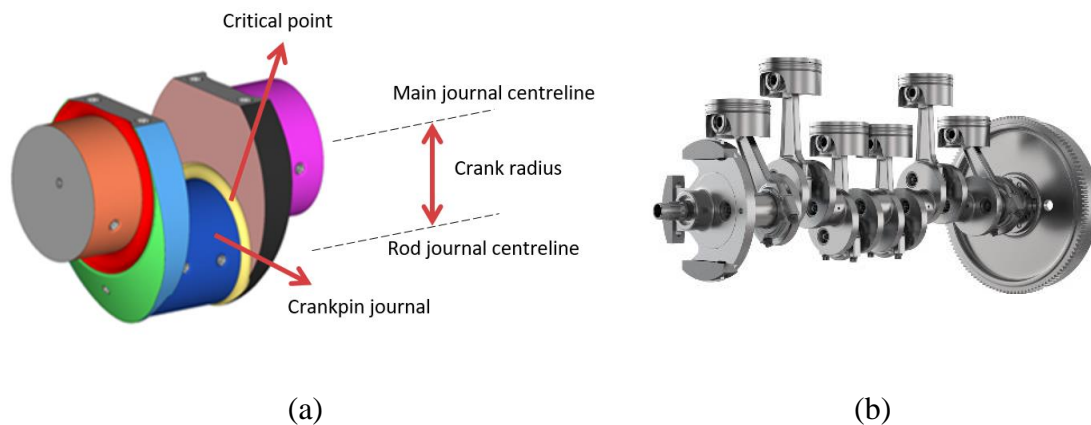


Figure 5 – (a) Detailed illustration of a crankpin journal; (b) generic crankshaft (source: turbosquid.com)

## 1.2. Preliminary considerations on stress-based criteria

As previously mentioned, stress-based criteria have been popularly used in light of infinite fatigue-life approach for assessing the fatigue behaviour of components that are expected to endure long service-lives. As such, critical plane-based models play an important role within the stress-based criteria group, hence justifying their application throughout this work.

In general terms, critical-plane stress-based criteria take into account loading histories and material properties to determine whether or not fatigue failures are to be expected. In this sense, attention is focused on guaranteeing a good margin of safety against failure by

admitting loading conditions in proximity with the fatigue resistance limit, above which fatigue failure can occur and below which fatigue life extends over a very high number of cycles (theoretically infinite). Some of the popular critical plane-based criteria were considered in this work, namely Findley (F) [10], Matake (M) [11], McDiarmid (McD) [12], Susmel & Lazzarin (S&L) [13] and Carpinteri & Spagnoli (C&S) [8]. Despite particular characteristics of each, all models are applicable in a similar manner: stresses must be computed for a large number of material planes in order to determine which plane experiences the greatest fatigue damage. Accordingly, only after determining the critical plane orientations and their corresponding stresses can the critical plane-based models be applied.

In addition to the critical plane-based criteria, the present work also takes into consideration the criterion proposed by Papadopoulos (P) [5], which is also a very well-established model. By adopting a mesoscopic scale approach, the criterion aims to evaluate the accumulated crystal plastic strain, thus being independent of critical plane determination. In contrast to critical plane-based models, Papadopoulos only takes into account the macroscopically applied loads and material properties to assess the fatigue behaviour of the component in question.

### **1.3. Motivation and objectives**

Although effective, the aforementioned models as described above are limited to assessing whether or not failures are to be expected, therefore lacking the ability of predicting the number of cycles endured by the component prior to its failure. In 2013, Carpinteri & Spagnoli proposed a modification to their own work, enabling their criterion to deliver fatigue-life predictions [14]. This was achieved by substituting in the model's expression the fixed values of fatigue resistance limits by the corresponding Basquin's expressions, which are dependent on the number of cycles to failure.

Nevertheless, the adapted version of the C&S criterion delivers a non-linear final expression that presents no analytical solution, which therefore must be solved numerically. Accordingly, it is to be remembered that all the previous steps required for the application of the C&S criterion, i.e., determination of critical plane and corresponding stresses, are still indispensable. Therefore, although feasible, fatigue-life

prediction as proposed by C&S may involve non-negligible efforts. In this sense, the proposal of a simpler fatigue-life prediction method becomes very desirable, especially if it reveals itself to be independent of critical plane determination.

A natural first step would be to verify whether it is possible to consider a macroscopic relation where the number of cycles to failure could be determined as function of the macroscopically applied stresses. Considering loading conditions where fully-reversed combined synchronous sinusoidal normal and shear stresses are applied to a specimen, one could verify if it is possible to equate the number of cycles to failure  $N_f$  to a function  $G(\sigma_a, \tau_a)$ , where  $\sigma_a$  and  $\tau_a$  respectively correspond to the nominal normal and shear stress amplitudes. As one would expect, obtaining function  $G$  is the main goal of the present work.

In order to verify such hypothesis, a good starting point would be to investigate the domain of such a function using the modified version of the C&S criterion as a survey tool. If successful, one may obtain a collection of coordinate points associated with a given constant fatigue-life, eventually building a level curve. Once such contour line is determined, it may be possible to further generalise such curve, allowing one to straight forwardly predict the number of cycles to failure  $N_f$  for any given  $(\sigma_a, \tau_a)$  combination without the need of critical plane determination.

## 2. Overview of basic concepts

### 2.1. Relevant concepts of tensor algebra

#### 2.1.1. Vectors and bases

Vectors are quantities with specified magnitude, direction and orientation in three-dimensional space, typically represented in minuscule bold-face roman symbols [15]. When a Euclidean vector space is taken into consideration, vectors in  $\mathbb{R}^3$  can be frequently arranged as a  $3 \times 1$  column matrix, as show in

$$[\mathbf{v}] = \begin{Bmatrix} v_1 \\ v_2 \\ v_3 \end{Bmatrix} \in \mathbb{R}^3, \quad (1)$$

where  $[\mathbf{v}]$  is addressed to as the matrix representation of  $\mathbf{v}$ . As one would expect, a vector in  $\mathbb{R}^3$  can be decomposed into a summation of three linearly independent vectors  $\mathbf{e}_1$ ,  $\mathbf{e}_2$  and  $\mathbf{e}_3$ , each multiplied by scale factors. This provides an algebraic representation of the vector  $\mathbf{v}$ , as given by [16]

$$\mathbf{v} = v_1 \mathbf{e}_1 + v_2 \mathbf{e}_2 + v_3 \mathbf{e}_3. \quad (2)$$

Accordingly, vector  $\mathbf{v}$  is therefore expressed in terms of the basis determined by  $\mathbf{e}_1$ ,  $\mathbf{e}_2$  and  $\mathbf{e}_3$ . The scalar quantities  $v_1$ ,  $v_2$  and  $v_3$  are the components of the vector  $\mathbf{v}$  in the same basis.

Vectors with unit magnitude are called unit vectors and three linearly independent vectors generate  $\mathbb{R}^3$ . Three mutually perpendicular unit vectors  $\mathbf{i}$ ,  $\mathbf{j}$  and  $\mathbf{k}$  constitute a right-handed orthonormal basis, provided that [15]

$$\mathbf{i} \times \mathbf{j} = \mathbf{k}, \quad \mathbf{j} \times \mathbf{k} = \mathbf{i}, \quad \mathbf{k} \times \mathbf{i} = \mathbf{j}, \quad (3)$$

$$(\mathbf{i} \times \mathbf{j}) \cdot \mathbf{k} = 1. \quad (4)$$

In order to obtain a more concise notation, any given basis  $\{\mathbf{e}_1, \mathbf{e}_2, \mathbf{e}_3\}$  will be henceforth addressed to as  $\{\mathbf{e}_i\}$ . Accordingly, the components are in turn addressed to as  $v_i$ , where the subscript  $i$  ranges from 1 to 3.

## 2.1.2. Index notation

### 2.1.2.1. Summation convention

The index notation aims to promote a more concise writing, which facilitates mathematical derivations that could otherwise be presented as long and repetitious in matrix representation. The notation is mainly based on the summation convention, where any repeated index implies a sum.

As such, vectors  $\mathbf{a}$  and  $\mathbf{b}$  can be represented using an abbreviated notation form, as given by [15]

$$\mathbf{a} = a_1 \mathbf{e}_1 + a_2 \mathbf{e}_2 + a_3 \mathbf{e}_3 = a_i \mathbf{e}_i \quad (5)$$

$$\mathbf{b} = b_j \mathbf{e}_j . \quad (6)$$

Any unrepeated index is a free index, and the final dimension of the quantity in question is associated with the number of free indices present in such quantity. Assume  $\mathbf{v}$  is a vector resulting from a linear transformation  $\mathbf{A}$  which receives the vector  $\mathbf{u}$  as input. In matrix representation, this operation would be presented as

$$\begin{Bmatrix} v_1 \\ v_2 \\ v_3 \end{Bmatrix} = \begin{pmatrix} A_{11} & A_{12} & A_{13} \\ A_{21} & A_{22} & A_{23} \\ A_{31} & A_{32} & A_{33} \end{pmatrix} \begin{Bmatrix} u_1 \\ u_2 \\ u_3 \end{Bmatrix}, \quad (7)$$

which would result in three independent expressions, as given by

$$v_1 = A_{11}u_1 + A_{12}u_2 + A_{13}u_3 \quad (8)$$

$$v_2 = A_{21}u_1 + A_{22}u_2 + A_{23}u_3 \quad (9)$$

$$v_3 = A_{31}u_1 + A_{32}u_2 + A_{33} . \quad (10)$$

Expressions (8)-(10) can be reduced to

$$v_1 = A_{1j}u_j \quad (11)$$

$$v_2 = A_{2j}u_j \quad (12)$$

$$v_3 = A_{3j}u_j , \quad (13)$$

where  $j$  is a repeated index where a sum is implied. Accordingly, this set of equations can be finally reduced to [15]

$$v_i = A_{ij}u_j. \quad (14)$$

Since the free index  $i$  can assume values from 1 to 3,  $v_i$  thus corresponds to the three components of a vector  $\mathbf{v} \in \mathbb{R}^3$ . Free indices on each term of an equation must agree, hence the above expression could be rewritten as  $v_k = A_{kj}u_j$ . It is important to mention that no index may appear more than twice within a given term in any expression.

### 2.1.2.2. Kronecker delta and inner product

The Kronecker delta ( $\delta_{ij}$ ) is defined by the inner (dot) product between two unit base vectors, as shown in [15]

$$\delta_{ij} = \mathbf{e}_i \cdot \mathbf{e}_j = \begin{cases} 1, & i = j, \\ 0, & i \neq j. \end{cases} \quad (15)$$

Using the definition above, the dot product between vectors  $\mathbf{a}$  and  $\mathbf{b}$  can be expressed in index notation. Let

$$\mathbf{a} = a_m \mathbf{e}_m, \quad \mathbf{b} = b_k \mathbf{e}_k, \quad (16)$$

the dot product is therefore given by

$$\mathbf{a} \cdot \mathbf{b} = a_m \mathbf{e}_m \cdot b_k \mathbf{e}_k. \quad (17)$$

Scalars can be brought to evidence, leading to

$$\mathbf{a} \cdot \mathbf{b} = a_m b_k (\mathbf{e}_m \cdot \mathbf{e}_k) = a_m b_k \delta_{mk}. \quad (18)$$

Expression (18) leads to an interesting identity of the Kronecker delta known as the transfer property [15]. In this identity, the Kronecker delta acts replacing one of the indices by the other, i.e., in  $a_m b_k \delta_{mk}$  either replacing the index  $m$  by  $k$  or replacing  $k$  by  $m$ . Dummy indices can be altered without modifying the expression, resulting in

$$\mathbf{a} \cdot \mathbf{b} = a_m b_k \delta_{mk} = a_m b_m = a_k b_k. \quad (19)$$

### 2.1.3. Second-order tensors

While some quantities in mechanics are well represented by vectors, other physical quantities such as stress and strain are better represented in terms of linear transformations, building the notion of second-order tensors [15].

More specifically, a tensor is a higher order mathematical object that acts correlating two directions in space. Let  $\mathbf{A}$  be a second-order tensor,  $\mathbf{u}$  and  $\mathbf{v}$  respectively the input and output vectors of a linear transformation. Using index notation, the three quantities are related, as previously presented in expression (14), by  $v_i = A_{ij}u_j$ .

Considering that  $\mathbf{u}$  and  $\mathbf{v}$  are vectors in space, the second-order tensor  $\mathbf{A}$  used to establish the relation between the input and output vectors must be constituted by nine components, as can be observed in equation (7). Each component  $v_i$  of the linear transformation is therefore determined using the summation convention, leading to

$$v_i = A_{i1}u_1 + A_{i2}u_2 + A_{i3}u_3, \quad (20)$$

where the matrix representation of the second-order tensor  $\mathbf{A}$  is therefore given by [15]

$$[\mathbf{A}] = \begin{pmatrix} A_{11} & A_{12} & A_{13} \\ A_{21} & A_{22} & A_{23} \\ A_{31} & A_{32} & A_{33} \end{pmatrix}. \quad (21)$$

Considering that tensors are linear applications, the properties below are satisfied [17]:

- $\mathbf{T}(\mathbf{u} + \mathbf{v}) = \mathbf{T}(\mathbf{u}) + \mathbf{T}(\mathbf{v})$ ;
- $\mathbf{T}(\alpha\mathbf{u}) = \alpha\mathbf{T}(\mathbf{u})$ , where  $\alpha$  is a scalar.

In addition, the zero tensor  $\mathbf{O}$  and the identity tensor  $\mathbf{I}$  can be defined, as given by [15]

- $\mathbf{O}\mathbf{v} = \mathbf{0}$ , where  $\mathbf{0}$  is a vector where all components are nil;
- $\mathbf{I}\mathbf{v} = \mathbf{v}$ , where  $\mathbf{I}$  transforms  $\mathbf{v}$  into itself.

Lastly, two tensors  $\mathbf{S}$  and  $\mathbf{T}$  are equal if they output the same vector when transforming an input vector  $\mathbf{v}$ , i.e., [15].

$$\mathbf{S}\mathbf{v} = \mathbf{T}\mathbf{v}. \quad (22)$$

### 2.1.4. Components of a vector and a second-order tensor

The components  $w_i$  of a vector  $\mathbf{w}$  can be obtained by projecting  $\mathbf{w}$  onto the direction of  $\mathbf{e}_i$ . Let  $\mathbf{w}$  be represented by  $w_j \mathbf{e}_j$  (instead of  $w_i \mathbf{e}_i$ ) in order to avoid the excessive repetition of the index  $i$ . Such operation can be derived as follows.

$$\mathbf{w} \cdot \mathbf{e}_i = (w_j \mathbf{e}_j) \cdot \mathbf{e}_i = w_j (\mathbf{e}_j \cdot \mathbf{e}_i) = w_j \delta_{ji} = w_i \quad (23)$$

The components of a second-order tensor can be accordingly determined. Assuming  $\mathbf{v}$  is a vector obtained from the linear transformation of the vector  $\mathbf{u}$ , i.e.,  $\mathbf{v} = \mathbf{A}\mathbf{u}$ , its components  $v_i$  can be obtained by projecting both sides of such expression to the direction of  $\mathbf{e}_i$ .

$$\begin{aligned} v_i &= \mathbf{e}_i \cdot \mathbf{v} = \mathbf{e}_i \cdot \mathbf{A}\mathbf{u} \\ &= \mathbf{e}_i \cdot \mathbf{A}(u_j \mathbf{e}_j) = [\mathbf{e}_i \cdot \mathbf{A}\mathbf{e}_j] u_j. \end{aligned} \quad (24)$$

Since  $v_i = A_{ij} u_j$ , as previously presented in expression (14), the component  $A_{ij}$  of the second-order tensor  $\mathbf{A}$  therefore corresponds to [15]

$$A_{ij} = \mathbf{e}_i \cdot \mathbf{A}\mathbf{e}_j. \quad (25)$$

An additional consideration regarding the application of the second-order tensor  $\mathbf{A}$  acting on a basis vector  $\mathbf{e}_i$  must be made. When a given second-order tensor is applied to transform either  $\mathbf{e}_1$ ,  $\mathbf{e}_2$  or  $\mathbf{e}_3$ , the output equals the corresponding column vector of the linear transformation tensor  $\mathbf{A}$ , as given by

$$\begin{aligned} \mathbf{A}\mathbf{e}_1 &= \begin{pmatrix} A_{11} & A_{12} & A_{13} \\ A_{21} & A_{22} & A_{23} \\ A_{31} & A_{32} & A_{33} \end{pmatrix} \begin{Bmatrix} 1 \\ 0 \\ 0 \end{Bmatrix} = \begin{Bmatrix} A_{11} \\ A_{21} \\ A_{31} \end{Bmatrix}, & \mathbf{A}\mathbf{e}_2 &= \begin{pmatrix} A_{11} & A_{12} & A_{13} \\ A_{21} & A_{22} & A_{23} \\ A_{31} & A_{32} & A_{33} \end{pmatrix} \begin{Bmatrix} 0 \\ 1 \\ 0 \end{Bmatrix} = \begin{Bmatrix} A_{12} \\ A_{22} \\ A_{32} \end{Bmatrix}, \\ \mathbf{A}\mathbf{e}_3 &= \begin{pmatrix} A_{11} & A_{12} & A_{13} \\ A_{21} & A_{22} & A_{23} \\ A_{31} & A_{32} & A_{33} \end{pmatrix} \begin{Bmatrix} 0 \\ 0 \\ 1 \end{Bmatrix} = \begin{Bmatrix} A_{13} \\ A_{23} \\ A_{33} \end{Bmatrix}. \end{aligned} \quad (26)$$

When  $\mathbf{A}$  transforms a basis vector  $\mathbf{e}_i$ , the output vector presents components  $A_{ji}$  for each direction  $\mathbf{e}_j$ . The free index shifts to the second position, and the relation is thus given by

$$\mathbf{A}\mathbf{e}_i = A_{ji} \mathbf{e}_j. \quad (27)$$

### 2.1.5. Product between tensors

The product between tensors in index notation is defined as follows. Let tensor  $\mathbf{C}$  be the result from the product between tensors  $\mathbf{A}$  and  $\mathbf{B}$ , i.e.,  $\mathbf{C} = \mathbf{AB}$ . The components  $C_{ij}$  are

$$\begin{aligned}
 C_{ij} &= \mathbf{e}_i \cdot \mathbf{C} \mathbf{e}_j = \mathbf{e}_i \cdot (\mathbf{AB}) \mathbf{e}_j \\
 &= \mathbf{e}_i \cdot \mathbf{A}(\mathbf{B} \mathbf{e}_j) = \mathbf{e}_i \cdot \mathbf{A}(B_{kj} \mathbf{e}_k) \\
 &= B_{kj}(\mathbf{e}_i \cdot \mathbf{A} \mathbf{e}_k) = B_{kj}(A_{ik}) \\
 &= A_{ik} B_{kj},
 \end{aligned} \tag{28}$$

where the number of columns of the first tensor corresponds the number of rows of the second.

### 2.1.6. Transpose tensor and change of basis

To every tensor  $\mathbf{S}$ , a transpose tensor  $\mathbf{S}^T$  is associated, where the property below is fulfilled [17].

$$\mathbf{v} \cdot \mathbf{S} \mathbf{u} = \mathbf{u} \cdot \mathbf{S}^T \mathbf{v} \tag{29}$$

The proof is derived using index notation, as presented in sequence.

$$\begin{aligned}
 \mathbf{v} \cdot \mathbf{S} \mathbf{u} &= (v_i \mathbf{e}_i) \cdot \mathbf{S}(u_j \mathbf{e}_j) \\
 &= u_j (\mathbf{e}_i \cdot \mathbf{S} \mathbf{e}_j) v_i = u_j (S_{ij}) v_i = u_j S_{ji}^T v_i \\
 &= \mathbf{u} \cdot \mathbf{S}^T \mathbf{v}
 \end{aligned} \tag{30}$$

It can also be shown that the result of transposing a multiplication of two second-order tensor  $(\mathbf{ST})^T$  corresponds to  $\mathbf{T}^T \mathbf{S}^T$ , as shown in

$$\begin{aligned}
 \mathbf{v} \cdot (\mathbf{ST}) \mathbf{u} &= v_j \mathbf{e}_j \cdot (\mathbf{ST}) u_i \mathbf{e}_i = u_i \{ \mathbf{e}_j \cdot \mathbf{S} \mathbf{T} \mathbf{e}_i \} v_j \\
 &= u_i \{ \mathbf{e}_j \cdot \mathbf{S} \mathbf{T}_{ki} \mathbf{e}_k \} v_j = u_i T_{ki} \{ \mathbf{e}_j \cdot \mathbf{S} \mathbf{e}_k \} v_j \\
 &= u_i T_{ki} S_{jk} v_j = u_i T_{ik}^T S_{kj}^T v_j \\
 &= \mathbf{u} \cdot (\mathbf{T}^T \mathbf{S}^T) \mathbf{v}.
 \end{aligned} \tag{31}$$

The concept of transpose tensor useful for changing the basis of a given system. Let  $\{\mathbf{e}_i\}$  be an orthonormal basis that coincides with the initial orientation of the reference system.

Let  $\{\bar{\mathbf{e}}_i\}$  be a second basis with different orientation. Tensor  $\mathbf{Q}$  corresponds to the linear transformation that correlates both basis, as given by [15]

$$\bar{\mathbf{e}}_i = \mathbf{Q}\mathbf{e}_i. \quad (32)$$

Different notations are employed in the literature, and the above expression could be rewritten in terms of a certain tensor  $\mathbf{M}$  that transforms the basis from its final orientation back to its initial position,  $\mathbf{e}_i = \mathbf{M}\bar{\mathbf{e}}_i$ . Accordingly, it is clear that both approaches are identical as the linear transformation  $\mathbf{M}$  is equal to the inverse transformation employed by tensor  $\mathbf{Q}$ , i.e.,  $\mathbf{M} = \mathbf{Q}^{-1}$ . Nevertheless, the present work utilises the notation as presented in expression (32).

Considering that  $\mathbf{Q}$  is an orthonormal transformation, its inverse  $\mathbf{Q}^{-1}$  corresponds to its transpose  $\mathbf{Q}^T$ . Accordingly,  $\mathbf{Q}^T\mathbf{Q} = \mathbf{I}$ , which is stated in index notation as [15]

$$Q_{ki} Q_{kj} = Q_{ik}^T Q_{kj} = \delta_{ij}. \quad (33)$$

From the definition presented in equation (15), the Kronecker delta precisely corresponds to all nine components of the identity tensor  $\mathbf{I}$ . Furthermore, it can be shown that the resulting basis  $\{\bar{\mathbf{e}}_i\}$  retains the orthonormal characteristic initially presented by  $\{\mathbf{e}_i\}$ , prior to the change of basis [15].

$$\begin{aligned} \bar{\mathbf{e}}_i \cdot \bar{\mathbf{e}}_j &= (\mathbf{Q}\mathbf{e}_i) \cdot (\mathbf{Q}\mathbf{e}_j) \\ &= Q_{ki}\mathbf{e}_k \cdot Q_{lj}\mathbf{e}_l = Q_{ki}(\mathbf{e}_k \cdot \mathbf{e}_l)Q_{lj} \\ &= Q_{ki} \delta_{kl} Q_{lj} = Q_{ki} Q_{kj} = Q_{ik}^T Q_{kj} \\ &= \delta_{ij} \end{aligned} \quad (34)$$

### 2.1.6.1. Components of vectors and tensors after changing the basis

A given vector  $\mathbf{u}$  exists regardless of the basis used to describe it. Changing the basis of the system requires that the components  $\mathbf{u}$  must be rewritten in terms of the new basis  $\{\bar{\mathbf{e}}_i\}$ . Such components can be obtained by projecting  $\mathbf{u}$  onto  $\bar{\mathbf{e}}_i$ , as given by

$$\mathbf{u} = u_i\mathbf{e}_i = \bar{u}_i\bar{\mathbf{e}}_i \quad (35)$$

Accordingly,

$$\begin{aligned}
 \bar{u}_i &= \mathbf{u} \cdot \bar{\mathbf{e}}_i = (u_j \mathbf{e}_j) \cdot (\mathbf{Q} \mathbf{e}_i) = u_j (\mathbf{e}_j \cdot \mathbf{Q} \mathbf{e}_i) \\
 &= (\mathbf{e}_j \cdot \mathbf{Q} \mathbf{e}_i) u_j = Q_{ji} u_j \\
 &= Q_{ij}^T u_j .
 \end{aligned} \tag{36}$$

Considering that the vector  $\mathbf{u}$  expressed in terms of its new basis  $\{\bar{\mathbf{e}}_i\}$  can be represented as  $\bar{\mathbf{u}}$ , the above derivation results in [15]

$$\bar{\mathbf{u}} = \mathbf{Q}^T \mathbf{u} . \tag{37}$$

Changing the basis of the system also modifies the components of a second-order tensor. The modified components  $\bar{A}_{ij}$  are therefore given by [15]

$$\begin{aligned}
 \bar{A}_{ij} &= \bar{\mathbf{e}}_i \cdot \mathbf{A} \bar{\mathbf{e}}_j = (\mathbf{Q} \mathbf{e}_i) \cdot \mathbf{A} (\mathbf{Q} \mathbf{e}_j) \\
 &= (Q_{ki} \mathbf{e}_k) \cdot \mathbf{A} (Q_{lj} \mathbf{e}_l) = Q_{ki} (\mathbf{e}_k \cdot \mathbf{A} \mathbf{e}_l) Q_{lj} \\
 &= Q_{ik}^T A_{kl} Q_{lj} ,
 \end{aligned} \tag{38}$$

resulting in

$$\bar{\mathbf{A}} = \mathbf{Q}^T \mathbf{A} \mathbf{Q} . \tag{39}$$

### 2.1.6.2. Components of the change of basis tensor $\mathbf{Q}$

As presented in equation (32), the change of basis can be carried out by employing the expression  $\bar{\mathbf{e}}_j = \mathbf{Q} \mathbf{e}_j$ . The quantities presented on both sides of this expression can be projected to  $\{\mathbf{e}_i\}$ , as given by [15]

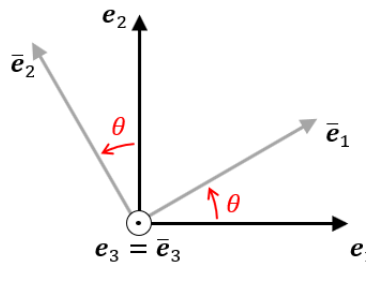
$$\begin{aligned}
 \mathbf{e}_i \cdot \bar{\mathbf{e}}_j &= \mathbf{e}_i \cdot \mathbf{Q} \mathbf{e}_j = \mathbf{e}_i \cdot (Q_{kj} \mathbf{e}_k) \\
 &= Q_{kj} (\mathbf{e}_i \cdot \mathbf{e}_k) = Q_{kj} \delta_{ik} \\
 &= Q_{ij} .
 \end{aligned} \tag{40}$$

Expression (40) states that the components of the change of basis tensor correspond to the inner product between components of the basis  $\{\mathbf{e}_i\}$  and components of the new basis

$\{\bar{\mathbf{e}}_j\}$ . Considering that the bases are orthonormal, all the involved vectors are therefore unitary. The components of the tensor  $\mathbf{Q}$  can be obtained according to [15]

$$Q_{ij} = |\mathbf{e}_i| |\bar{\mathbf{e}}_j| \cos(\theta) = \cos(\theta). \quad (41)$$

The change of basis as presented above corresponds to an anticlockwise rotation to the reference system of a certain angle  $\theta$  with respect to a certain axis that remains unaltered. Expression (42) exemplifies a rotation to the reference system of a certain angle  $\theta$  with respect to  $\mathbf{e}_3$ , as presented in Fig. 6.



$$[\mathbf{Q}] = \begin{pmatrix} \cos(\mathbf{e}_1, \bar{\mathbf{e}}_1) & \cos(\mathbf{e}_1, \bar{\mathbf{e}}_2) & \cos(\mathbf{e}_1, \bar{\mathbf{e}}_3) \\ \cos(\mathbf{e}_2, \bar{\mathbf{e}}_1) & \cos(\mathbf{e}_2, \bar{\mathbf{e}}_2) & \cos(\mathbf{e}_2, \bar{\mathbf{e}}_3) \\ \cos(\mathbf{e}_3, \bar{\mathbf{e}}_1) & \cos(\mathbf{e}_3, \bar{\mathbf{e}}_2) & \cos(\mathbf{e}_3, \bar{\mathbf{e}}_3) \end{pmatrix}$$

$$[\mathbf{Q}] = \begin{pmatrix} \cos(\theta) & -\sin(\theta) & 0 \\ \sin(\theta) & \cos(\theta) & 0 \\ 0 & 0 & 1 \end{pmatrix} \quad (42)$$

Figure 6 – Anticlockwise rotation of  $\theta$  to the reference system

### 2.1.7. Dyadic product

The dyadic product between two vectors  $\mathbf{u}$  and  $\mathbf{v}$  is a second-order tensor  $\mathbf{A}$ , as presented in [15]

$$\mathbf{u} \otimes \mathbf{v} = \begin{pmatrix} u_1 v_1 & u_1 v_2 & u_1 v_3 \\ u_2 v_1 & u_2 v_2 & u_2 v_3 \\ u_3 v_1 & u_3 v_2 & u_3 v_3 \end{pmatrix} = \mathbf{A}. \quad (43)$$

In terms of components, it can be stated that

$$A_{ij} = u_i v_j. \quad (44)$$

Since  $\mathbf{A}$  is a linear operator itself,  $\mathbf{A}$  could be applied to a vector  $\mathbf{w}$  in order to obtain an output vector  $\mathbf{m}$ , as presented in

$$\mathbf{m} = \mathbf{A}\mathbf{w} = (\mathbf{u} \otimes \mathbf{v})\mathbf{w}. \quad (45)$$

The components  $m_i$  can be expressed as

$$\begin{aligned} m_i &= A_{ij}w_j = (u_i v_j)w_j \\ &= (v_j w_j)u_i. \end{aligned} \quad (46)$$

Considering that  $v_j w_j$  corresponds to the inner product between vector  $\mathbf{v}$  and  $\mathbf{w}$ , one obtains that  $\mathbf{m}$  is therefore given by

$$m_i \mathbf{e}_i = (v_j w_j) u_i \mathbf{e}_i, \quad (47)$$

leading to

$$\mathbf{m} = (\mathbf{v} \cdot \mathbf{w}) \mathbf{u}. \quad (48)$$

By comparing expressions (45) and (48), one obtains that the dyadic product between  $\mathbf{u}$  and  $\mathbf{v}$  modifying  $\mathbf{w}$  also corresponds to [15]

$$(\mathbf{u} \otimes \mathbf{v}) \mathbf{w} = (\mathbf{v} \cdot \mathbf{w}) \mathbf{u}, \quad (49)$$

which is an essential definition for the adequate comprehension of Cauchy's theorem, to be discussed in following stages of this overview.

## 2.2. Additional mathematical concepts

### 2.2.1. Considerations on several-variable function

In general terms, physical quantities are often dependent on multiple variables. As such, basic concepts concerning single variable functions may be extended to a context where functions receive several variables as input parameters.

For instance, the temperature  $T$  in a room may be expressed in terms of the coordinates  $(x, y, z)$ , as well as being function of time  $t$ , leading to a 4-input variable expression such as  $T = f(x, y, z, t)$ . Likewise, assuming that dimensions remain constant in time, the volume of a cylinder can be expressed as  $V(r, h) = \pi r^2 h$ , where  $r$  is the radius and  $h$  is the height. Despite the difference in notation, where  $T$  omits the input variables while  $V(r, h)$  evidences them, both constitute functions which depend on more than one variable as inputs.

Regarding the context of the present work, attention is turned towards two-variable functions, where both input parameters as well as the output parameter are real numbers. Such function  $f$  of two variables can be defined as a rule that assigns each ordered pair of real numbers  $(x, y)$  in a set  $D$  a unique real number denoted by  $f(x, y)$ . The set  $D$  is the domain of  $f$ , while its range is the set of values that  $f$  takes on [18].

### 2.2.1.1. Level curves

A level curve consists of a set of coordinate points pertaining to the domain which are associated with a fixed value of the function in question. In other words, considering the case of two-variable functions  $y = f(x, y)$ , contour lines (or level curves) are defined as a set of curves pertaining to the domain which satisfies the expression  $f(x, y) = k$ , where  $k$  is a constant.

Fig. 7 presents a graph relative to the function  $f(x, y) = x^2 + y^2$ , along with a number of level curves in the  $xy$  plane associated with generic values of  $k$ .

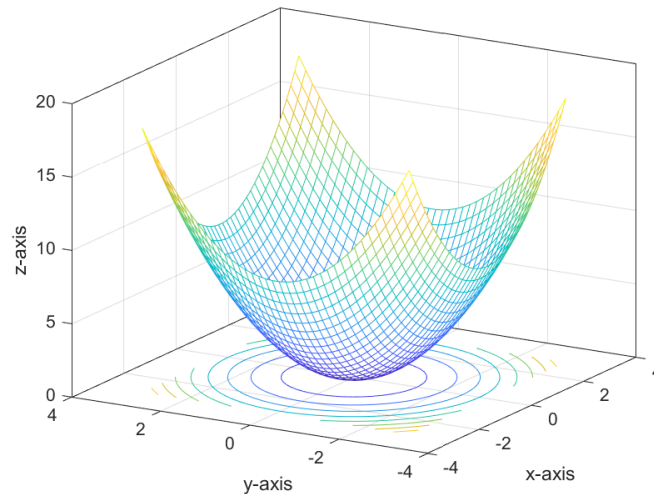


Figure 7 – Level curves relative to an arbitrary function

Much can be learned about a function from inspecting the behaviour of its level curves. In many cases, if the expression to one or more level curves are determined, further generalisation may lead to identifying the expression to the original function itself.

### 2.2.2. Eigenvalues and eigenvectors

Let  $\mathbf{x}$  be a vector pertaining to  $\mathbb{R}^n$  and  $\mathbf{A}$ , a linear operator with dimension  $n \times n$ . Vector  $\mathbf{x}$  is said to be an eigenvector of  $\mathbf{A}$  if it satisfies [17]

$$\mathbf{Ax} = \lambda\mathbf{x} \quad (50)$$

for some scalar  $\lambda \in \mathbb{R}$ . The scalar  $\lambda$ , in turn, is said to be an eigenvalue of the linear transformation  $\mathbf{A}$ . The above expression corresponds to a system of linear equations presenting  $n$  variables and  $n$  equations. It can equivalently be rewritten as

$$\mathbf{Ax} - \lambda\mathbf{x} = \mathbf{0}. \quad (51)$$

By introducing the identity operator  $\mathbf{I}$  in the second term, the expression becomes

$$\mathbf{Ax} - \lambda\mathbf{Ix} = \mathbf{0}, \quad (52)$$

$$(\mathbf{A} - \lambda\mathbf{I})\mathbf{x} = \mathbf{0}. \quad (53)$$

Considering the case where  $\mathbf{x} \in \mathbb{R}^3$ , the linear system corresponds to

$$\begin{pmatrix} A_{11} - \lambda & A_{12} & A_{13} \\ A_{21} & A_{22} - \lambda & A_{23} \\ A_{31} & A_{32} & A_{33} - \lambda \end{pmatrix} \begin{Bmatrix} x_1 \\ x_2 \\ x_3 \end{Bmatrix} = \begin{Bmatrix} 0 \\ 0 \\ 0 \end{Bmatrix}. \quad (54)$$

If the number of variables corresponds to the number of linearly independent linear equations, the system admits a single trivial solution, given by  $\mathbf{x} = \mathbf{0}$ . In order to obtain different solutions, the above expression must satisfy [17]

$$\det(\mathbf{A} - \lambda\mathbf{I}) = 0, \quad (55)$$

as this allows the system to remain consistent, with infinitely many solutions. In fact, expression (54) cannot admit an inverse matrix to  $(\mathbf{A} - \lambda\mathbf{I})$ , as this would lead to  $\mathbf{x} = (\mathbf{A} - \lambda\mathbf{I})^{-1} \mathbf{0}$ , which is not acceptable as the zero vector cannot be transformed into anything other than the zero vector itself. Accordingly, equation (55) thus leads to a characteristic polynomial expression of third degree, where each value of  $\lambda$  that satisfies this expression is therefore an eigenvalue of the system. Vectors associated with eigenvalues correspond to the eigenvectors of the system.

### 2.3. Relevant concepts of mechanical behaviour of solids

Forces arising from the interaction between a solid body  $\Omega$  and its surrounding environment are essentially of two kinds: contact forces  $\mathbf{h}$  and body forces  $\mathbf{b}$  [19]. Contact forces  $\mathbf{h}$ , with units in force per area, act on the boundary surface  $\partial\Omega$  of the solid. Body forces, in turn, correspond to forces exerted by the environment on interior points within the volume  $\Omega$ , typically due to force fields such as gravity or electromagnetic fields [19], thus presenting units of force per volume.

If the solid body is in equilibrium, as shown in Fig. 8(a), then the resulting force is nil, as given by [19]

$$\int_{\partial\Omega} \mathbf{h} dA + \int_{\Omega} \mathbf{b} dV = \mathbf{0}. \quad (56)$$

Equilibrium is also valid for parts of the solid body. However, since different parts are subjected to different sets of forces, equilibrium can only be achieved if different parts of the material interact exerting forces upon each other. The internal forces acting on a given part  $p$  are represented in Fig. 8(b) by Cauchy's stress vector  $\mathbf{t}$ , with units in force per area.

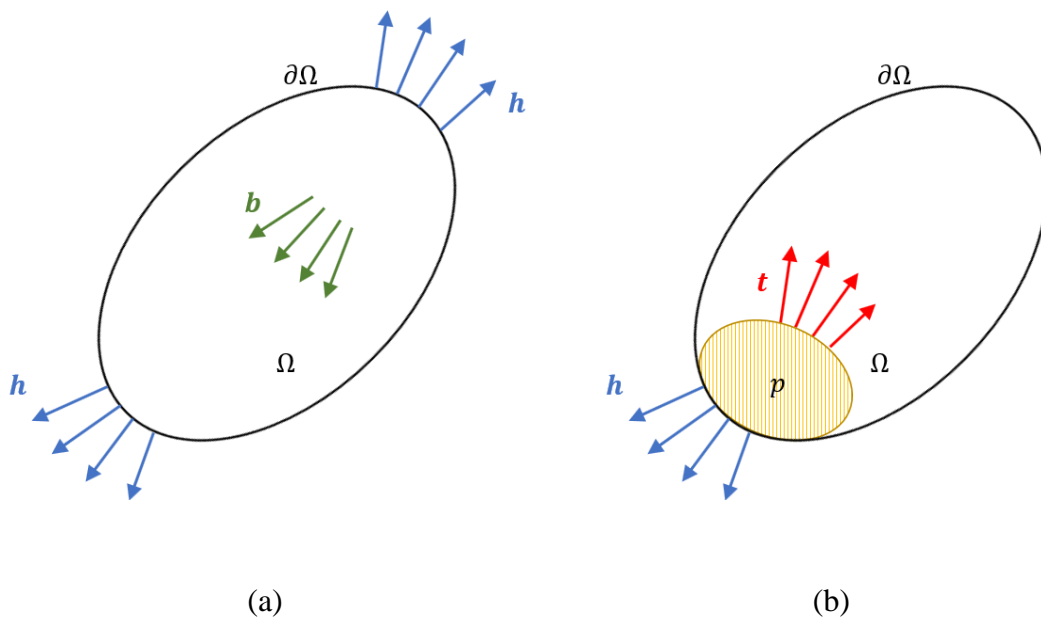


Figure 8 – (a) Contact and body forces; (b) equilibrium of part  $p$  due to internal forces  $\mathbf{t}$

### 2.3.1. Cauchy's postulate

From a more localised perspective, consider a point  $P$  (with coordinates given by the vector  $\mathbf{x}$ ) pertaining to the boundary surface of a given part  $p$  well within the solid body. Considering that the surface of  $p$  is subjected to a given distribution of internal forces, point  $P$  itself experiences the stress vector  $\mathbf{t}$ . Nevertheless, it is to be pointed out the solid can be partitioned in infinitely many ways, where point  $P$  can simultaneously be part of different boundaries associated with different parts, for instance parts  $p_1$  and  $p_2$ . This indicates that the stress vector  $\mathbf{t}$  acting on  $P$  is therefore independent of the selected part  $p$ .

As such, Cauchy assumed that the stress vector  $\mathbf{t}$  depends on the location of the point  $P$  as well as on the orientation of the tangent plane at point  $P$ . Such hypothesis implies that, upon two different material parts  $p_1$  and  $p_2$ , the stress vector  $\mathbf{t}$  acting on  $P$  is the same, even though  $p_1$  and  $p_2$  may be subjected to different sets of forces. Fig. 9 exemplifies the described situation, where  $\mathbf{n}$  corresponds to the unitary normal vector associated with the material plane tangent to both  $p_1$  and  $p_2$  at  $P$ .

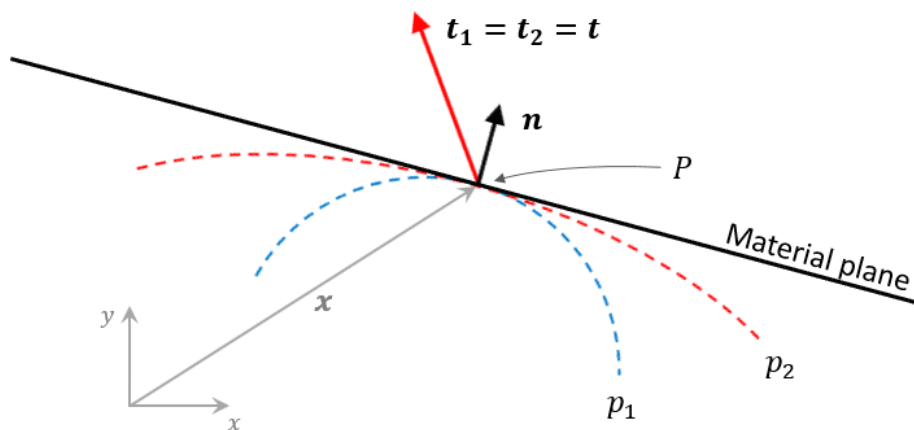


Figure 9 – Cauchy's hypothesis

Changing the orientation of the tangent plane accordingly modifies the stress vector  $\mathbf{t}$ , as  $\mathbf{t}$  is function of the position and the normal vector of the material plane, as given by

$$\mathbf{t} = \mathbf{f}(\mathbf{x}, \mathbf{n}). \quad (57)$$

## 2.3.2. Cauchy's theorem

### 2.3.2.1. Part I: the stress tensor

Consider an elementary volume, as presented in Fig. 10(a), where all sides of the solid are subjected to normal and shear stresses. If the solid is in equilibrium, so are smaller partitions of it. As illustrated in Fig. 10(b), a tetrahedral part (obtained by slicing the elementary volume, as shown) is considered where an internal stress vector  $\mathbf{t}(\mathbf{n})$  acting on PQR is revealed in order to maintain the part in equilibrium, as is the whole solid. The adopted notation  $\mathbf{t}(\mathbf{n})$  aims to emphasise that  $\mathbf{t}$  is a function of the material plane uniquely described by its normal unitary vector  $\mathbf{n}$  [19].

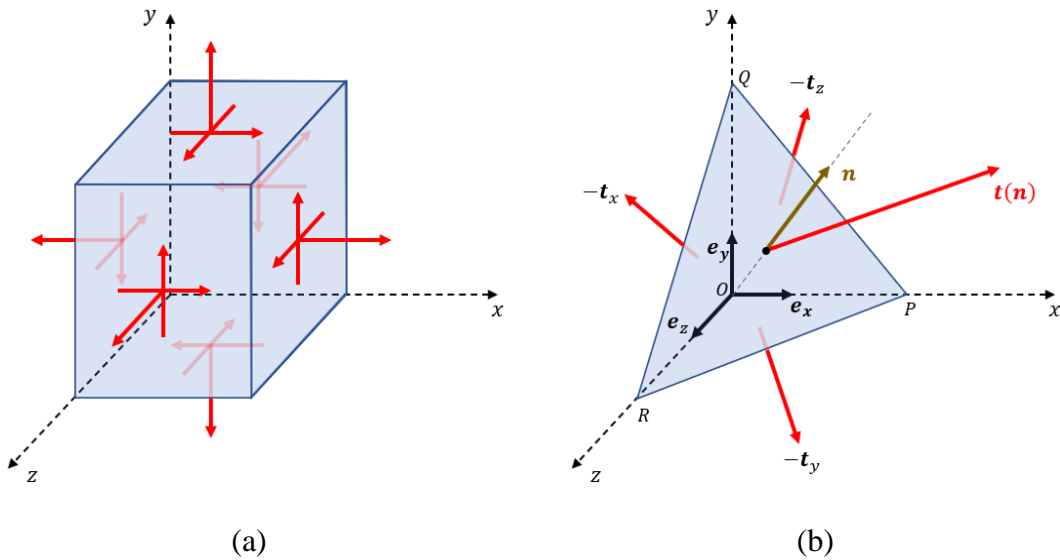


Figure 10 – (a) Entire solid in equilibrium; (b) part in equilibrium

By imposing equilibrium, the resultant force is nil, accordingly leading to

$$\mathbf{t}(\mathbf{n})\Delta A - \mathbf{t}_x\Delta A_x - \mathbf{t}_y\Delta A_y - \mathbf{t}_z\Delta A_z + \mathbf{b}\Delta V = \mathbf{0}, \quad (58)$$

where  $\Delta A$ ,  $\Delta A_x$ ,  $\Delta A_y$  and  $\Delta A_z$  correspond the areas upon which  $\mathbf{t}(\mathbf{n})$ ,  $-\mathbf{t}_x$ ,  $-\mathbf{t}_y$  and  $-\mathbf{t}_z$  respectively act. Accordingly,  $-\mathbf{t}_x$ ,  $-\mathbf{t}_y$  and  $-\mathbf{t}_z$  each correspond to a combination of normal stress and to two components of shear stress, equivalent to what is shown in Fig. 10(a). In addition,  $\mathbf{b}$  is the body force acting on the tetrahedral.

Any given area  $\Delta A$  can be expressed in terms of its normal vector. Accordingly, from a vectorial perspective, the quantity  $\Delta \mathbf{A}$  can be expressed as

$$\Delta \mathbf{A} = \Delta A \mathbf{n}. \quad (59)$$

Considering that the areas  $\Delta A_x$ ,  $\Delta A_y$  and  $\Delta A_z$  correspond to the projection of  $\Delta \mathbf{A}$  towards  $\mathbf{e}_x$ ,  $\mathbf{e}_y$  and  $\mathbf{e}_z$ , one straightforwardly obtains

$$\begin{aligned} \Delta A_x &= (\Delta_A \mathbf{n}) \cdot \mathbf{e}_x = \Delta A (\mathbf{n} \cdot \mathbf{e}_x) \\ \Delta A_y &= (\Delta_A \mathbf{n}) \cdot \mathbf{e}_y = \Delta A (\mathbf{n} \cdot \mathbf{e}_y) \\ \Delta A_z &= (\Delta_A \mathbf{n}) \cdot \mathbf{e}_z = \Delta A (\mathbf{n} \cdot \mathbf{e}_z). \end{aligned} \quad (60)$$

In addition, the volume of the tetrahedron is given by

$$\Delta V = \frac{1}{3} \Delta h \Delta A, \quad (61)$$

where  $\Delta h$  is the distance between O and the surface PQR (Fig. 10).

Equilibrium can therefore be rewritten as [19]

$$\mathbf{t}(\mathbf{n}) \Delta A - \Delta A (\mathbf{n} \cdot \mathbf{e}_x) \mathbf{t}_x - \Delta A (\mathbf{n} \cdot \mathbf{e}_y) \mathbf{t}_y - \Delta A (\mathbf{n} \cdot \mathbf{e}_z) \mathbf{t}_z + \mathbf{b} \frac{1}{3} \Delta h \Delta A = \mathbf{0}. \quad (62)$$

Since  $\Delta A$  is a common factor different than zero, the entire expression can be divided by this quantity. Considering the limiting case when  $\Delta h$  tends to zero, its corresponding term may be disregarded. Accordingly, the expression becomes [19]

$$\mathbf{t}(\mathbf{n}) = (\mathbf{n} \cdot \mathbf{e}_x) \mathbf{t}_x + (\mathbf{n} \cdot \mathbf{e}_y) \mathbf{t}_y + (\mathbf{n} \cdot \mathbf{e}_z) \mathbf{t}_z. \quad (63)$$

By using the definition of the dyadic product presented in expression (49), one obtains

$$\mathbf{t}(\mathbf{n}) = (\mathbf{t}_x \otimes \mathbf{e}_x) \mathbf{n} + (\mathbf{t}_y \otimes \mathbf{e}_y) \mathbf{n} + (\mathbf{t}_z \otimes \mathbf{e}_z) \mathbf{n}, \quad (64)$$

where  $\mathbf{n}$  can be evidenced, leading to

$$\mathbf{t}(\mathbf{n}) = (\mathbf{t}_x \otimes \mathbf{e}_x + \mathbf{t}_y \otimes \mathbf{e}_y + \mathbf{t}_z \otimes \mathbf{e}_z) \mathbf{n}. \quad (65)$$

Finally, one can conclude that [19]

$$\mathbf{t}(\mathbf{n}) = \mathbf{T} \mathbf{n}, \quad (66)$$

where  $\mathbf{T}$  corresponds to Cauchy's stress tensor as given by

$$\mathbf{T} = \mathbf{t}_x \otimes \mathbf{e}_x + \mathbf{t}_y \otimes \mathbf{e}_y + \mathbf{t}_z \otimes \mathbf{e}_z. \quad (67)$$

From the first part of Cauchy's theorem, it can be straightforwardly concluded that the stress-state acting on a given location is fully determined if the stress vectors acting on three mutually orthogonal planes are known. In addition, the stress-tensor can be interpreted as a mathematical object that, provided a material plane, the stress-tensor delivers the stress vector  $\mathbf{t}$  acting the plane of interest, allowing one to straightforwardly obtain the associated normal and shear stresses.

### 2.3.2.2. Part II: symmetry of the stress tensor

The elementary volume is a cubic solid with dimensions  $\Delta x$ ,  $\Delta y$  and  $\Delta z$  subjected to forces that impose moments to the body. The symmetry of the stress tensor is a consequence of the equilibrium of moments [19]. As presented in Fig. 11, it is assumed that normal and shear stresses are applied at the centre of their respective surfaces, while body forces are assumed to be applied at the centre of the elementary volume.

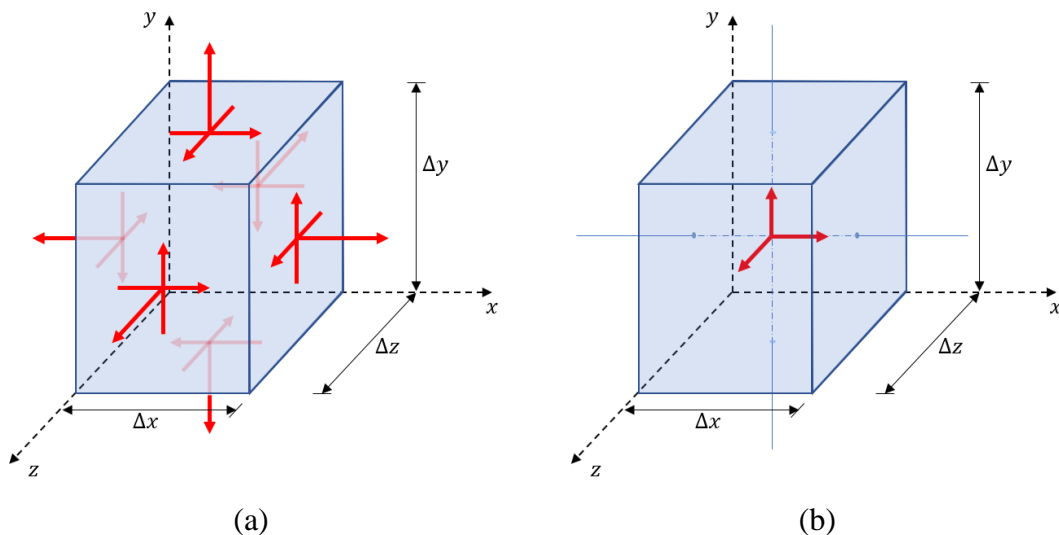


Figure 11 – Forces acting on elementary volume (a) contact forces and (b) body forces

The following derivation evaluates the moments with respect to the  $z$  axis. As one would expect, forces parallel to  $\mathbf{e}_z$  do not result in torques about the  $z$  axis. In addition, given

that the elementary volume is assumed to be in equilibrium, the resulting moment is nil. The analysis is broken down into four smaller steps.

**Step 1** considers the effect of the body forces, as presented in Fig. 12. The moment due to body forces  $M_b$  is given by

$$\begin{aligned} M_b &= \left[ \frac{\Delta x}{2} \mathbf{e}_x \times b_y (\Delta x \Delta y \Delta z) \mathbf{e}_y \right] + \left[ \frac{\Delta y}{2} \mathbf{e}_y \times b_x (\Delta x \Delta y \Delta z) \mathbf{e}_x \right] \\ &= \frac{\Delta x}{2} b_y (\Delta x \Delta y \Delta z) \mathbf{e}_z - \frac{\Delta y}{2} b_x (\Delta x \Delta y \Delta z) \mathbf{e}_z. \end{aligned} \quad (68)$$

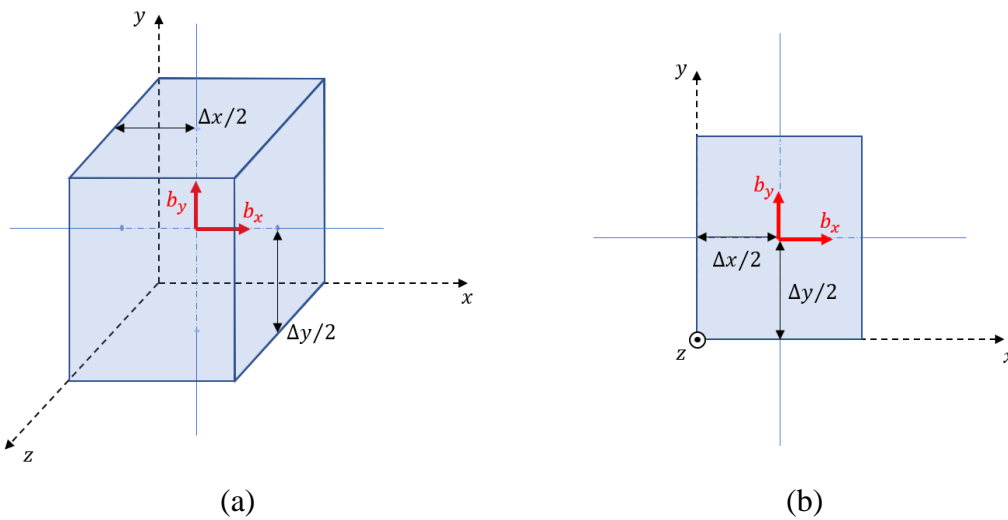


Figure 12 – Moments produced by body forces (a) general view and (b) top view

**Step 2** considers the moment produced by normal forces  $M_n$ , as presented in Fig. 13. Such expression is given by

$$\begin{aligned} M_n &= \left[ \frac{\Delta x}{2} \mathbf{e}_x \times \sigma_{yy} (\Delta x \Delta z) (-\mathbf{e}_y) \right] + \\ &+ \left[ \frac{\Delta x}{2} \mathbf{e}_x \times \left( \sigma_{yy} + \frac{\partial \sigma_{yy}}{\partial y} \Delta y \right) (\Delta x \Delta z) \mathbf{e}_y \right] + \\ &+ \left[ \frac{\Delta y}{2} \mathbf{e}_y \times \sigma_{xx} (\Delta y \Delta z) (-\mathbf{e}_x) \right] + \\ &+ \left[ \frac{\Delta y}{2} \mathbf{e}_y \times \left( \sigma_{xx} + \frac{\partial \sigma_{xx}}{\partial x} \Delta x \right) (\Delta y \Delta z) \mathbf{e}_x \right], \end{aligned} \quad (69)$$

where terms in different colours cancel out, leading to

$$M_n = \left[ \frac{\Delta x}{2} \frac{\partial \sigma_{yy}}{\partial y} (\Delta x \Delta y \Delta z) \right] \mathbf{e}_z - \left[ \frac{\Delta y}{2} \frac{\partial \sigma_{xx}}{\partial x} (\Delta x \Delta y \Delta z) \right] \mathbf{e}_z . \quad (70)$$

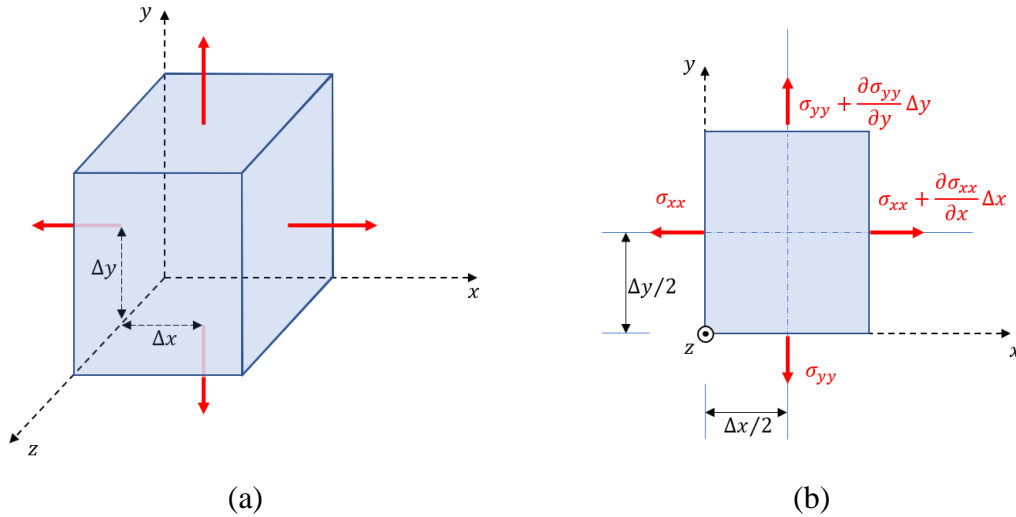


Figure 13 – Moments produced by normal forces (a) general view and (b) frontal view

**Step 3** considers the moments  $M_{s,1}$  produced by shear forces acting on  $z$  planes, as shown in Fig. 14.

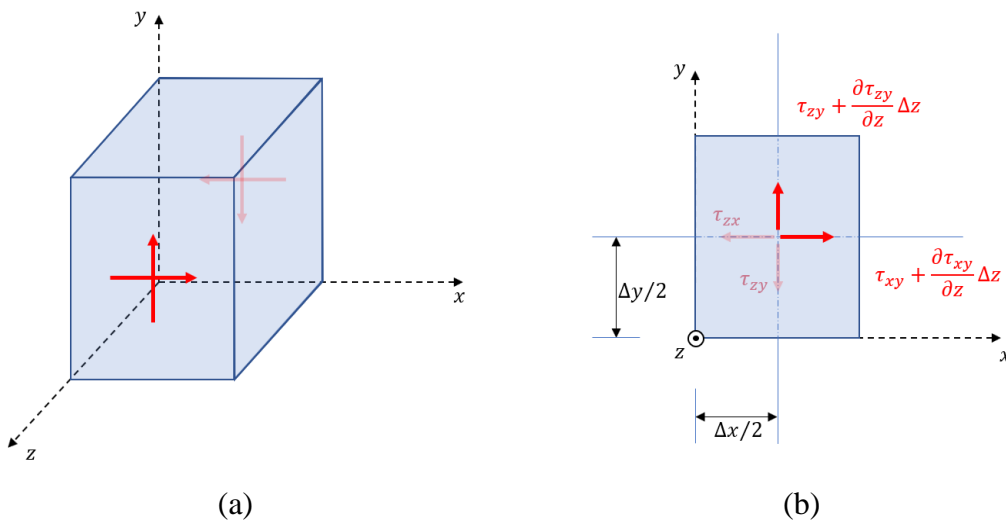


Figure 14 – Moments produced by shear forces acting on  $z$  planes (a) general view and (b) frontal view

The corresponding expression is given by

$$\begin{aligned}
 M_{s,1} = & \left[ \frac{\Delta x}{2} \mathbf{e}_x \times \tau_{zy}(\Delta x \Delta y)(-\mathbf{e}_y) \right] + \\
 & + \left[ \frac{\Delta x}{2} \mathbf{e}_x \times \left( \tau_{zy} + \frac{\partial \tau_{zy}}{\partial z} \Delta z \right) (\Delta x \Delta y)(\mathbf{e}_y) \right] + \\
 & + \left[ \frac{\Delta y}{2} \mathbf{e}_y \times \tau_{zx}(\Delta x \Delta y)(-\mathbf{e}_x) \right] + \\
 & + \left[ \frac{\Delta y}{2} \mathbf{e}_y \times \left( \tau_{zx} + \frac{\partial \tau_{zx}}{\partial z} \Delta z \right) (\Delta x \Delta y)(\mathbf{e}_x) \right], \tag{71}
 \end{aligned}$$

where terms in different colours cancel out, leading to

$$M_{s,1} = \left[ \frac{\Delta x}{2} \frac{\partial \tau_{zy}}{\partial z} (\Delta x \Delta y \Delta z) \right] \mathbf{e}_z - \left[ \frac{\Delta y}{2} \frac{\partial \tau_{zx}}{\partial z} (\Delta x \Delta y \Delta z) \right] \mathbf{e}_z. \tag{72}$$

**Step 4** considers the moments  $M_{s,2}$  produced by shear forces acting on  $x$  and  $y$  planes, as presented in Fig. 15. It is important to mention that  $\tau_{xy}$  and  $\tau_{yz}$  do not produce moments as the perpendicular distance to the  $z$  axis is nil.

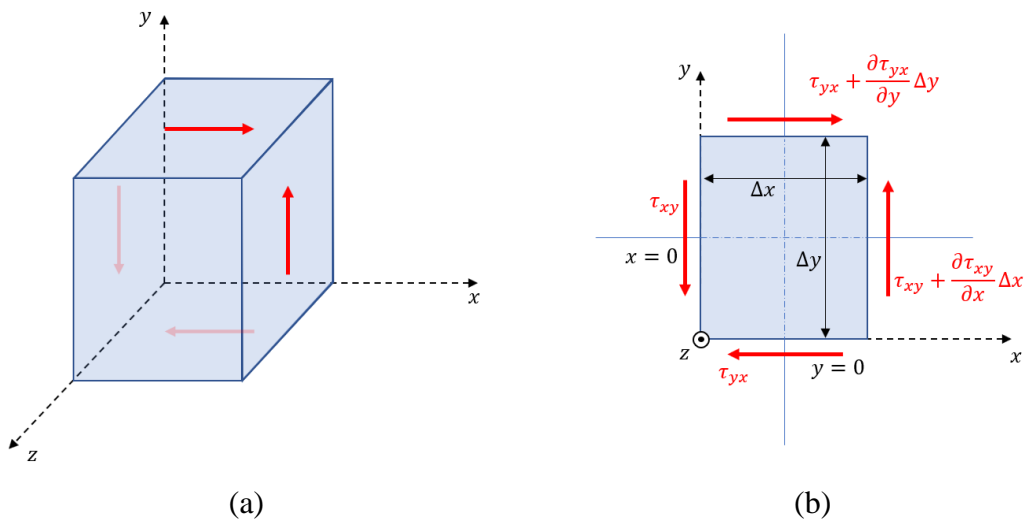


Figure 15 – Moments produced by shear forces acting on  $x$  and  $y$  planes (a) general view and (b) top view

The corresponding expression is

$$M_{s,2} = \left[ (\Delta x) \mathbf{e}_x \times \left( \tau_{xy} + \frac{\partial \tau_{xy}}{\partial x} \Delta x \right) (\Delta y \Delta z) \mathbf{e}_y \right] + \left[ (\Delta y) (\mathbf{e}_y) \times \left( \tau_{yx} + \frac{\partial \tau_{yx}}{\partial y} \Delta y \right) (\Delta x \Delta z) \mathbf{e}_x \right], \quad (73)$$

leading to

$$M_{s,2} = [\tau_{xy}(\Delta x \Delta y \Delta z) \mathbf{e}_z] + \left[ \left( \frac{\partial \tau_{xy}}{\partial y} \Delta x \right) (\Delta x \Delta y \Delta z) \mathbf{e}_z \right] + [\tau_{yx}(\Delta x \Delta y \Delta z) \mathbf{e}_z] - \left[ \left( \frac{\partial \tau_{yx}}{\partial y} \Delta y \right) (\Delta x \Delta y \Delta z) \mathbf{e}_z \right]. \quad (74)$$

Equilibrium is obtained when the sum of the terms  $M_b$ ,  $M_n$ ,  $M_{s,1}$  and  $M_{s,2}$  equals zero [19]. Dividing by  $\Delta x \Delta y \Delta z$  (and omitting  $\mathbf{e}_z$ ), the whole expression becomes

$$\left( \frac{\Delta x}{2} b_y - \frac{\Delta y}{2} b_x \right) + \left( \frac{\Delta x}{2} \frac{\partial \sigma_{yy}}{\partial y} - \frac{\Delta y}{2} \frac{\partial \sigma_{xx}}{\partial x} \right) + \left( \frac{\Delta x}{2} \frac{\partial \tau_{zy}}{\partial z} - \frac{\Delta y}{2} \frac{\partial \tau_{zx}}{\partial z} \right) + \left( \tau_{xy} + \frac{\partial \tau_{xy}}{\partial y} \Delta x - \tau_{yx} - \frac{\partial \tau_{yx}}{\partial y} \Delta y \right) = 0. \quad (75)$$

In the limiting case where both  $\Delta x$  and  $\Delta y$  tend to zero, one obtains

$$\tau_{xy} - \tau_{yx} = 0, \quad (76)$$

from where it can be concluded that

$$\tau_{xy} = \tau_{yx}. \quad (77)$$

Analogously to this derivation, one may carry out the same procedure with respects to axes  $x$  and  $y$ , leading to

$$\tau_{xz} = \tau_{zx} \quad (78)$$

$$\tau_{yz} = \tau_{zy}, \quad (79)$$

where one can conclude that the stress tensor is symmetric [19].

### 2.3.2.3. Part III: satisfying the equation of motion

The final part of Cauchy's theorem states that the stress-tensor satisfies the equation of motion. Consider a body subjected to contact and body forces, as presented in Fig. 16.

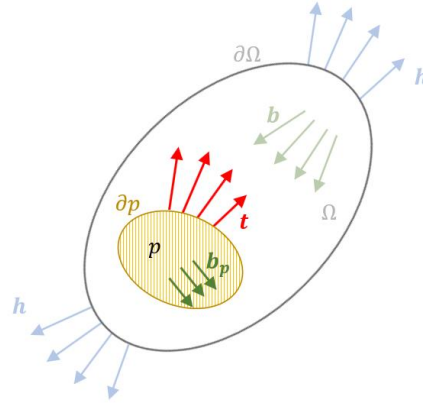


Figure 16 – Solid body where part  $p$  and corresponding forces are evidenced

As previously discussed, a given part  $p$  experiences its own contact forces  $\mathbf{t}$  acting on the boundary  $\partial p$  as well a body forces  $\mathbf{b}_p$  acting upon its volume. According to Newton's second law, the resultant force corresponds to the product between mass and acceleration. Accordingly, balance of linear momentum takes the form [19]

$$\int_{\partial p} \mathbf{t} dA + \int_p \mathbf{b}_p dV = \int_p \rho \frac{d}{dt}(\mathbf{v}) dV. \quad (80)$$

Using expression (66), which states that  $\mathbf{t} = \mathbf{T}\mathbf{n}$ , expression (80) becomes

$$\int_{\partial p} \mathbf{T}\mathbf{n} dA + \int_p \mathbf{b}_p dV = \int_p \rho \frac{d}{dt}(\mathbf{v}) dV. \quad (81)$$

By using the divergence (Gauss) theorem, one obtains

$$\int_p [\operatorname{div}(\mathbf{T}) + \mathbf{b}_p] dV = \int_p \rho \frac{d}{dt}(\mathbf{v}) dV, \quad (82)$$

which can be reduced to

$$\operatorname{div}(\mathbf{T}) + \mathbf{b}_p = \rho \frac{d}{dt}(\mathbf{v}) \quad (83)$$

For a body in equilibrium, the term on the right-hand side turns out to be nil, leading to [19]

$$\text{div}(\mathbf{T}) + \mathbf{b}_p = \mathbf{0}. \quad (84)$$

Expression (84) corresponds to a three-dimensional equation, which in cartesian coordinates corresponds to [19]

$$\left\{ \begin{array}{l} \frac{\partial}{\partial x}(\sigma_{xx}) + \frac{\partial}{\partial y}(\tau_{xy}) + \frac{\partial}{\partial z}(\tau_{xz}) + b_{p,x} = 0 \\ \frac{\partial}{\partial x}(\tau_{xy}) + \frac{\partial}{\partial y}(\sigma_{yy}) + \frac{\partial}{\partial z}(\tau_{yz}) + b_{p,y} = 0 \\ \frac{\partial}{\partial x}(\tau_{xz}) + \frac{\partial}{\partial y}(\tau_{yz}) + \frac{\partial}{\partial z}(\sigma_{zz}) + b_{p,z} = 0. \end{array} \right. \quad (85)$$

### 2.3.3. Principal stresses and spectral decomposition

For a generic stress-state  $\boldsymbol{\sigma}$  the normal stress  $\mathbf{t}$  can be obtained using Cauchy's theorem, as given by  $\mathbf{t} = \boldsymbol{\sigma}\mathbf{n}$ . Accordingly, the normal stress component  $t_n$  can be obtained by projecting  $\mathbf{t}$  to the normal direction  $\mathbf{n}$ , as shown in

$$t_n = \mathbf{n} \cdot (\boldsymbol{\sigma}\mathbf{n}). \quad (86)$$

In order to obtain the maximum (and minimum) value of normal stress, one must find  $\mathbf{n}$  that maximises the above expression, restricted to  $\mathbf{n}$  being a unit vector, leading to

$$\mathbf{n} \cdot \mathbf{n} = 1. \quad (87)$$

Optimisation can be achieved by using Lagrange multipliers, where the Lagrangean function can be presented as

$$\mathcal{L}(\mathbf{n}) = \mathbf{n} \cdot (\boldsymbol{\sigma}\mathbf{n}) - \lambda(\mathbf{n} \cdot \mathbf{n}), \quad (88)$$

where  $\lambda$  is the Lagrange multiplier.

Maxima and minima values are obtained when the partial derivatives of  $\mathcal{L}$  with respect to its arguments equal zero. Accordingly,

$$\frac{\partial}{\partial \mathbf{n}} \{\mathcal{L}(\mathbf{n})\} = 2\boldsymbol{\sigma}\mathbf{n} - 2\lambda\mathbf{n} = \mathbf{0}, \quad (89)$$

leading to

$$\boldsymbol{\sigma}\mathbf{n} = \lambda\mathbf{n}, \quad (90)$$

which is in full agreement with expression (50).

The spectral decomposition theorem states that, for any given symmetric second-order tensor  $\boldsymbol{\sigma}$  exists a right-handed orthonormal basis  $\{\mathbf{e}'_i\}$  constituted of its eigenvectors [15]. Within the context of mechanical behaviour of solids, the eigenvalues  $\lambda_i$  correspond to the values of the maximum stresses and in terms of the basis  $\{\mathbf{e}'_i\}$ , the stress tensor  $\boldsymbol{\sigma}'$  in matrix representation is thus given by

$$\boldsymbol{\sigma}' = \begin{pmatrix} \sigma_1 & 0 & 0 \\ 0 & \sigma_2 & 0 \\ 0 & 0 & \sigma_3 \end{pmatrix}, \quad (91)$$

where  $\sigma_1$ ,  $\sigma_2$  and  $\sigma_3$  correspond to the principal stresses, with  $\sigma_1$  being by convention the highest value and  $\sigma_3$ , by convention, being the lowest.

#### 2.3.4. Hydrostatic and deviatoric stresses

The Cauchy stress-tensor  $\boldsymbol{\sigma}$  can be decomposed into a sum of two parts, as presented in [15]

$$\boldsymbol{\sigma} = \boldsymbol{\sigma}_{Dev} + \sigma_H \mathbf{I}, \quad (92)$$

where  $\boldsymbol{\sigma}_{Dev}$  corresponds to the deviatoric stress-tensor,  $\sigma_H$  is the hydrostatic stress and  $\mathbf{I}$  is the identity tensor. The hydrostatic stress is defined as [15]

$$\sigma_H = \frac{1}{3} tr(\boldsymbol{\sigma}) = \frac{1}{3} \sigma_{ii} = \frac{1}{3} (\sigma_{xx} + \sigma_{yy} + \sigma_{zz}), \quad (93)$$

where the operation  $tr(\boldsymbol{\sigma})$  is the trace of the tensor, which can be represented in index notation as  $\sigma_{ii}$ . Accordingly, the deviatoric stress-tensor can be obtained as [15]

$$\boldsymbol{\sigma}_{Dev} = \boldsymbol{\sigma} - \sigma_H \mathbf{I}, \quad (94)$$

which corresponds in matrix representation to

$$\boldsymbol{\sigma}_{Dev} = \begin{bmatrix} \frac{2\sigma_{xx} - \sigma_{yy} - \sigma_{zz}}{3} & \tau_{xy} & \tau_{xz} \\ \tau_{xy} & \frac{2\sigma_{yy} - \sigma_{xx} - \sigma_{zz}}{3} & \tau_{yz} \\ \tau_{xz} & \tau_{yz} & \frac{2\sigma_{zz} - \sigma_{xx} - \sigma_{yy}}{3} \end{bmatrix}. \quad (95)$$

## 2.4. Relevant concepts of fatigue

### 2.4.1. Uniaxial fatigue

#### 2.4.1.1. Wöhler curves and fatigue resistance limit

In the 19<sup>th</sup> century, fatigue was already a well-known technical problem as several failures of metallic structures were being reported. It had already been recognised that a single load far below the ultimate tensile strength of the material exerted no damage to the structure, but repetition of this load could eventually induce complete failure [1].

Wöhler thus proposed a method of presenting fatigue data by means of a plot that correlated the applied stress amplitudes against number of cycles to failure [20]. Such approach via S-N curves is still popular to this day and is used to assess and design against fatigue behaviour of materials. The S-N curves (or Wöhler curves) are commonly determined for normal *push-pull* condition, typically relating the stress amplitude with the observed fatigue-life. Most determinations of the fatigue properties of materials have been made to fully reversed loadings, where mean stress is nil [20].

Accordingly, from a theoretical perspective, fluctuating loads are commonly modelled as sinusoidal expressions, as given by

$$\sigma(t) = \sigma_m + \sigma_a \sin(\omega t), \quad (96)$$

where  $\sigma_m$  corresponds to the mean stress and  $\sigma_a$  corresponds to the stress amplitude [20].

Fig. 17(a) exemplifies loading histories modelled as sinusoidal curves, with and without mean stress, while Fig. 17(b) presents a generic S-N curve for a metallic material.

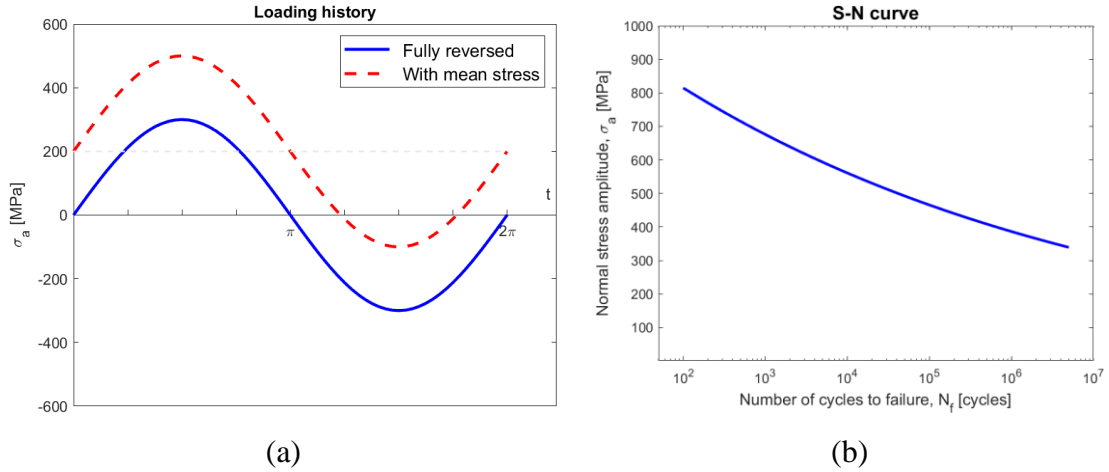


Figure 17 – Loading histories  $\sigma(t)$  as sinusoidal curves, with and without mean stress

As one may observe, stress amplitude  $\sigma_a$  and the number of cycles to failure  $N_f$  are related via a power function, as given by Basquin's expression [21]

$$\sigma_a = AN_f^m, \quad (97)$$

where  $A$  and  $m$  are experimentally determined material constants. For some metallic materials, notably plain-carbon and low alloy steels, the S-N presents an asymptotic behaviour [22]. The value to which the S-N curve converges is known as the endurance limit (or fatigue resistance limit)  $f_{-1}$ , where stress amplitudes below such level are insufficient to drive the material into failure, and the fatigue life is theoretically expected to be infinite.

Analogously, fatigue analysis can also be carried out for pure torsion. The fatigue data can be accordingly presented in a T-N plot, where the relation between shear stress amplitudes and fatigue-life also follows the Basquin expression, as given by [21]

$$\tau_a = A'N_f^{m*}, \quad (98)$$

where  $A'$  and  $m^*$  are material constants. The fatigue resistance limit in pure torsion is addressed to, in the present work, as  $t_{-1}$ .

### 2.4.1.2. Effect of mean stress on fatigue

Fatigue data available in the literature has been predominately determined and made available for conditions of fully reversed loadings. Nevertheless, many in-service conditions are in practice found to present a combination of time-varying loads superimposed to static stresses [20].

Goodman proposed a relation where the limiting range of stress decays linearly with the presence of a mean stress, as given by [1]

$$\sigma_a^{R \neq -1} = \sigma_{a,eq}^{R=-1} \left( 1 - \frac{\sigma_m}{\sigma_u} \right), \quad (99)$$

where  $\sigma_a^{R \neq -1}$  corresponds to a stress amplitude fluctuating around a certain mean value,  $\sigma_{a,eq}^{R=-1}$  corresponds to an equivalent stress amplitude under fully reversed condition,  $\sigma_m$  corresponds to the mean stress value and  $\sigma_u$  corresponds to the ultimate tensile strength of the material.

The above relation can be visualised in the plot presented in Fig. 18, where the admissible stress amplitude  $\sigma_a$  (for a given fatigue-life) linearly decreases with the increase of the mean stress  $\sigma_m$ .

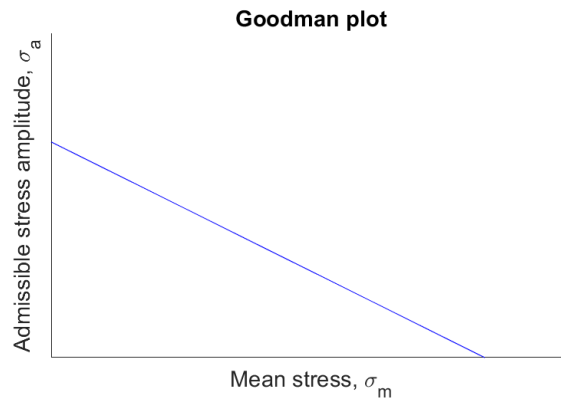


Figure 18 – Goodman plot

It is important to point out that such behaviour is only valid for the case of alternating axial or bending with static normal stress, as well as for the case of alternating torsion with static tension [20], [23]. It is well-established that a superimposed static torsion does not influence the fatigue resistance limit provided that the elastic regime is not exceeded.

## 2.4.2. Multiaxial fatigue

### 2.4.2.1. Stresses acting on material plane

The stress-state acting on a small volume of material in a body is described with the use of six stress components, namely  $\sigma_{xx}$ ,  $\sigma_{yy}$ ,  $\sigma_{zz}$ ,  $\tau_{xy}$ ,  $\tau_{xz}$  and  $\tau_{yz}$ , acting on three orthogonal planes (Fig. 19). Considering that such stress components fluctuate in value over time, the associated stress-tensor is also a function of time, as given by

$$\boldsymbol{\sigma}(t) = \begin{pmatrix} \sigma_{xx}(t) & \tau_{xy}(t) & \tau_{xz}(t) \\ \tau_{xy}(t) & \sigma_{yy}(t) & \tau_{yz}(t) \\ \tau_{xz}(t) & \tau_{yz}(t) & \sigma_{zz}(t) \end{pmatrix}. \quad (100)$$

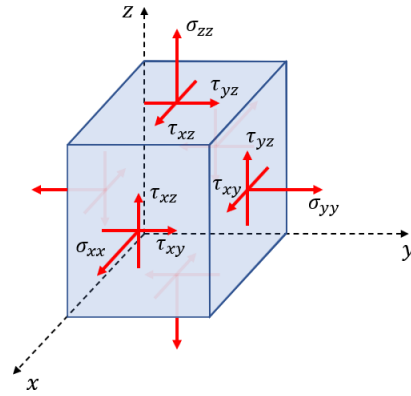


Figure 19 – Time-varying stresses acting on a small volume of material

Assume that a material plane  $\Delta$ , defined uniquely by its unit vector described in spherical coordinates, intercepts the elementary volume as presented in Fig. 20(a) [24]. From Cauchy's theorem, the stress vector  $\mathbf{t}$  acting on  $\Delta$  can be obtained by applying the stress-state tensor  $\boldsymbol{\sigma}$  to the plane's normal vector  $\mathbf{n}$ . The resulting stress vector  $\mathbf{t}$  is also a function of time, as follows

$$\mathbf{t}(t) = \boldsymbol{\sigma}(t) \mathbf{n}. \quad (101)$$

The normal stress vector  $\mathbf{N}(t)$  can be obtained by projecting the stress vector  $\mathbf{t}(t)$  to the direction of  $\mathbf{n}$ . The inner product delivers a scalar quantity that corresponds to the magnitude of  $\mathbf{N}(t)$ , which can be simply referred to as  $N(t)$ . The normal stress vector  $\mathbf{N}(t)$  is therefore obtained by multiplying  $\mathbf{n}$  by its corresponding magnitude  $N(t)$ , as given by [5], [8]

$$\mathbf{N}(t) = (\mathbf{t} \cdot \mathbf{n})\mathbf{n}. \quad (102)$$

Accordingly, the shear stress vector  $\mathbf{C}(t)$  can be obtained by subtracting the normal component  $\mathbf{N}(t)$  from the stress vector  $\mathbf{t}(t)$ , as shown in

$$\mathbf{C}(t) = \mathbf{t}(t) - \mathbf{N}(t). \quad (103)$$

Such decomposition is depicted in Fig. 20(b).

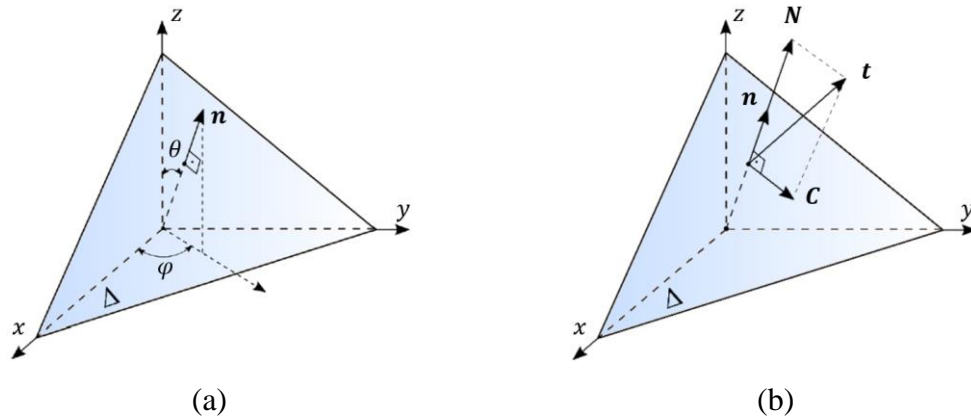


Figure 20 – (a) Material plane  $\Delta$ ; (b) Normal and shear stress vectors

In practical terms, stresses of interest are often not aligned with the coordinate axes. Performing a coordinate transformation is usually a convenient approach to obtain the stress values with respect to material plane  $\Delta$  in question [25].

Fig. 21(a) depicts the change of basis given by an anticlockwise rotation of  $\varphi$  with respect to the  $z$  axis, followed by a clockwise rotation of  $90^\circ - \theta$  with respect to the position where the  $y$  axis landed after the first rotation. Fig. 21(b) presents the final orientation of the reference system in terms of  $(\theta, \varphi)$ .

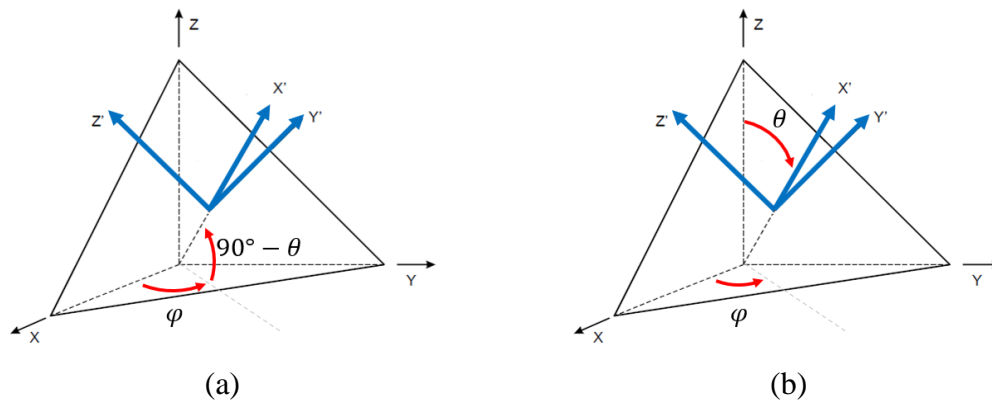


Figure 21 – (a) Rotations applied to the reference system; (b) final orientation of the reference system

The transformation consists of a two-step procedure, with the first corresponding to the anticlockwise rotation of  $\varphi$  with respect to  $z$ , modifying the stress-tensor as follows

$$\bar{\sigma} = \mathbf{Q}_1^T \sigma \mathbf{Q}_1. \quad (104)$$

For the second step, the transformation corresponds to a clockwise rotation with respect to the direction where the  $y$  axis landed after the first transformation. Such expression corresponds to

$$\begin{aligned} \sigma' &= \mathbf{Q}_2^T \bar{\sigma} \mathbf{Q}_2 \\ &= \mathbf{Q}_2^T (\mathbf{Q}_1^T \sigma \mathbf{Q}_1) \mathbf{Q}_2 \\ &= (\mathbf{Q}_2^T \mathbf{Q}_1^T) \sigma (\mathbf{Q}_1 \mathbf{Q}_2) \\ &= (\mathbf{Q}_1 \mathbf{Q}_2)^T \sigma (\mathbf{Q}_1 \mathbf{Q}_2) \end{aligned} \quad (105)$$

where  $\mathbf{Q}_1$  and  $\mathbf{Q}_2$  are respectively given by

$$\mathbf{Q}_1 = \begin{pmatrix} \cos(\varphi) & -\sin(\varphi) & 0 \\ \sin(\varphi) & \cos(\varphi) & 0 \\ 0 & 0 & 1 \end{pmatrix}, \quad \mathbf{Q}_2 = \begin{pmatrix} \sin(\theta) & 0 & -\cos(\theta) \\ 0 & 1 & 0 \\ \cos(\theta) & 0 & \sin(\theta) \end{pmatrix}. \quad (106)$$

The product  $\mathbf{Q}_1 \mathbf{Q}_2$  is given by

$$\mathbf{Q}_1 \mathbf{Q}_2 = \begin{pmatrix} \cos(\varphi) \sin(\theta) & -\sin(\varphi) & -\cos(\varphi) \cos(\theta) \\ \sin(\varphi) \sin(\theta) & \cos(\varphi) & -\sin(\varphi) \cos(\theta) \\ \cos(\theta) & 0 & \sin(\theta) \end{pmatrix}, \quad (107)$$

and, accordingly,  $\mathbf{Q}_2^T \mathbf{Q}_1^T$  is therefore given by

$$\mathbf{Q}_2^T \mathbf{Q}_1^T = (\mathbf{Q}_1 \mathbf{Q}_2)^T = \begin{pmatrix} \cos(\varphi) \sin(\theta) & \sin(\varphi) \sin(\theta) & \cos(\theta) \\ -\sin(\varphi) & \cos(\varphi) & 0 \\ -\cos(\varphi) \cos(\theta) & -\sin(\varphi) \cos(\theta) & \sin(\theta) \end{pmatrix}. \quad (108)$$

Finally, let  $\mathbf{A}$  correspond to  $(\mathbf{Q}_1 \mathbf{Q}_2)^T$ . The stresses acting on the material plane are therefore given by [25]

$$\left\{ \begin{array}{l} N = \sigma_{xx}a_{11}^2 + \sigma_{yy}a_{12}^2 + \sigma_{zz}a_{13}^2 + \\ \quad + 2(\tau_{xy}a_{11}a_{12} + \tau_{xz}a_{11}a_{13} + \tau_{yz}a_{13}a_{12}) \end{array} \right. \quad (109)$$

$$\left\{ \begin{array}{l} C_{x'y'} = \sigma_{xx}a_{11}a_{21} + \sigma_{yy}a_{12}a_{22} + \sigma_{zz}a_{13}a_{23} + \tau_{xy}(a_{11}a_{22} + a_{12}a_{21}) + \\ \quad + \tau_{yz}(a_{12}a_{23} + a_{13}a_{22}) + \tau_{xz}(a_{13}a_{21} + a_{11}a_{23}) \end{array} \right. \quad (110)$$

$$\left\{ \begin{array}{l} C_{x'z'} = \sigma_{xx}a_{11}a_{31} + \sigma_{yy}a_{12}a_{32} + \sigma_{zz}a_{13}a_{33} + \tau_{xy}(a_{11}a_{32} + a_{12}a_{31}) + \\ \quad + \tau_{yz}(a_{12}a_{33} + a_{13}a_{32}) + \tau_{xz}(a_{13}a_{31} + a_{11}a_{33}), \end{array} \right. \quad (111)$$

where  $a_{11}$ ,  $a_{12}$ ,  $a_{13}$ ,  $a_{21}$ ,  $a_{22}$ ,  $a_{23}$ ,  $a_{31}$ ,  $a_{32}$  and  $a_{33}$  correspond to the components of  $\mathbf{A}$ , given in matrix representation as

$$\mathbf{A} = \begin{pmatrix} a_{11} & a_{12} & a_{13} \\ a_{21} & a_{22} & a_{23} \\ a_{31} & a_{32} & a_{33} \end{pmatrix} = \begin{pmatrix} \cos(\varphi) \sin(\theta) & \sin(\varphi) \sin(\theta) & \cos(\theta) \\ -\sin(\varphi) & \cos(\varphi) & 0 \\ -\cos(\varphi) \cos(\theta) & -\sin(\varphi) \cos(\theta) & \sin(\theta) \end{pmatrix}. \quad (112)$$

#### 2.4.2.2. Shear stress amplitude and maximum value of normal stress acting on $\Delta$

For a time-varying stress-state  $\boldsymbol{\sigma}(t)$ , the corresponding normal and shear stresses,  $\mathbf{N}(t)$  and  $\mathbf{C}(t)$ , associated with a material plane  $\Delta$  are also described as function of time. Determination of quantities associated with the normal stress component  $N(t)$  is usually very straightforward as it can be treated as a scalar. Consequently, direct inspection within a loading cycle with a period of  $T$  allows one to obtain the values of normal stress amplitude  $N_a$  and mean normal stress  $N_m$ , as follows [5]

$$N_a = \frac{1}{2} \left\{ \max_{t \in T} N(t) - \min_{t \in T} N(t) \right\} \quad (113)$$

$$N_m = \frac{1}{2} \left\{ \max_{t \in T} N(t) + \min_{t \in T} N(t) \right\}. \quad (114)$$

On the other hand, determination of the shear stress amplitude can be far more complicated as the shear stress vector  $\mathbf{C}(t)$  may change both in magnitude and in direction

throughout a loading cycle [13]. Fig. 22 depicts a closed path described by a generic time-varying shear stress vector  $\mathbf{C}(t)$ .

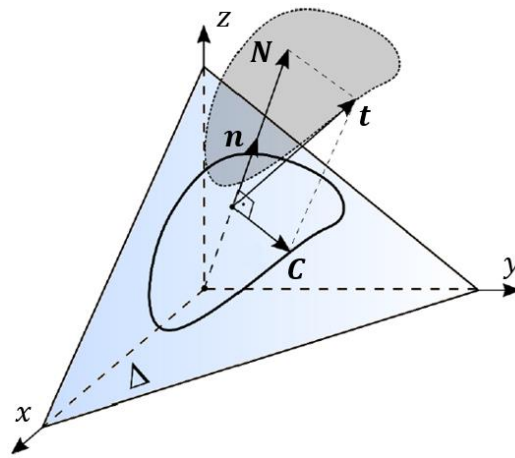


Figure 22 – Closed path described by the shear stress vector on material plane  $\Delta$  within a loading cycle

Several different approaches to determine the shear stress amplitude have been discussed in the literature. Two of the most popular methods correspond to the minimum circumscribed circumference (MCC) [5], [13] and to the maximum rectangular hull (MRH), respectively illustrated in Fig. 23(a) and (b) [26].

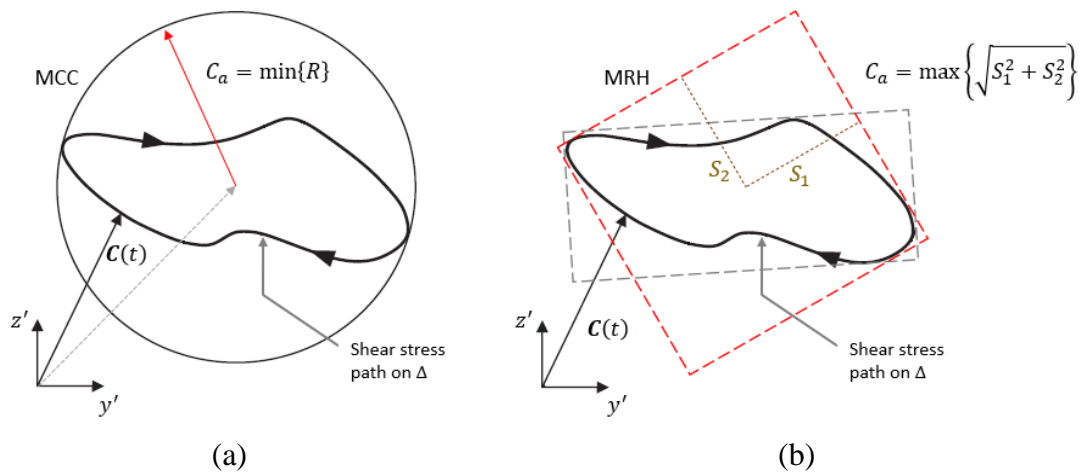


Figure 23 – Determination of the shear stress amplitude: (a) MCC; (b) MRH

The MCC method consists of circumscribing the shear stress path with a circumference, where the shear stress amplitude  $C_a$  for the material plane  $\Delta$  in question corresponds to the radius of the circumference [5], i.e.,  $C_a = \min\{R\}$ . The MRH method consists of

employing axes rotations within the material plane  $\Delta$  to encounter the rectangular hull that maximises the value of the shear stress amplitude [26], as given by  $C_a = \sqrt{S_1^2 + S_2^2}$ , where the quantities  $S_1$  and  $S_2$  corresponds to the half-length of the sides of the rectangular hull.

The MRH method was proposed to overcome a limitation presented by the MCC method. Such limitation refers to the fact that the MCC may indicate that two different loading paths (respectively produced by non-proportional and proportional loadings) may result in the same shear stress amplitude even though the fatigue damage itself may be physically different.

Fig. 24 illustrates two different loading paths,  $\Psi_1$  (non-proportional) and  $\Psi_2$  (proportional), associated with two different loading conditions, where the latter is typically the case of synchronous sinusoidal in-phase normal and shear stress loadings. As one may observe in Fig. 24(a), both shear stress paths are circumscribed by the same circumference therefore resulting, according to the MCC method, in the same shear stress amplitude. Fig. 24(b), on the other hand, presents how the aforementioned paths result in different prismatic hulls, therefore illustrating the sensitivity of the MRH method to non-proportionality.

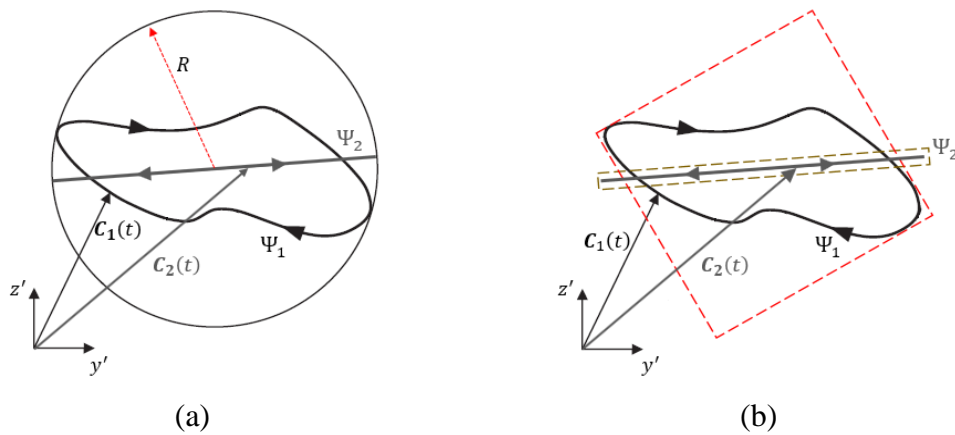


Figure 24 – (a) Drawback on shear stress amplitude estimation; (b) sensitivity to non-proportionality

### 2.4.2.3. Specimens subjected to combined normal and shear stresses

Papadopoulos [5] analytically described the stresses acting on a material plane  $\Delta$ . Considering hourglass specimens, the reference system is positioned on the free surface where the cross-sectional area is minimum, with the  $x$  axis aligned with the longitudinal direction of the specimen (Fig. 25).

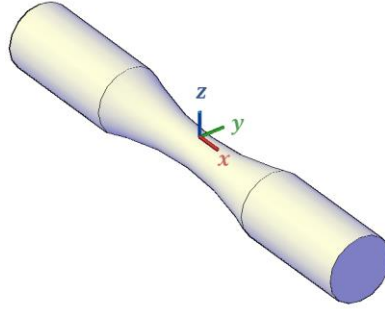


Figure 25 – Positioning of the reference system relative to an hourglass specimen

For combined synchronous sinusoidal normal and shear stresses, the stress-state is expressed as [5]

$$\boldsymbol{\sigma}(t) = \begin{pmatrix} \sigma_{xx}(t) & \tau_{xy}(t) & 0 \\ \tau_{xy}(t) & 0 & 0 \\ 0 & 0 & 0 \end{pmatrix}. \quad (115)$$

The normal and shear stress components,  $\sigma_{xx}(t)$  and  $\tau_{xy}(t)$ , are modelled as sinusoids, as given by

$$\sigma_{xx}(t) = \sigma_m + \sigma_a \sin(\omega t) \quad (116)$$

$$\tau_{xy}(t) = \tau_m + \tau_a \sin(\omega t - \beta), \quad (117)$$

where  $\sigma_a$  and  $\tau_a$  correspond to macroscopically applied normal and shear stress amplitudes, while  $\sigma_m$  and  $\tau_m$  correspond to mean normal and shear stresses. The parameter  $\beta$ , in turn, corresponds to the phase-difference between the normal and shear stresses. As presented in the expressions above,  $\tau_{xy}$  is delayed of  $\beta$  with respect to  $\sigma_{xx}$ .

Accordingly, the stresses acting on any material plane  $\Delta$  are dependent on such plane's orientation, which is in turn oriented relative to the specimen in terms of angles  $(\theta, \varphi)$ ,

as shown in Fig. 26(a). A top view including the normal and shear stresses,  $N(t)$  and  $C(t)$ , acting on  $\Delta$  is presented in Fig. 26(b).

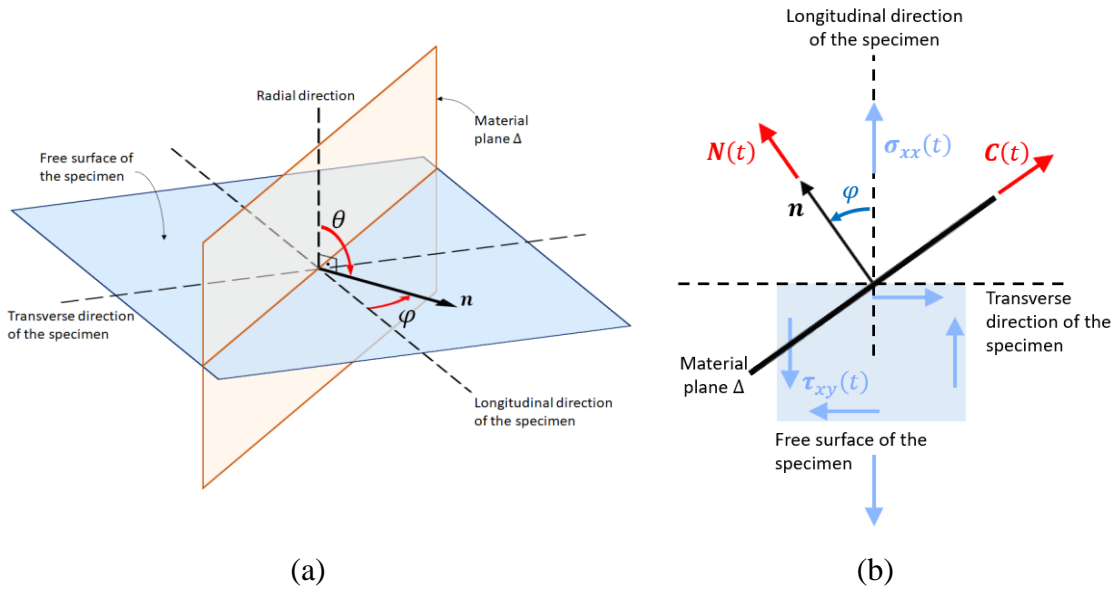


Figure 26 – Material plane  $\Delta$  and free surface of the specimen: (a) free view; (b) top view

For the case of combined synchronous normal and shear loadings, the stresses acting on  $\Delta$  can be analytically determined and expressed in terms of  $\sigma_a$ ,  $\tau_a$ ,  $\sigma_m$ ,  $\tau_m$  and  $\beta$ . The normal stress quantities are therefore given by [5]

$$N_a = \sin^2(\theta) |\cos(\varphi)| \sqrt{\sigma_a^2 \cos^2(\varphi) + 4\tau_a^2 \sin^2(\varphi) + 2\sigma_a\tau_a \sin(2\varphi) \cos(\beta)} \quad (118)$$

$$N_m = \sin^2(\theta) [\sigma_m \cos^2(\varphi) + \tau_m \sin(2\varphi)]. \quad (119)$$

For critical plane-based models, the maximum value attained by the normal stress  $N_{max}$  is a quantity of interest. As such, the  $N_{max}$  can be evaluated as [5]

$$N_{max} = N_a + N_m. \quad (120)$$

In regard to the other quantity of interest, the shear stress amplitude  $C_a$  is given by [5]

$$C_a = \sqrt{\frac{f^2 + g^2 + p^2 + q^2}{2}} + \sqrt{\left(\frac{f^2 + g^2 + p^2 + q^2}{2}\right)^2 - (fq - gp)^2}, \quad (121)$$

where  $f$ ,  $g$ ,  $p$  and  $q$  are auxiliary functions given by

$$f = \sin(\theta) \left[ -\frac{\sigma_a}{2} \sin(2\varphi) + \tau_a \cos(2\varphi) \cos(\beta) \right] \quad (122)$$

$$g = -\sin(\theta) [\tau_a \cos(2\varphi) \sin(\beta)] \quad (123)$$

$$p = -\frac{1}{2} \sin(2\theta) [\sigma_a \cos^2(\varphi) + \tau_a \cos(2\varphi) \cos(\beta)] \quad (124)$$

$$q = \frac{1}{2} \sin(2\theta) [\tau_a \sin(2\varphi) \sin(\beta)]. \quad (125)$$

#### 2.4.2.4. Multiaxial fatigue criteria

Five popular critical plane-based criteria, namely Findley (F), Matake (M), McDiardmid (McD), Susmel & Lazzarin (S&L), Carpinteri & Spagnoli (C&S) are considered in the present work. Their corresponding expressions are respectively given by [8], [10]–[13]

$$C_a + k N_{max} \leq f^* \quad (126)$$

$$C_a + \mu N_{max} \leq t_{-1} \quad (127)$$

$$C_a + \frac{t_{-1}}{2 \sigma_u} N_{max} \leq t_{-1} \quad (128)$$

$$C_a + \left[ t_{-1} - \frac{f_{-1}}{2} \right] \frac{N_{max}}{C_a} \leq t_{-1} \quad (129)$$

$$\sqrt{N_{max}^2 + \left( \frac{f_{-1}}{t_{-1}} \right)^2 C_a^2} \leq f_{-1}, \quad (130)$$

where  $C_a$  and  $N_{max}$  are, respectively, the shear stress amplitude and the maximum value attained by the normal stress within a loading cycle, both acting on the critical plane. The constants  $f_{-1}$ ,  $t_{-1}$  and  $\sigma_u$  are material properties, where the first two respectively correspond to fatigue resistance limits for fully reversed bending and fully reversed torsion, while the latter corresponds to the ultimate tensile strength of the material. The remaining parameters  $k$ ,  $f^*$  and  $\mu$  are constants which can be directly evaluated from  $f_{-1}$  and  $t_{-1}$ , as shown in

$$k = \frac{2 - \left(\frac{f_{-1}}{t_{-1}}\right)}{2\sqrt{\frac{f_{-1}}{t_{-1}} - 1}} \quad (131)$$

$$f^* = \sqrt{\frac{f_{-1}^2}{4\left(\frac{f_{-1}}{t_{-1}} - 1\right)}} \quad (132)$$

$$\mu = 2\left(\frac{t_{-1}}{f_{-1}}\right) - 1. \quad (133)$$

In addition, the criterion proposed by Papadopoulos [5] is also a very well-established model. By adopting a mesoscopic scale approach, the criterion aims to evaluate the accumulated crystal plastic strain, thus being independent of critical plane determination. The fatigue behaviour is assessed by considering both material properties and macroscopically applied loads. Its expression is given by

$$\sqrt{\left(\frac{\sigma_a^2}{3} + \tau_a^2\right)} + \alpha \sigma_{H,max} \leq t_{-1}, \quad (134)$$

where  $\sigma_a$  and  $\tau_a$  respectively correspond to the macroscopic normal and shear stress amplitudes,  $\sigma_{H,max}$  corresponds to the maximum value attained by the hydrostatic stress within a loading cycle and  $\alpha$  is a constant that can be directly evaluated from  $f_{-1}$  and  $t_{-1}$ , as shown in [5]

$$\alpha = \frac{t_{-1} - \left(\frac{f_{-1}}{\sqrt{3}}\right)}{\frac{f_{-1}}{3}}. \quad (135)$$

Application of the aforementioned critical-plane models depends on the prior identification of their respective critical planes, where fatigue damage can occur leading to crack nucleation. In order to determine critical planes, one must investigate the stresses acting on several different material planes, identifying the plane which experiences the maximum fatigue damage according to each model's definition. Once critical plane orientations are determined, the corresponding shear stress amplitude  $C_a$  and maximum value of the normal stress  $N_{max}$  according to each criterion can be obtained and therefore directly substituted into expressions (126)-(130). The procedure for critical plane determination relative to each model is briefly discussed as follows.

Findley considers the fatigue damage parameter to be a linear combination of the shear stress amplitude  $C_a$  with the maximum value of the normal stress  $N_{max}$ . Thus, the critical plane  $(\theta_c, \varphi_c)$  relative to Findley's criterion [10] is the one that experiences the maximum value of the fatigue parameter  $C_a + k N_{max}$ .

As for Matake, McDiarmid and Susmel & Lazzarin, the shear stress amplitude  $C_a$  plays a primary role, as fatigue damage is associated with the relative slip between crystallographic planes, which occurs due to shear. The presence of normal stress, in turn, plays a secondary role as it tends to separate crack surfaces, abbreviating the fatigue-life of the component. Therefore, determination of critical plane orientation  $(\theta_c, \varphi_c)$  requires a two-step procedure, where one must select the one or more planes that experience the maximum value of normal stress  $N_{max}$  among a set of pre-selected candidate planes where the shear stress amplitude  $C_a$  attains its maximum value [11]–[13].

Finally, the procedure for Carpinteri & Spagnoli depends on an additional step as the critical plane orientation cannot be directly evaluated from the stresses acting on the material planes. Instead, one must first identify the orientation of the fracture plane, where the maximum value of normal stress  $N_{max}$  is achieved [12]. For plane stress, at least one occurrence of fracture and critical plane takes place at  $\theta = 90^\circ$ . Critical and fracture planes, respectively  $\varphi_c$  and  $\varphi_f$ , differ in their orientations by an angle  $\delta$ , as given by [8]

$$\delta = \frac{3\pi}{8} \left[ 1 - \left( \frac{t_{-1}}{f_{-1}} \right)^2 \right]. \quad (136)$$

Accordingly, critical plane orientation for the C&S criterion corresponds to

$$\varphi_c = \varphi_f + \delta, \quad (137)$$

and its orientation relative to the fracture plane is illustrated in Fig. 27

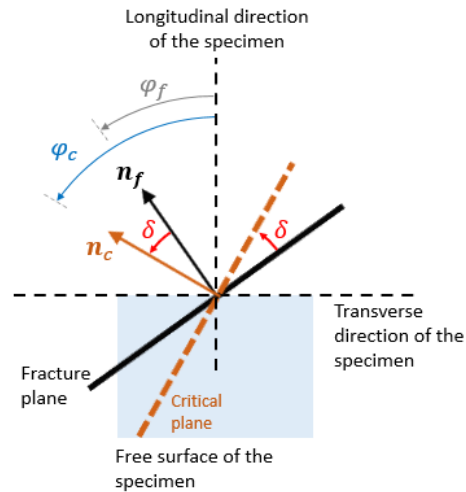


Figure 27 - Critical plane orientation

Equation (137) is valid for the case where  $\varphi$  is situated between  $0^\circ$  and  $90^\circ$ . In many cases a second  $\varphi_f$  is revealed in between  $90^\circ$  and  $180^\circ$ , which must be adequately treated. Application of the involved models are exemplified in Appendix I.

#### 2.4.2.5. Modified C&S criterion for fatigue-life prediction

Although effective, the approach considering infinite fatigue-life stress-based criteria lacks the ability of predicting the number of cycles to failure in case of finite fatigue life. In this sense, Carpinteri & Spagnoli proposed in 2013 a modification to their own model, enabling the criterion to predict the number of cycles to failure [14]. This modification consisted of employing the Basquin expressions [21] in place of fixed values of fatigue resistance limits. Accordingly, the fatigue strength  $f'_{-1}$  for fully reversed normal stress at finite life  $N_f$  can be expressed as [14]

$$f'_{-1} = f_{-1} \left( \frac{N_f}{N_0} \right)^m, \quad (138)$$

where  $N_0$  is the reference number of loading cycles taken as  $2 \times 10^6$ . The parameter  $f_{-1}$  corresponds to the fatigue strength limit and  $m$  corresponds the slope of the Wöhler curve. Likewise, the fatigue strength limit  $t'_{-1}$  for pure torsion can be expressed as [14]

$$t'_{-1} = t_{-1} \left( \frac{N_f}{N_0} \right)^{m*}, \quad (139)$$

where  $m^*$  is the slope of the Wöhler curve for fully reversed shear stress and  $t_{-1}$  is the fatigue resistance limit in pure torsion. Accordingly, for a fatigue life of  $N_f$  cycles, equation (130) can be rewritten as [14]

$$\sqrt{\left[ N_{max}^2 + \left( \frac{f_{-1}}{t_{-1}} \right)^2 \left( \frac{N_f}{N_0} \right)^{2m} \left( \frac{N_0}{N_f} \right)^{2m*} C_a^2 \right]} = f_{-1} \left( \frac{N_f}{N_0} \right)^m. \quad (140)$$

As one may observe, expression (140) corresponds to a non-linear expression with no analytical solution. The solution therefore has to be found through iterative numerical procedures, where two of the most popular procedures correspond to Newton-Raphson method [27] and to the bisection method [27]. In order to apply any numerical procedure, expression (140) must be rearranged to

$$N_{max}^2 + \left\{ \left[ \left( \frac{f_{-1}}{t_{-1}} \right)^2 N_0^{2(m*-m)} \right] C_a^2 \right\} N_f^{2(m-m*)} - \left( \frac{f_{-1}}{N_0^m} \right)^2 N_f^{2m} = 0, \quad (141)$$

giving rise to

$$P + QN_f^S - RN_f^T = 0, \quad (142)$$

where  $P$ ,  $Q$ ,  $S$ ,  $R$  and  $T$  turn out to be constant values, respectively given by

$$P = N_{max}^2 \quad (143)$$

$$Q = \left[ \left( \frac{f-1}{t-1} \right)^2 N_0^{2(m*-m)} \right] C_a^2 \quad (144)$$

$$R = \left( \frac{f-1}{N_0^m} \right)^2 \quad (145)$$

$$S = 2(m - m^*) \quad (146)$$

$$T = 2m. \quad (147)$$

Accordingly, expression (142) can be treated as a generic one-variable function, as given by

$$P + QN^S - RN^T = y, \quad (148)$$

where  $P$ ,  $Q$ ,  $S$ ,  $R$  and  $T$  are known. The root of this expression satisfies the Modified C&S criterion, and therefore corresponds to the number of cycles to failure predicted  $N_f$ , as presented in Fig. 28.

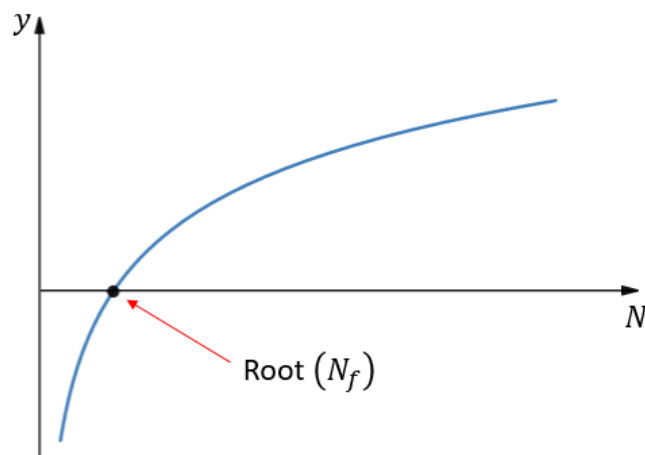


Figure 28 – Solution to the modified C&S expression

Finally, the above-mentioned numerical procedures to solve expression (141) are briefly discussed. Starting with Newton-Raphson method, let  $f(x)$  be a function of interest, to which the root is unknown. By admitting an initial guess  $x_G$  as a hypothetical root of  $f$ , one seeks for the linear curve tangent to  $f$  at  $x_G$ . Unless the initial guess is an extreme value (where the derivative is nil), the linear function is expected to intercept the abscissa at a certain value of  $x_{G+1}$ . The value of  $x_G$  is thus updated to the corresponding value of  $x_{G+1}$ , and the procedure is repeated until the distance between two consecutive steps is revealed to be sufficiently small, within a given pre-established tolerance [27]. This procedure depends on a good initial guess and solution is very commonly obtained within a few iterative steps, usually with quite good precision. However, under some circumstances, the procedure may not converge.

The bisection method consists of defining an initial interval within the domain of  $f(x)$ , to which the desired root is expected do pertain. The procedure divides the interval in half (at  $x_H$ ) and verifies if, for this particular value of  $x_H$ , the signal of the function has changed in comparison to the beginning of the interval. If it has, the second half of the interval is discarded. If not, then the first half is discarded. The procedure is repeated to the remaining part of the interval until the magnitude of the remaining interval is under a certain tolerance value [27]. The present works utilises the bisection method.

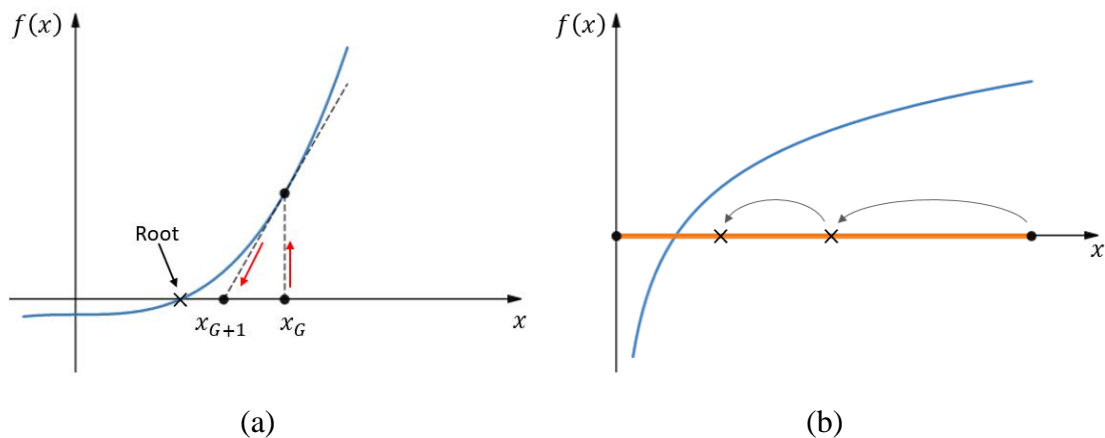


Figure 29 – (a) Newton-Raphson method; (b) bisection method

### 3. Methods

#### 3.1. Proposition of the elliptical curve method

Assuming the existence of a function  $G$ , which establishes a direct relation between the number of cycles to failure and the loading stress amplitudes, a set of  $(\sigma_a, \tau_a)$  combinations associated with a fixed value of fatigue life determines a level curve of  $G$ . The generalisation of such level curve may provide an expression where any generic  $N_f$  can be determined as function of  $\sigma_a$  and  $\tau_a$ .

Using the C&S criterion presented in expression (140) as a survey tool, an iterative procedure was thus implemented to identify a set of coordinate pairs associated with fixed values of  $N_f$ , aiming to build a level curve. The procedure consisted of choosing a combination of  $\sigma_a$  and  $\tau_a$  as input parameters and selecting a fatigue-life value of interest. While holding one of the input parameters as constant, the procedure iteratively sweeps through different values of the other. For each step of the procedure, the critical plane is determined as well as the quantities  $C_a$  and  $N_{max}$  and the corresponding value of  $N$ . The procedure is then repeated until  $N$  converges to the desired value of  $N_f$ , and the resulting  $(\sigma_a, \tau_a)$  combination that delivered such fatigue life is then registered.

Ten different  $(\sigma_a, \tau_a)$  combinations associated with a fixed value of  $N_f$  are shown in Fig. 30. The distribution of the coordinate pairs across the  $\sigma_a \times \tau_a$  domain presents an elliptical symmetry, and the relation between  $\sigma_a$  and  $\tau_a$  for a certain fatigue life can be represented by

$$\frac{\sigma_a^2}{(f'_{-1})^2} + \frac{\tau_a^2}{(t'_{-1})^2} = 1 \quad (149)$$

where the semi-major and semi-minor axes of the ellipse,  $f'_{-1}$  and  $t'_{-1}$ , respectively correspond to uniaxial stress amplitudes for normal and torsional loadings leading to the same fatigue life.

The behaviour described by expression (149) was also perceived by Gough *et al.* [25], [28], [29], where an extensive set of experiments were carried out to determine the fatigue resistance limit in combined loading. As a result, they plotted the observed fatigue resistance limit for combined loading as a summation of the ratios between stress

amplitudes in bending and torsion to their corresponding fixed values of uniaxial fatigue resistance limits, also giving rise to an elliptical symmetry. Such a result can be obtained by substituting the uniaxial fatigue resistance limits in place of the  $f'_{-1}$  and  $t'_{-1}$  in expression (149). Using Basquin's relation,  $f'_{-1}$  and  $t'_{-1}$  can be expressed as

$$f'_{-1} = A N_f^m \quad (150)$$

$$t'_{-1} = A' N_f^{m*}, \quad (151)$$

leading to the general equation of the elliptical curve method (E), as given by

$$\left( \frac{\sigma_a}{A N_f^m} \right)^2 + \left( \frac{\tau_a}{A' N_f^{m*}} \right)^2 = 1. \quad (152)$$

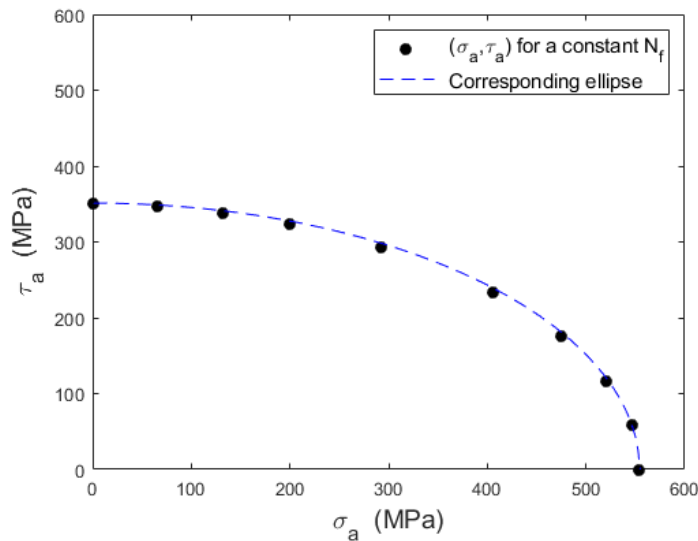


Figure 30 – Elliptical level curve associated with a constant fatigue-life

The elliptical curve method does not only establish a boundary between safe and unsafe regions in the  $\sigma_a \times \tau_a$  domain for a given fatigue life, but it also provides a simple method of predicting  $N_f$  associated with any given  $(\sigma_a, \tau_a)$  combination. The prediction can be obtained by enumeration, where one can iteratively sweep through different values of  $N_f$  until the quadratic sum converges to 1. The precision of the elliptical curve method (E) is tested in a set of experiments, where experimentally observed fatigue lives and predicted number of cycles to failure are compared.

### 3.2. Adaptation of other stress-based criteria for fatigue-life prediction

Carpinteri & Spagnoli proposed an adaptation to their own model for fatigue life prediction [14] by replacing the fixed values of fatigue resistance limits  $f_{-1}$  and  $t_{-1}$ , associated with a fatigue life  $N_0$  of  $2 \times 10^6$  cycles, by variable fatigue resistance limits  $f'_{-1}$  and  $t'_{-1}$  that are dependent on the fatigue life, as given by expressions (138) and (139), or equivalently by expressions (150) and (151).

By implementing the same approach to the other previously cited criteria, one can compare their predictions with those made using the elliptical curve method (E). Accordingly, all predictions can thus be compared with experimental results.

For finite fatigue life  $N_f$ , the parameters  $k$ ,  $f^*$ ,  $\mu$  and  $\alpha$ , previously mentioned in equations (131)-(133) and (135), can be rewritten as

$$k' = \frac{2 - \left( \frac{A N_f^m}{A' N_f^{m*}} \right)}{2 \sqrt{\frac{A N_f^m}{A' N_f^{m*}} - 1}} \quad (153)$$

$$f'^* = \sqrt{\frac{(A N_f^m)^2}{4 \left( \frac{A N_f^m}{A' N_f^{m*}} - 1 \right)}} \quad (154)$$

$$\mu' = 2 \left( \frac{A' N_f^{m*}}{A N_f^m} \right) - 1 \quad (155)$$

$$\alpha' = \frac{A' N_f^{m*} - \left( \frac{A N_f^m}{\sqrt{3}} \right)}{\frac{A N_f^m}{3}}. \quad (156)$$

Accordingly, expressions (126)-(130) and (134) can thus be rewritten, giving rise to the adapted versions of Findley (F), Matake (M), McDiarmid (McD), Susmel & Lazzarin (S&L) and Papadopoulos (P), as given by

$$C_a + \left[ \frac{2 - \left(\frac{A}{A'} N_f^{m-m^*}\right)}{2\sqrt{\frac{A}{A'} N_f^{m-m^*} - 1}} \right] N_{max} - \sqrt{\frac{(A N_f^m)^2}{4 \left(\frac{A}{A'} N_f^{m-m^*} - 1\right)}} = 0 \quad (157)$$

$$C_a + \left[ 2 \frac{A'}{A} N_f^{m^*-m} - 1 \right] N_{max} - A' N_f^{m^*} = 0 \quad (158)$$

$$C_a + \left[ \frac{A' N_f^{m^*}}{2 \sigma_u} \right] N_{max} - A' N_f^{m^*} = 0 \quad (159)$$

$$C_a + \left[ A' N_f^{m^*} - \frac{A N_f^m}{2} \right] \frac{N_{max}}{C_a} - A' N_f^{m^*} = 0 \quad (160)$$

$$\sqrt{\left(\frac{\sigma_a^2}{3} + \tau_a^2\right)} + \left[\frac{A'}{A} \sigma_a\right] N_f^{m^*-m} - \left[\frac{\sqrt{3}}{3} \sigma_a\right] - A' N_f^{m^*} = 0, \quad (161)$$

where expression (161) is valid for the case of fully reversed loadings, as the mean normal stress  $\sigma_m$  is nil, and hence the maximum hydrostatic stress  $\sigma_{H,max}$  will be given by

$$\sigma_{H,max} = \frac{\sigma_a + \sigma_m}{3} = \frac{\sigma_a}{3}. \quad (162)$$

Regarding the C&S criterion, the fatigue resistance limits may be obtained by extrapolation using expressions (97) and (98) to a fatigue-life of  $N_0$ , where  $f_{-1}$  and  $t_{-1}$  respectively turn out to be  $A N_0^m$  and  $A' N_0^{m^*}$ . By squaring both sides of equation (141) and by conducting some algebraic manipulation, the C&S criterion becomes

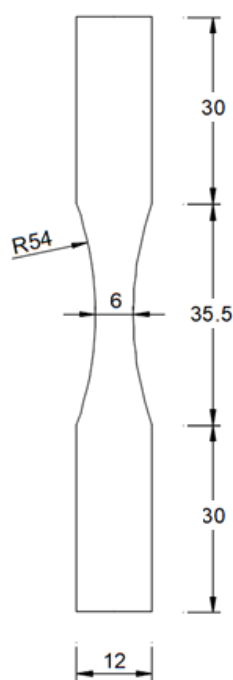
$$N_{max}^2 + \left[ \left(\frac{A}{A'}\right)^2 C_a^2 \right] N_f^{2(m-m^*)} - A^2 N_f^{2m} = 0. \quad (163)$$

Except for the Papadopoulos criterion, given by equation (161), all the other models require the prior identification of critical plane, as previously described, to determine the shear stress amplitude  $C_a$  and maximum value of the normal stress  $N_{max}$  acting on the critical plane. Once these values are known,  $N_f$  according to each model can be determined by enumeration by varying its value until expressions (157)-(161) and (163) converge to zero.

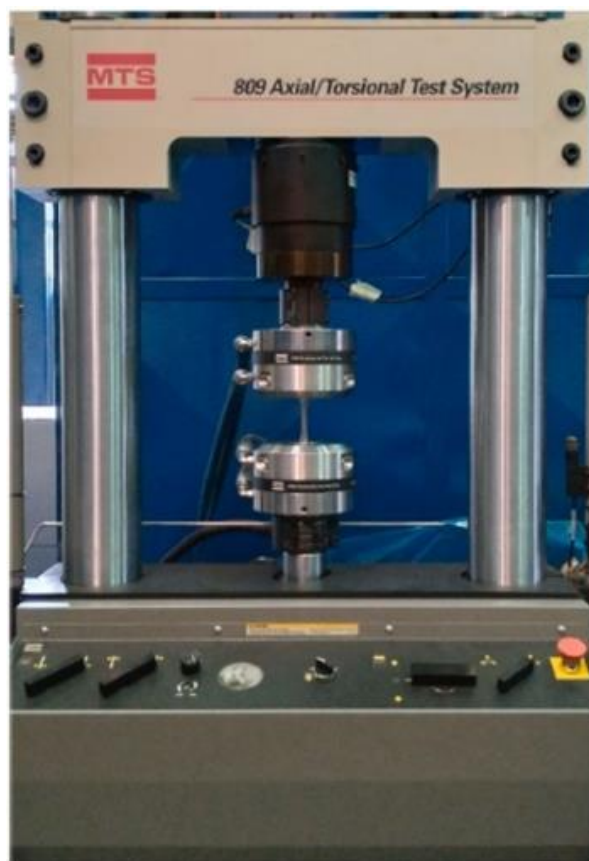
### 3.3. Material and experimental approach

The material considered in this work was a DIN 42CrMo4 steel, extracted from a motor crankshaft that experienced premature failure due to fatigue while in operation within a thermoelectric power plant environment. The crankshaft was sectioned into smaller parts and a certain volume of the material was received. A batch of specimens were machined following the geometry illustrated in Fig. 31(a), which was designed according to an international standard [30]. The machining of the specimens was followed by polishing with 220-2000 grit sandpaper to ensure surface roughness  $Ra$  inferior to  $0.2 \mu\text{m}$ .

Experiments were carried out using an MTS 809 axial/torsional testing system (100 kN / 1100 Nm), depicted in Fig. 31(b). Tests were performed at room temperature using a frequency of 4.5 Hz, which indicates a test duration of 3-6 hours necessary for establishing the elliptic arc corresponding to a fatigue life of 40,000 cycles.



(a)



(b)

Figure 31 – (a) Adopted specimen geometry (dimensions in mm); (b) MTS 809 axial/torsional testing system

The mechanical properties of the DIN 42CrMo4 in question are reported in Table 1 [24].

Table 1 – Mechanical properties of the DIN 42CrMo4 steel

Yield strength $\sigma_y$ (MPa)	Ultimate Tensile strength $\sigma_u$ (MPa)	Vickers hardness HV
710	900	320

Using equation (152), a level curve associated with a fatigue life of 40,000 cycles was selected, and a number of  $(\sigma_a, \tau_a)$  combinations pertaining to this curve were considered for fatigue testing. Such loading conditions were determined by the interception of the elliptic arc with fixed  $\tau_a/\sigma_a$  ratios corresponding to  $\infty$ , 4, 2, 1,  $1/2$ ,  $1/4$  and 0. An additional set of loading conditions that are not associated with any particular fatigue life were also selected, where some of the loading conditions follow the  $\tau_a/\sigma_a$  ratios, while others do not. All the tested loading conditions are distributed across the  $\sigma_a \times \tau_a$  domain, as illustrated in Fig. 32, and presented in Tables 2 and 3.

Table 2 – Selected stress amplitudes relative to the 40,000-cycle level curve

Loading condition	$\tau_a/\sigma_a$	$\sigma_a$ (MPa)	$\tau_a$ (MPa)
A	$\infty$	0	346.9
B	4	85.5	341.8
C	2	163.9	327.8
D	1	285.3	285.3
E	$1/2$	406.5	203.3
F	$1/4$	471.8	117.9
G	0	501.7	0

Table 3 – Additional loading conditions not associated with any particular  $N_f$ 

Loading condition	$\tau_a/\sigma_a$	$\sigma_a$ (MPa)	$\tau_a$ (MPa)
H	$\infty$	0	318.7
I	2	149.7	299.3
J	1	257.3	257.3
K	1/2	359.9	179.9
L	0.58	429.3	247.9
M	0.65	350.2	227.7
N	0.39	450	174.7

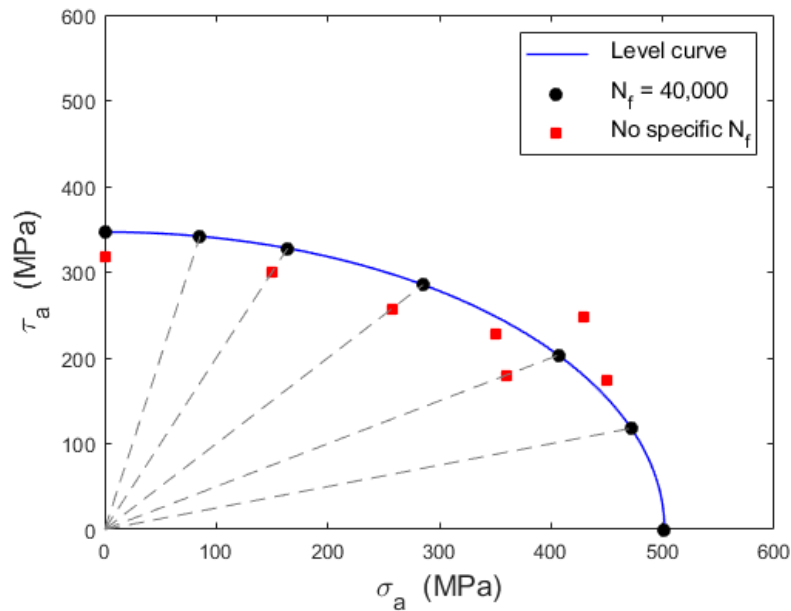


Figure 32 – Loading conditions selected for testing

Lastly, predictions obtained through all the involved criteria are compared to the experimental results using the error index  $I$ , as defined by

$$I = \frac{N_{f,th} - N_{f,exp}}{N_{f,exp}} \times 100\%. \quad (164)$$

This definition establishes the experimental result as the reference value, thus evaluating the deviation of the predictions relative to the experimental observations.

### 3.4. Influence of phase difference

Up to this point, the elliptical curve method (E) has only been considered for predicting the number of cycles to failure  $N_f$  relative to loading conditions that were applied in-phase. Accordingly, inspecting the influence of the out-of-phasesness over the predictive capability of the elliptical curve method therefore arises as a matter of interest.

The nature of fatigue damage due to combined sinusoidal normal and shear stresses is seen to be reduced if the applied sinusoidal normal and shear stresses are out-of-phase [25]. As such, by employing the same iterative procedure used to construct the elliptical level curve discussed in section 3.1 of the present work, different  $(\sigma_a, \tau_a)$  combinations associated with the same fatigue-life were obtained for phase differences of  $0^\circ$ ,  $30^\circ$ ,  $45^\circ$ ,  $60^\circ$ ,  $90^\circ$ ,  $120^\circ$ ,  $135^\circ$  and  $150^\circ$ . The  $(\sigma_a, \tau_a)$  combinations obtained from the procedure followed the same  $\tau_a/\sigma_a$  ratios of 4, 2, 1,  $\frac{1}{2}$  and  $\frac{1}{4}$ .

Based on what is presented in Fig. 33, the introduction of a phase difference deviates the  $(\sigma_a, \tau_a)$  combinations from the previously obtained (in-phase) level curve which is in agreement with the literature, as stress levels have to be raised in order to compensate for the reduction in fatigue damage due to out-of-phasesness. Furthermore, it is seen that the maximum deviation occurs along the  $\tau_a/\sigma_a$  ratio of 1 associated with  $\beta$  corresponding to  $90^\circ$ , and phase differences above this value converge back to the ellipsis.

As such, one can therefore conclude that the elliptic construction as elaborated for in-phase loading conditions, represented by expression (152), is in fact, a conservative approach, where stress levels corresponding to  $\beta$  of  $90^\circ$  are approximately 23% higher than those associated with a  $\beta$  of  $0^\circ$  (Table 4).

Table 4 – Stress levels as function of  $\beta$  for a  $\tau_a/\sigma_a$  ratio of 1 relative to a constant value of fatigue life

$\beta$ ( $^\circ$ )	$\sigma_a$ (MPa)	$\tau_a$ (MPa)
0	292.7	292.7
30	300.2	300.2
45	309.7	309.7
60	323.2	323.2
90	359.4	359.4
120	291.9	291.9
135	292.2	292.2
150	292.5	292.5

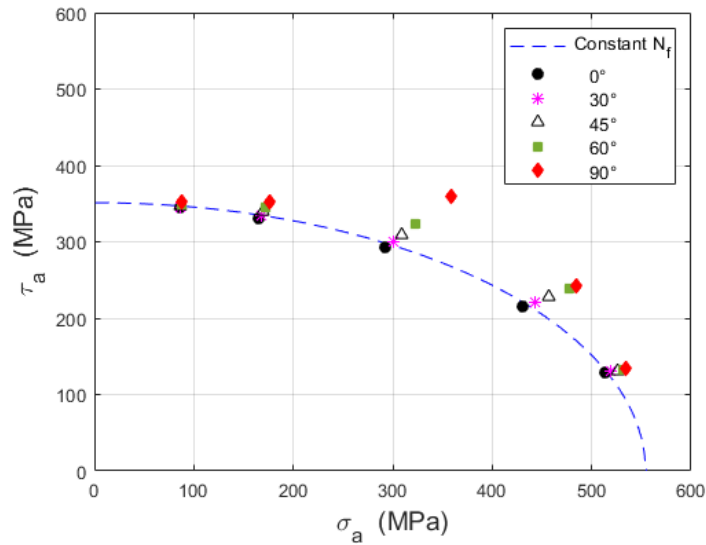


Figure 33 – Influence of phase difference for a given constant fatigue-life

Since  $\beta$  corresponding to  $90^\circ$  is the phase difference that produces the highest deviation, six different experimental results with such a phase difference were collected from the literature [24] and used to provide the required experimental evidence for the influence of the phase difference. It is important to mention that the specimens used in the cited reference were machined from the same DIN 42CrMo4 steel and extracted from the same crankshaft as were the specimens used in the present work. Such loading conditions are presented in Table 5, along with their experimentally observed fatigue-lives.

The adapted versions of Findley (F), Matake (M), McDiarmid (McD), Susmel & Lazzarin (S&L), Carpinteri & Spagnoli (C&S) and Papadopoulos (P) criteria, as well as the elliptical curve method (E) were applied to such out-of-phase loading conditions. The first five models take into consideration the phase difference  $\beta$  to determine  $C_a$  and  $N_{max}$  acting on the critical plane, as discussed in expressions (118)-(125), while the last two do not.

The life diagrams presented in Fig. 34 compare the predicted and the experimentally observed [24] fatigue-life values, revealing that the criteria that do not take the phase difference  $\beta$  into consideration do, in fact, present a better predictive capability for loading conditions which are out-of-phase. As one may observe (Fig. 34),  $\beta$ -dependent criteria delivered predictions that were spread across 3 to 4 orders of magnitude, greatly

differing from the experimentally observed lives that ranged between  $3 \times 10^5$  cycles and  $1.7 \times 10^6$  cycles. On the other hand,  $\beta$ -independent criteria produced predictions that were in much better agreement with the experiments, where all the predictions remained within a range of  $2 \times 10^5$  to  $1.2 \times 10^6$  cycles. Therefore, one may conclude that it is appropriate to maintain the expression of the elliptical curve method as presented in equation (152), without the inclusion of the parameter  $\beta$ .

Table 5 – Stress levels  $\beta$  corresponding to  $90^\circ$  for a  $\tau_a/\sigma_a$  ratio of 1

Loading conditions	$\sigma_a$ (MPa)	$\tau_a$ (MPa)	$\beta$ ( $^\circ$ )	Experimental $N_f$
P1	230	230	90	771,198
P2	230	230	90	1,649,979
Q1	300	150	90	733,995
R1	320	160	90	750,695
R2	320	160	90	352,444
S1	140	280	90	1,039,328

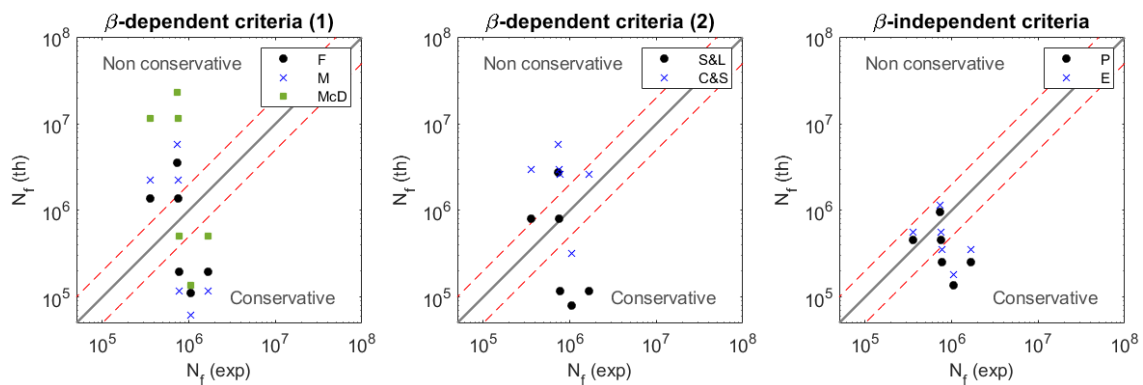


Figure 34 – Comparison of the predictive capability of  $\beta$ -dependent and  $\beta$ -independent criteria

## 4. Results

### 4.1. Uniaxial fatigue tests

Uniaxial experiments were carried out to determine the Wöhler curves associated with the DIN 42CrMo4 steel. The results are presented in Table 6 along with the resulting Wöhler curves presented in Fig. 35. The corresponding Basquin equations obtained for fully reversed push-pull and torsional experiments are given by

$$\sigma_a = 1183.6 N_f^{-0.081} \quad (165)$$

$$\tau_a = 1089.4 N_f^{-0.108}, \quad (166)$$

leading to

$$\begin{aligned} A &= 1183.6 \\ m &= -0.081 \\ A' &= 1089.4 \\ m^* &= -0.108. \end{aligned} \quad (167)$$

By extrapolating the curves to  $N_0 = 2 \times 10^6$  cycles, the uniaxial fatigue resistance limits for fully reversed normal and shear stresses, respectively  $f_{-1}$  and  $t_{-1}$ , given by expressions (165) and (166) turn out to be

$$f_{-1} = 365 \text{ MPa} \quad (168)$$

$$t_{-1} = 227 \text{ MPa}. \quad (169)$$

Table 6 – Results for uniaxial fully reversed tests

Normal <i>push-pull</i> experiments		Torsional experiments	
$\sigma_a$ (MPa)	$N_f$ (cycles)	$\tau_a$ (MPa)	$N_f$ (cycles)
642	1,400	500	1,192
609	3,395	444	5,493
573	11,598	413	9,574
537	34,698	392	11,805
503	64,748	372	12,261
466	72,000	351	37,193
428	156,280		

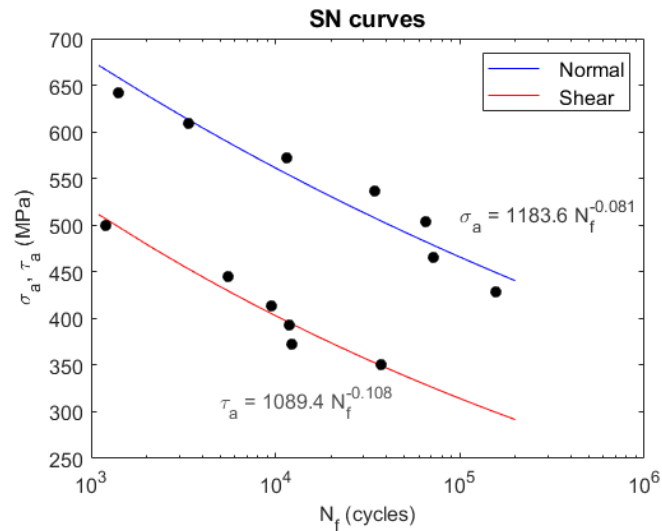


Figure 35 – Resulting Wöhler curves and corresponding Basquin expressions

## 4.2. Multiaxial fatigue predictions

Table 7 presents the experimental results relative to each of the selected loading conditions, as well as the predicted values obtained using the elliptical curve method (E). The last column presents the corresponding values of the error index  $I$  as defined in expression (164). Negative  $I$  values, on the one hand, correspond to conservative predictions, once the experimentally observed life exceeds the predicted value. On the other hand, positive  $I$  values correspond to non-conservative situations, where the predicted fatigue lives are greater than those observed in fatigue tests.

In addition, the adapted versions of Findley (F), Matake (M), McDiarmid (McD), Susmel & Lazzarin (S&L), Carpinteri & Spagnoli (C&S) and Papadopoulos (P) criteria were also applied to the same loading conditions, thus producing predictions of their own. The predictive capabilities of all the involved criteria are presented using fatigue life diagrams shown in Fig. 36, where a scatter band defined by a factor of 2 is delimited by the diagonal dashed lines. Results within this band indicate a fair agreement between predictions and experimental observations.

All predictions were compared to the experimental results by using the definition of error index presented in expression (164). The comparison is presented in Table 8, while the overall behaviour of each model can be assessed in Fig. 37, where the error indices are grouped and presented in the form of frequency histograms.

Table 7 – Comparison of predictions obtained via elliptical curve method vs. experimental results

Loading condition	$\tau_a/\sigma_a$	$\sigma_a$ (MPa)	$\tau_a$ (MPa)	Predicted $N_f$ (cycles)	Experimental $N_f$ (cycles)	Error Index (%)
A	$\infty$	0	346.9	40,000	48,561	-18
				40,000	42,644	-6
				40,000	37,193	8
B	4	85.5	341.8	40,000	54,890	-27
				40,000	41,458	-4
C	2	163.9	327.8	40,000	79,676	-50
				40,000	73,427	-46
D	1	285.3	285.3	40,000	73,721	-46
				40,000	71,097	-44
E	1/2	406.5	203.3	40,000	60,628	-34
				40,000	86,588	-54
F	1/4	471.8	117.9	40,000	102,954	-61
				40,000	32,153	24
				40,000	89,422	-55
G	0	501.7	0	40,000	31,376	27
				40,000	64,748	-38
H	$\infty$	0	318.7	87,699	190,806	-54
				87,699	213,990	-59
				87,699	145,776	-40
I	2	149.7	299.3	95,021	326,157	-71
				95,021	422,563	-78
J	1	257.3	257.3	113,143	107,430	5
				113,143	247,769	-54
K	1/2	359.9	179.9	153,762	502,399	-69
L	0.58	429.3	247.9	12,245	28,941	-58
M	0.65	350.2	227.7	63,038	75,769	-17
N	0.39	450	174.7	28,939	37,800	-23

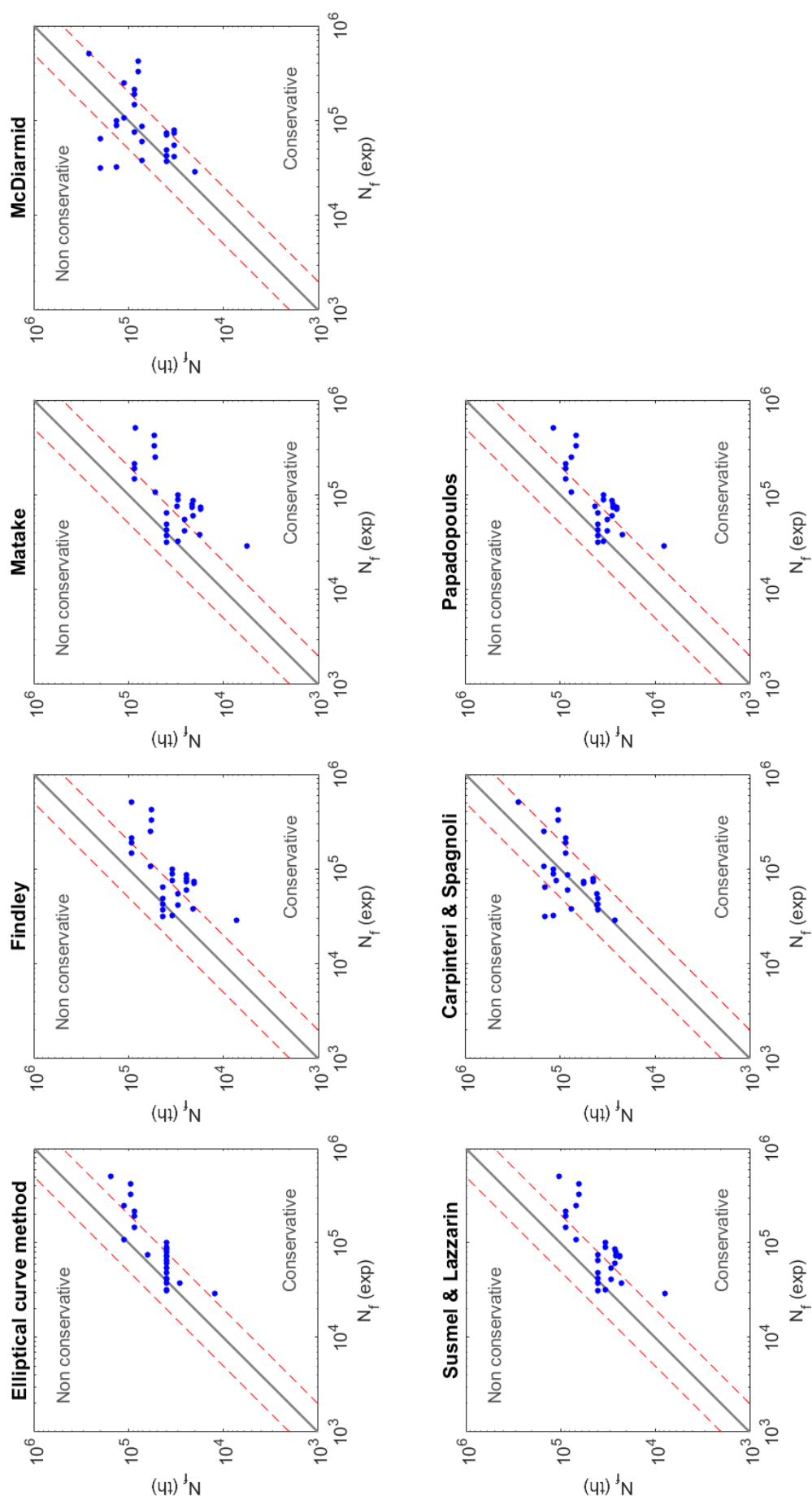


Figure 36 – Fatigue-life prediction compared to experimental observations

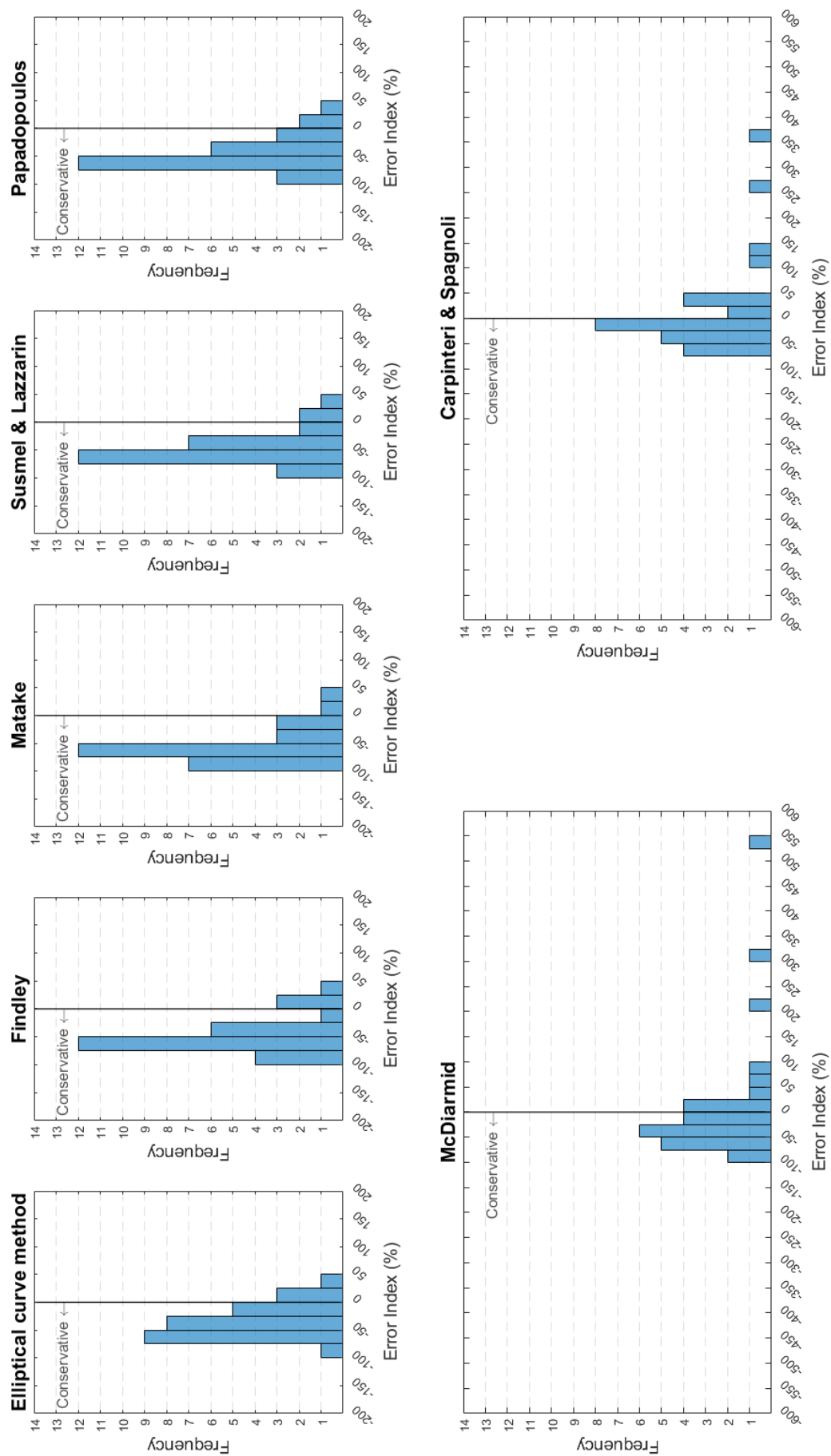


Figure 37 – Frequency histograms of the error indices obtained from each multiaxial fatigue criterion (data in Table 8)

Table 8 – Deviation of each prediction relative to its corresponding experimental observation

<b>F (%)</b>	<b>M (%)</b>	<b>McD (%)</b>	<b>S&amp;L (%)</b>	<b>C&amp;S (%)</b>	<b>P (%)</b>	<b>E (%)</b>
-9	-18	-18	-18	-18	-18	-18
3	-6	-6	-6	-6	-6	-6
19	8	8	8	8	8	8
-45	-53	-39	-46	-25	-42	-27
-27	-38	-20	-29	-1	-23	-4
-70	-73	-59	-67	-44	-65	-50
-67	-71	-55	-64	-39	-62	-46
-72	-76	-46	-68	-24	-66	-46
-71	-75	-44	-67	-21	-64	-44
-60	-66	20	-56	38	-52	-34
-72	-76	-16	-69	-3	-67	-54
-66	-70	35	-66	18	-65	-60
7	-6	322	5	268	9	24
-62	-66	52	-62	32	-61	-55
40	27	539	27	365	27	27
-32	-38	209	-38	125	-38	-38
-51	-54	-54	-54	-54	-54	-54
-56	-59	-59	-59	-59	-59	-59
-36	-40	-40	-40	-40	-40	-40
-82	-84	-76	-81	-68	-79	-71
-86	-87	-81	-85	-75	-84	-78
-46	-51	4	-37	40	-29	5
-76	-79	-55	-73	-39	-69	-54
-81	-83	-48	-79	-45	-77	-69
-75	-80	-30	-73	-7	-72	-58
-54	-59	16	-47	45	-43	-17
-45	-52	89	-41	101	-41	-23

## 5. Discussion

Considering the error indices relative to the elliptical curve method (E) presented in Table 7, a fair agreement between predicted lives and experimentally observed  $N_f$  values is shown to exist. Given that good predictions produce error indices close to nil, and that negative error indices correspond to a conservative behaviour of the model, the predictions made using the elliptical curve method (E) were found to be predominantly conservative, as twenty-three among a total of twenty-seven error indices presented negative values. One may also add that two of the positive values are considerably close to nil. Furthermore, considering the scatter band defined by a factor of 2, the error indices showed that seventeen among twenty-seven predictions (63%) fell within such range, also indicating fair accuracy of the elliptical curve method.

As can be observed in Figs. 36 and 37, as well as in Table 8, the other involved criteria also presented fair predictive capabilities, with Findley (F), Matake (M), Susmel & Lazzarin (S&L) and Papadopoulos (P) being also biased towards conservativeness. Carpinteri & Spagnoli (C&S), in turn, presented nineteen predictions out of twenty-seven (70%) within the scatter band of 2, while McDiarmid (McD) presented the same seventeen predictions among twenty-seven (63%) as did the elliptical curve method, but with the first two (C&S and McD) presenting more scattering than the latter (E).

Table 9 presents the statistics relative to each criterion, where the elliptical curve method was seen to present the best average (-35%) associated with a slight bias towards conservativeness, as well as the best standard deviation among all. This result is followed by Papadopoulos (P), Findley (F) and Susmel & Lazzarin (S&L), which presented very similar results with averages corresponding to -46%, -47% and -48%, with respective standard deviations of 29%, 33% and 29%, being in sequence followed by Matake, with an average of -53% and standard deviation of 30%.

The scattering produced by C&S and McD influenced both average and standard deviation, as these were the only models to present non-conservative averages (positive values corresponding to 17% and 20%) as well as considerably higher standard deviation (99% and 136%, respectively) when compared to the other that presented standard deviations of approximately 30%. The scattering for McD and C&S can be clearly perceived in Fig. 11.

Table 9 – Statistics relative to each criterion

	Avg (%)	StdDev (%)	Min (%)	Median (%)	Max (%)	Range (%)
F	-47	33	-86	-56	40	126
M	-53	30	-87	-59	27	115
McD	20	136	-81	-20	539	620
S&L	-48	29	-85	-56	27	112
C&S	17	99	-75	-7	365	440
P	-46	29	-84	-54	27	111
E	-35	29	-78	-44	27	105

When considering a statistical analysis of the error indices, attention is required to the fact that the overall behaviour of a given model cannot be exclusively measured by average values, as positive error indices would cancel out with negative ones. Therefore, an efficient way to complement the assessment of the predictive capabilities of the criteria is to identify the percentage of error indices that fall within a certain range of interest.

Furthermore, a conservative behaviour of a given criterion is typically preferable over an eventual non-conservative tendency, as uncertainties will bias designs towards safety. Therefore, it would be interesting to identify the number of error indices that fall within the conservative part of the scatter band. The result of this analysis is presented in Fig. 38, where E and C&S, both presented 13 occurrences (48%) within such range. In decreasing order, McD (37%), P and S&L (33%), Findley (26%) and M (22%) presented, respectively, 10, 9, 9, 7 and 6 occurrences. In addition, another range of interest corresponds to a situation where the error indices are comprehended within a central range of  $\pm 50\%$ . For this particular case, C&S displays 19 occurrences (70%), while E presents 17 occurrences (63%) within such range. Once again in decreasing order, McD (56%), P and S&L (44%), F (41%) and M (30%) respectively presented 15, 12, 12, 11 and 8 occurrences within the targeted  $\pm 50\%$ .

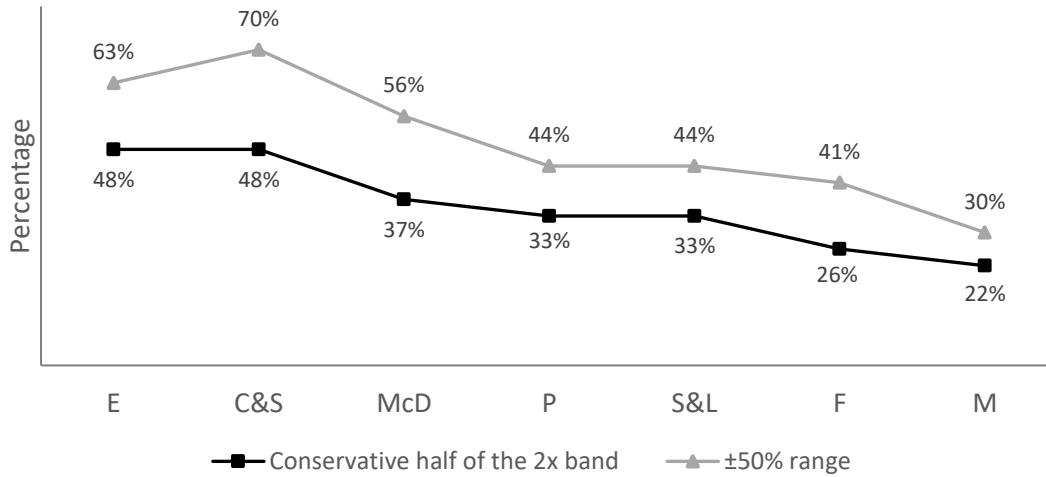


Figure 38 – Percentage of error indices located within the ranges of interest

### 5.1. Adjusting parameter

Although the elliptical curve method has managed to deliver predictions in fair agreement with experimental observations, the predicted  $N_f$  values associated with  $(\sigma_a, \tau_a)$  combinations located at the central region of the elliptical arc were seen to be more conservative than those located closer to the axes. In fact, the experiments have revealed that loading conditions C and D, in Table 7, have driven the specimen to failure after approximately 70,000, instead of the initially predicted 40,000 cycles. Therefore, if one desires to obtain just 40,000 cycles prior to failure, the stress amplitudes  $\sigma_a$  and  $\tau_a$  must be increased so that the number of cycles to failure decreases from 70,000 cycles to 40,000 cycles.

Fig. 39 illustrates how loading conditions C, D and E should be raised to C', D' and E' in order to maintain a fatigue life of 40,000 cycles. Accordingly, an experimental adjustment parameter  $H$  may be required, and hence the adjusted elliptical curve can be represented by

$$\left(\frac{\sigma_a}{A N_f^m}\right)^2 + \left(\frac{\tau_a}{A' N_f^{m*}}\right)^2 = 1 + H, \quad (170)$$

further distancing the above expression from Gough's approach. However, determination of an appropriate expression for  $H$  requires attention, as points A and G, respectively located at the  $\tau_a$  and  $\sigma_a$  axes, correspond to uniaxial loading conditions, and the stress amplitudes associated with a fatigue life of 40,000 cycles must remain consistent with uniaxial fatigue theory.

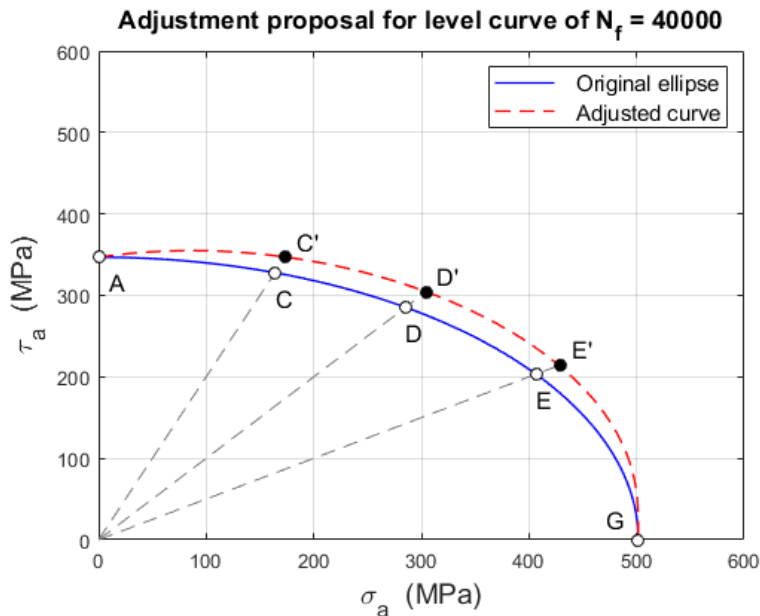


Figure 39 – C, D and E shifted along constant  $\tau_a/\sigma_a$  ratios, while A and G are held fixed

In fact, it can easily be verified that the expression of the elliptical curve method (E), given by equation (152), is consistent with uniaxial fatigue theory, as one may observe that the Basquin's expressions are restored when either  $\sigma_a$  or  $\tau_a$  are set to zero. Consequently, the adjusting parameter must not be a constant, but a function of the variable  $s$ , where  $s$  is defined as the  $\tau_a/\sigma_a$  ratio. It is therefore required that the adjusting parameter  $H(s)$  should be effective only in a certain vicinity of  $\tau_a/\sigma_a = 1$ , shifting the central region of the elliptic arc further away from the origin. Accordingly,  $H(s)$  must tend to zero when  $s$  approaches zero or infinity, not affecting the extremes of the elliptic arc. In this sense, a well-known function that meets the above requirements is given by [31], [32]

$$H(s) = \frac{c_1 s}{s^2 + c_2 s + 1}, \quad (171)$$

which corresponds to the expression of a band-pass filter centred in 1, where  $c_1$  and  $c_2$  are constants associated with overall gain and selectiveness of the filter. This function is seen to have applications in mechanical vibrations [31] as well as in analogue electronics [32]. The overall expression of the adjusted version of the elliptical curve method is therefore given by

$$\left(\frac{\sigma_a}{A N_f^m}\right)^2 + \left(\frac{\tau_a}{A' N_f^{m*}}\right)^2 = 1 + \frac{c_1 \left(\frac{\tau_a}{\sigma_a}\right)}{\left(\frac{\tau_a}{\sigma_a}\right)^2 + c_2 \left(\frac{\tau_a}{\sigma_a}\right) + 1}. \quad (172)$$

Expression (171) presents two very convenient characteristics. The first convenient feature is that it meets the requirement of being centred at 1 as well as decreasing to nil when  $s$  equals zero or when  $s$  tends to infinity. This means that, as long as  $H(s)$  presents the adequate selectivity, it is expected to rectify predictions associated with  $(\sigma_a, \tau_a)$  in the corresponding vicinity of  $\tau_a/\sigma_a$  ratio of 1. The second interesting characteristic is that  $H(s)$  presents a reciprocal symmetry, i.e.,  $H(s)$  and  $H(1/s)$  present identical values. This means that the adjusting parameter evenly adjusts the elliptical arc to both sides with respect to  $\tau_a/\sigma_a = 1$  without introducing asymmetric distortion, as observed in Fig. 39. A generic plot of  $H(s)$  is presented in Fig. 40, where  $c_1$  corresponds to 0.5 and  $c_2$  corresponds to 1.0.

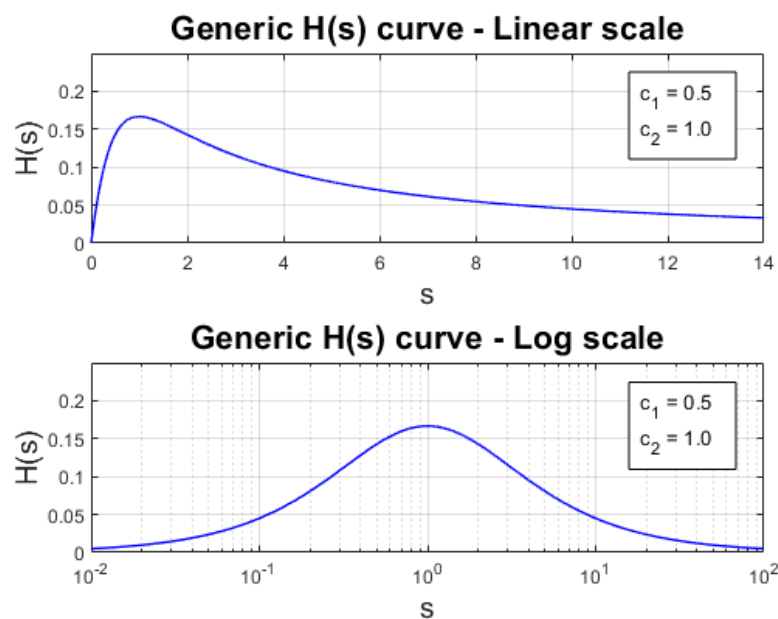


Figure 40 – Generic plot of a band-pass filter function both in linear and log scale

The procedure to determine  $c_1$  and  $c_2$  depends on the experimental data. If equation (152) is applied using a certain combination of experimented  $\sigma_{a,i}$  and  $\tau_{a,i}$  values, the right-hand side (RHS) equals 1 if the fatigue-life introduced into the expression corresponds to the predicted value. However, if one is to consider the same  $\sigma_{a,i}$  and  $\tau_{a,i}$  values while inputting the experimentally observed fatigue-life into expression (152), the RHS of this expression differs from 1 by a certain residual value  $H_i$ , as given by

$$\left[ \frac{\sigma_{a,i}}{A (N_{f,exp})^m} \right]^2 + \left[ \frac{\tau_{a,i}}{A' (N_{f,exp})^{m*}} \right]^2 = 1 + H_i, \quad (173)$$

where  $N_{f,exp}$  corresponds to the experimentally observed fatigue life. Accordingly, for each experiment  $i$ , the residue  $H_i$  can be determined via expression (174), as given by

$$H_i = \left[ \frac{\sigma_{a,i}}{A (N_{f,exp})^m} \right]^2 + \left[ \frac{\tau_{a,i}}{A' (N_{f,exp})^{m*}} \right]^2 - 1. \quad (174)$$

By considering loading conditions pertaining to the inspected elliptical arc (40,000-cycle level curve), the residues  $H_i$  associated with loading conditions B-F (Table 7) were determined and plotted against  $s$ . The corresponding values of  $H_i$  to each experiment are presented in Table 10.

Table 10 – Residues obtained from the experiments associated with a 40,000-cycle fatigue-life

Loading condition	$\sigma_a$	$\tau_a$	$N_{f,exp}$	$\tau_a/\sigma_a$	$H_i$
B1	85.5	341.8	54,890	4	0.0702
B2	85.5	341.8	41,458	4	0.0077
C1	163.9	327.8	79,676	2	0.1560
C2	163.9	327.8	73,427	2	0.1363
D1	285.3	285.3	73,721	1	0.1292
D2	285.3	285.3	71,097	1	0.1211
E1	406.5	203.3	60,628	1/2	0.0780
E2	406.5	203.3	86,588	1/2	0.1498
F1	471.8	117.9	100,354	1/4	0.1675
F2	471.8	117.9	32,153	1/4	-0.0361
F3	471.8	117.9	89,422	1/4	0.1451

By fitting the data according to expression (171), the values of  $c_1$  and  $c_2$  were respectively revealed to be of approximately 0.379 and 0.725, resulting in the plot of  $H(s)$  presented in Fig. 41. At this point, it is important to mention that loading conditions A and G (Table 7) were excluded from this analysis, as they correspond to uniaxial loadings. As such, the adjusted 40,000-cycle level curve indeed corresponds to the one presented in Fig. 39, where the central part of the elliptic arc is shifted away from the origin while points A and G remain unaltered.

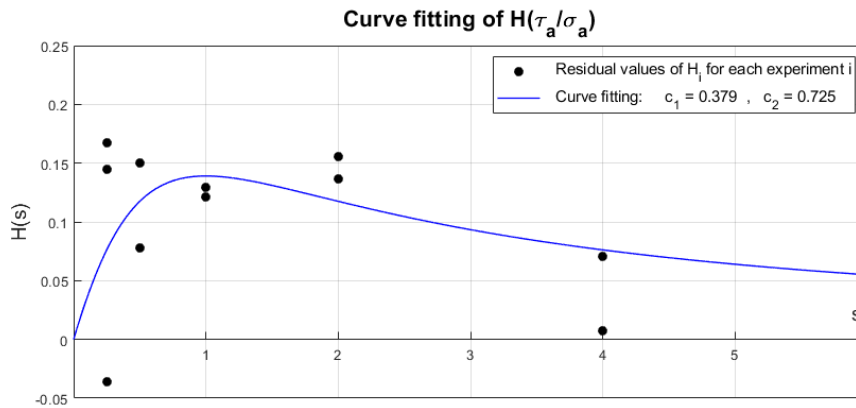


Figure 41 – Curve fitting of  $H(s)$  using residues to obtain the corresponding values of  $c_1$  and  $c_2$

## 5.2. Additional results and discussion

The adjusted version of the elliptical curve method was applied to the same loading conditions presented in Table 7, and the predictions obtained were compared to experimental observations. The resulting error indices are presented in Table 11, and the corresponding life diagram and frequency histogram are presented in Fig. 42.

Table 11 – Error indices relative to the adjusted version of the elliptical curve method

Loading condition	Error Index (%)	Loading condition	Error Index (%)	Loading condition	Error Index (%)
A1	-18	E1	22	H3	-40
A2	-6	E2	-15	I1	-51
A3	8	F1	-38	I2	-62
B1	3	F2	92	J1	102
B2	36	F3	-31	J2	-13
C1	-15	G1	27	K1	-44
C2	-8	G2	-38	L1	-20
D1	4	H1	-54	M1	59
D2	8	H2	-59	N1	34

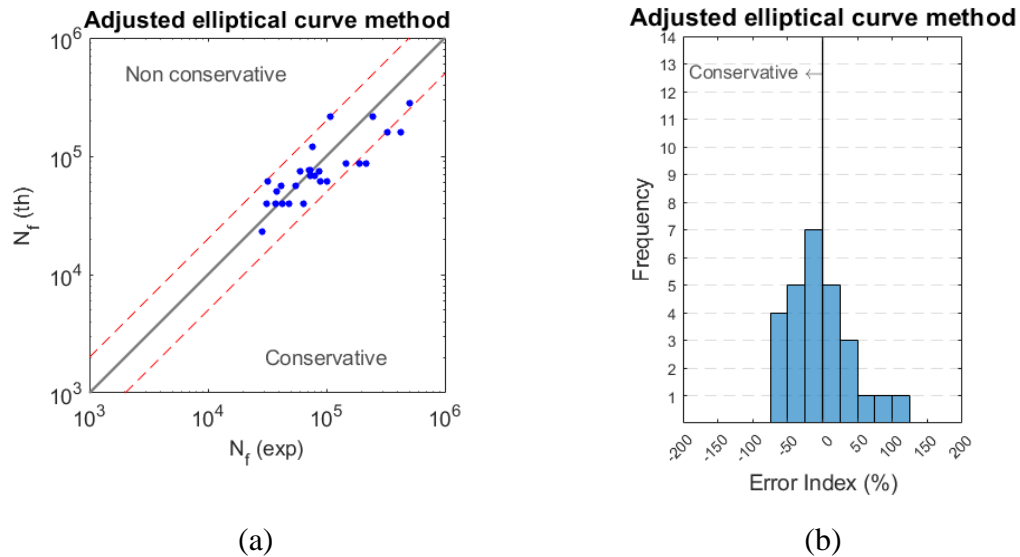


Figure 42 – Life diagram and frequency history relative to the adjusted elliptical curve method

As one may observe, an improvement on the predictions was revealed, as 22 among a total of 27 predictions (81%) were delivered in the scatter band of 2. Such improvement can be clearly perceived in the life diagram (Fig. 42), where the results are well correlated with the diagonal grey line.

The frequency histogram was also revealed to be concise in terms of range, and the majority of the results were concentrated in the -25% to 0% range, which is seen as an improvement over the other frequency histograms, where the models either predominantly delivered error indices within the -75% to -50% range (E, F, M, S&L and P) or presented higher levels of scattering (C&S and McD). Regarding the analysis presented in Fig. 38, the adjusted model delivered 12 occurrences (44%) within the conservative half of the scatter band, as well as 20 occurrences (74%) within the  $\pm 50\%$  central range. In terms of statistics (Table 12), the adjusted elliptical curve method presented an average of error indices corresponding to -4%, which is seen to be a very good result. The proximity of that average to the ideal value of 0% was associated with an increase to the standard deviation.

Table 12 – Statistics relative to the adjusted version of the elliptical curve method

	Avg (%)	StdDev (%)	Min (%)	Median (%)	Max (%)	Range (%)
Adjusted E	-4	43	-62	-13	102	164

## 6. Conclusions

Based on what is presented within this work, the following conclusions can be drawn:

- A direct relationship between fatigue life and normal and shear stress amplitudes,  $\sigma_a$  and  $\tau_a$ , in fully reversed cyclic loading was developed. Accordingly, for a given number of cycles to failure,  $(\sigma_a, \tau_a)$  combinations leading to the same fatigue life should pertain to an elliptical curve in the  $\sigma_a \times \tau_a$  plane.
- Specimens of a DIN 42CrMo4 steel were tested under a selected number of combined synchronous sinusoidal fully reversed normal and shear stress loadings and the results obtained indicated a fair agreement with the fatigue life predictions made by the elliptical curve method.
- Compared to a number of critical plane-based criteria applied to the same steel, the elliptical curve method is seen to possess a better predictability. In addition, it is much simpler to apply as it does not require prior determination of the critical plane.
- The proposed elliptical curve method was found to present a tendency towards conservativeness for loading conditions located at central parts of the elliptical arc. An adjusting parameter, which is a function of the  $\tau_a/\sigma_a$  ratio, is therefore proposed with the purpose of attenuating such a tendency, giving rise to an adjusted version of the method. The adjusted version of the elliptical curve method delivered 81% of its predictions within the scatter band determined by a factor of 2.

## References

- [1] J. Schijve, *Fatigue of structures and materials*. Delft: Springer, 2009. doi: 10.1007/978-1-4020-6808-9.
- [2] S. Suresh, *Fatigue of Materials*. 1998. doi: 10.1017/cbo9780511806575.
- [3] Y. Liu and S. Mahadevan, “Multiaxial high-cycle fatigue criterion and life prediction for metals,” *Int. J. Fatigue*, vol. 27, no. 7, pp. 790–800, 2005, doi: 10.1016/j.ijfatigue.2005.01.003.
- [4] Y. S. Garud, “Multiaxial fatigue: a survey of the state-of-the-art,” *J Test Eval*, vol. 9, no. 3, pp. 165–78, 1981.
- [5] I. V. Papadopoulos, P. Davoli, C. Gorla, M. Filippini, and A. Bernasconi, “A comparative study of multiaxial high-cycle fatigue criteria for metals,” *Int. J. Fatigue*, vol. 19, no. 3, pp. 219–235, 1997, doi: 10.1016/S0142-1123(96)00064-3.
- [6] Y. Y. Wang and W. X. Yao, “Evaluation and comparison of several multiaxial fatigue criteria,” *Int. J. Fatigue*, vol. 26, no. 1, pp. 17–25, 2004, doi: 10.1016/S0142-1123(03)00110-5.
- [7] B. R. You and S. B. Lee, “A critical review on multiaxial fatigue assessments of metals,” *Int. J. Fatigue*, vol. 18, no. 4, pp. 235–244, 1996, doi: 10.1016/0142-1123(96)00002-3.
- [8] A. Carpinteri and A. Spagnoli, “Multiaxial high-cycle fatigue criterion for hard metals,” *Int. J. Fatigue*, vol. 23, no. 2, pp. 135–145, 2001, doi: 10.1016/S0142-1123(00)00075-X.
- [9] A. C. de S. G. dos Santos, L. M. Carvalho, C. F. de Souza, A. da C. Reis, and A. E. B. Freitag, “Total Quality Management: the case of an electricity distribution company,” *Brazilian J. Oper. Prod. Manag.*, vol. 16, pp. 53–65, 2019, doi: <https://doi.org/10.14488/bjopm.2019.v16.n1.a5>.
- [10] W. N. Findley, “A Theory for the Effect of Mean Stress on Fatigue of Metals Under Combined Torsion and Axial Load or Bending,” *J. Eng. Ind.*, vol. 81, no. 4, pp. 301–305, 1959, doi: 10.1115/1.4008327.

- [11] T. Matake, “Explanation on Fatigue Limit Under Combined Stress.,” *Bull JSME*, vol. 20, no. 141, pp. 257–264, 1977, doi: 10.1299/jsme1958.20.257.
- [12] D. L. McDiarmid, “Fatigue Under Out-of-Phase Bending and Torsion,” *Fatigue Fract. Eng. Mater. Struct.*, vol. 9, no. 6, pp. 457–475, 1987, doi: 10.1111/j.1460-2695.1987.tb00471.x.
- [13] L. Susmel and P. Lazzarin, “A bi-parametric Wöhler curve for high cycle multiaxial fatigue assessment,” *Fatigue Fract. Eng. Mater. Struct.*, vol. 25, no. 1, pp. 63–78, 2002, doi: 10.1046/j.1460-2695.2002.00462.x.
- [14] A. Carpinteri, A. Spagnoli, S. Vantadori, and C. Bagni, “Structural integrity assessment of metallic components under multiaxial fatigue: The C-S criterion and its evolution,” *Fatigue Fract. Eng. Mater. Struct.*, vol. 36, no. 9, pp. 870–883, 2013, doi: 10.1111/ffe.12037.
- [15] O. Gonzalez and A. Stuart, *A first course in continuum mechanics*, 1st editio. Cambridge, New York: Cambridge University Press, 2008.
- [16] H. Anton and C. Rorres, *Elementary linear algebra: Applications Version*, 11th editi. 2013.
- [17] A. Howard and C. Rorres, *Elementary Linear Algebra Applications Version*, 8th Ed. John Wiley & Sons, Inc, 2000.
- [18] J. Stewart, *Essential Calculus: Early Transcendentals*. 2012.
- [19] M. Gurtin, *An Introduction to Continuum Mechanics*. New York, 1981.
- [20] G. E. Dieter and D. Bacon, *Mechanical metallurgy SI Metric Edition*. 1988.
- [21] O. H. Basquin, “The exponential law of endurance tests,” in *Proceedings of the American Society for Testing and Materials*, 1910, pp. 625–630.
- [22] N. E. Dowling, K. S. Prasad, and R. Narayanasamy, *Mechanical Behavior of Materials*, 4th editio. 2013.
- [23] T. L. Castro, M. V. S. Pereira, and F. A. Darwish, “On the Influence of Mean Shear Stress on Multiaxial High Cycle Fatigue of Metallic Materials,” *Mater. Res.*, vol.

- 24, no. 1, p. 20200319, 2021, doi: 10.1590/1980-5373-MR-2020-0319.
- [24] P. V. S. Machado, L. C. Araújo, M. V. Soares, L. Reis, and J. A. Araújo, “Multiaxial fatigue assessment of steels with non-metallic inclusions by means of adapted critical plane criteria,” *Theor. Appl. Fract. Mech.*, vol. 108, no. March, p. 102585, 2020, doi: 10.1016/j.tafmec.2020.102585.
- [25] G. B. Marquis and D. F. Socie, *Multiaxial Fatigue*. SAE International, 2000. doi: 10.1016/B0-08-043749-4/04030-1.
- [26] J. A. Araújo, A. P. Dantas, F. C. Castro, E. N. Mamiya, and J. L. A. Ferreira, “On the characterization of the critical plane with a simple and fast alternative measure of the shear stress amplitude in multiaxial fatigue,” *Int. J. Fatigue*, vol. 33, no. 8, pp. 1092–1100, 2011, doi: 10.1016/j.ijfatigue.2011.01.002.
- [27] A. Gil, J. Segura, and N. M. Temme, *Numerical Methods for Special Functions*, 1st Editio. Society for Industrial and Applied Mathematics, 2008.
- [28] H. J. Gough and H. V. Pollard, “The strength of metals under combined alternating stresses,” in *Proceedings of the Institute of Mechanical Engineers, Vol 131*, 1935, pp. 3–103. doi: 10.1243/PIME\_PROC\_1935\_131\_008\_02.
- [29] H. J. Gough, “Engineering Steels Under Combined Cyclic and Static Stresses,” *J. Appl. Mech.*, vol. 17, no. 2, pp. 113–125, Jun. 1950, doi: 10.1115/1.4010088.
- [30] ASTM E446-15, “Standard Practice for Conducting Force Controlled Constant Amplitude Axial Fatigue Tests of Metallic Materials.” ASTM International, 2015.
- [31] M. Pawlenka, M. Mahdal, J. Tůma, and A. Bureček, “Application of a bandpass filter for the active vibration control of high-speed rotors,” *Int. J. Acoust. Vib.*, vol. 24, no. 3, pp. 608–615, 2019, doi: 10.20855/ijav.2019.24.31515.
- [32] A. S. Sedra and K. C. Smith, *Microelectronics*, 4th editio. Oxford University Press Inc, 1998.

## Appendix I – Exemplifying the use of critical plane-based criteria

Assume a specimen (DIN 42CrMo4 steel) subjected to combined fully reversed sinusoidal normal and shear stresses, as presented in Fig. 43(a) and (b). The stress amplitudes  $\sigma_a$  and  $\tau_a$  both correspond to 100 MPa, with a phase difference  $\beta$  of  $90^\circ$ .

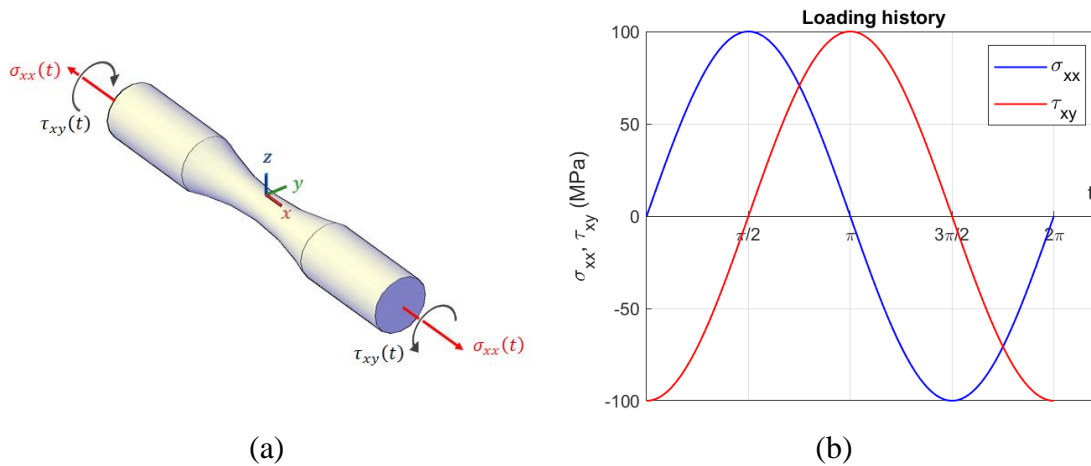


Figure 43 – (a) Specimen subjected to normal and shear stresses; (b) loading history

### Determining $C_a$ and $N_{max}$ for Matake, McDiarmid and S&L

As discussed in section 2.4.2.3, stresses acting on any material plane  $\Delta$  can be determined in terms of  $\sigma_a$  and  $\tau_a$ ,  $\sigma_m$ ,  $\tau_m$  and  $\beta$  using expressions (119)-(125) for the case of combined normal and shear sinusoidal stresses. Given the periodicity of the auxiliary functions  $f$ ,  $g$ ,  $p$  and  $q$ , it is clear that  $C_a$  attains its maximum values when  $\theta$  corresponds to  $45^\circ$ ,  $90^\circ$  and  $135^\circ$ , allowing one to restrict the inspection for candidate planes to such values of  $\theta$ .

With respect to  $\varphi$ , inspecting material planes in every  $1^\circ$ - $5^\circ$  usually generally delivers good results. For this particular example, steps of  $\Delta\varphi$  corresponding to  $5^\circ$  were selected.

Table 13 presents the quantities of interest  $C_a$  and  $N_{max}$  for all the considered material planes, where candidate planes (which maximise  $C_a$ ) are identified.

Table 13 – Quantities of interest acting on material planes

$\theta$ (°)	$\varphi$ (°)	$C_a$ (MPa)	$N_{max}$ (MPa)
45	0	70.71	50.00
45	5	70.18	50.37
45	10	68.61	51.42
45	15	66.17	52.93
45	20	63.17	54.61
45	25	60.25	56.16
45	30	58.33	57.28
45	35	57.74	57.73
45	40	58.07	57.32
45	45	58.96	55.90
45	50	60.22	53.40
45	55	61.74	49.78
45	60	63.44	45.07
45	65	65.21	39.33
45	70	66.93	32.67
45	75	68.46	25.22
45	80	69.67	17.17
45	85	70.44	8.69
45	90	70.71	0.00
45	95	70.44	8.69
45	100	69.67	17.17
45	105	68.46	25.22
45	110	66.93	32.67
45	115	65.21	39.33
45	120	63.44	45.07
45	125	61.74	49.78
45	130	60.22	53.40
45	135	58.96	55.90
45	140	58.07	57.32
45	145	57.74	57.73
45	150	58.33	57.28
45	155	60.25	56.16
45	160	63.17	54.61
45	165	66.17	52.93
45	170	68.61	51.42
45	175	70.18	50.37
90	0	100.00	100.00
90	5	98.86	100.75
90	10	95.51	102.84
90	15	90.14	105.85
90	20	83.07	109.22
90	25	74.83	112.32
90	30	66.14	114.56
90	35	58.11	115.47
90	40	52.21	114.64
90	45	50.00	111.80
90	50	52.21	106.80
90	55	58.11	99.56
90	60	66.14	90.14
90	65	74.83	78.66
90	70	83.07	65.33
90	75	90.14	50.45
90	80	95.51	34.33
90	85	98.86	17.38

$\theta$ (°)	$\varphi$ (°)	$C_a$ (MPa)	$N_{max}$ (MPa)
90	90	100.00	0.00
90	95	98.86	17.38
90	100	95.51	34.33
90	105	90.14	50.45
90	110	83.07	65.33
90	115	74.83	78.66
90	120	66.14	90.14
90	125	58.11	99.56
90	130	52.21	106.80
90	135	50.00	111.80
90	140	52.21	114.64
90	145	58.11	115.47
90	150	66.14	114.56
90	155	74.83	112.32
90	160	83.07	109.22
90	165	90.14	105.85
90	170	95.51	102.84
90	175	98.86	100.75
135	0	70.71	50.00
135	5	70.18	50.37
135	10	68.61	51.42
135	15	66.17	52.93
135	20	63.17	54.61
135	25	60.25	56.16
135	30	58.33	57.28
135	35	57.74	57.73
135	40	58.07	57.32
135	45	58.96	55.90
135	50	60.22	53.40
135	55	61.74	49.78
135	60	63.44	45.07
135	65	65.21	39.33
135	70	66.93	32.67
135	75	68.46	25.22
135	80	69.67	17.17
135	85	70.44	8.69
135	90	70.71	0.00
135	95	70.44	8.69
135	100	69.67	17.17
135	105	68.46	25.22
135	110	66.93	32.67
135	115	65.21	39.33
135	120	63.44	45.07
135	125	61.74	49.78
135	130	60.22	53.40
135	135	58.96	55.90
135	140	58.07	57.32
135	145	57.74	57.73
135	150	58.33	57.28
135	155	60.25	56.16
135	160	63.17	54.61
135	165	66.17	52.93
135	170	68.61	51.42
135	175	70.18	50.37

Candidate planes are summarised in Table 14, where both planes experience a shear stress amplitude  $C_a$  of 100 MPa. Nevertheless, in one case  $N_{max}$  corresponds to 100 MPa, while, in the other,  $N_{max}$  corresponds to nil. As such, the first  $(\theta, \varphi)$  combination is the one associated with the critical plane.

Table 14 – Critical plane selection among pre-selected set of candidate planes for Matake, McDiarmid and Susmel & Lazzarin

$\theta$ (°)	$\varphi$ (°)	$C_a$ (MPa)	$N_{max}$ (MPa)	
90	0	100	100	✓
90	90	100	0	✗

It is worth mentioning that, in some cases, there may be more than one critical plane. For instance, specimens subjected to pure torsion with a shear stress amplitude corresponding to the fatigue resistance limit in shear  $t_{-1}$  result in two candidate planes where both planes are critical (Table 15). Fig. 44 presents the orientation of such planes relative to the specimen axes and to its free surface, where the  $x$ -axis corresponds to the longitudinal direction of the specimen.

Table 15 – Critical plane selection among pre-selected set of candidate planes for Matake, McDiarmid and Susmel & Lazzarin

$\theta$ (°)	$\varphi$ (°)	$C_a$ (MPa)	$N_{max}$ (MPa)	
90	0	$t_{-1}$	0	✓
90	90	$t_{-1}$	0	✓

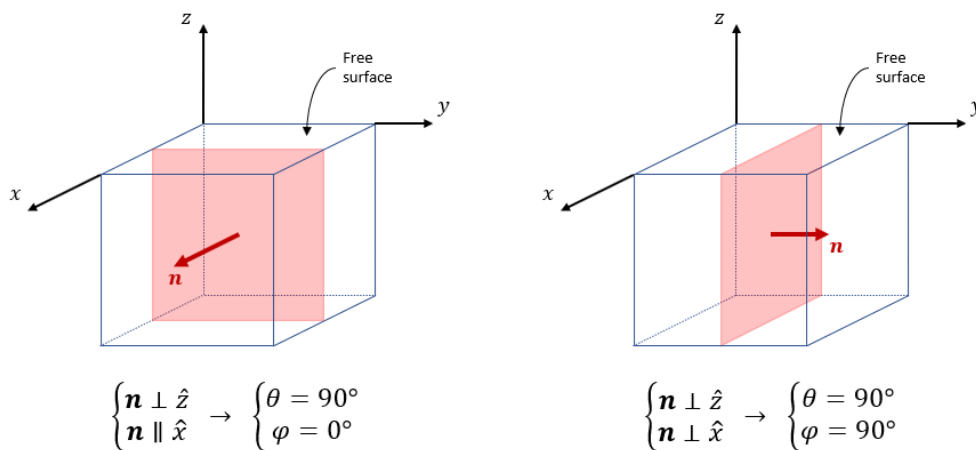


Figure 44 – Orientation of critical planes in pure torsion

Another example is the case where specimens are subjected to uniaxial push-pull with a stress amplitude corresponding to the fatigue resistance limit,  $f_{-1}$ . This results in four candidate planes (Table 16), where all of them are critical. Fig. 45 presents the orientation of such planes relative to the specimen axes and to its free surface, where the  $x$ -axis corresponds to the longitudinal direction of the specimen.

Table 16 – Critical plane selection among pre-selected set of candidate planes for Matake, McDiarmid and Susmel & Lazzarin

$\theta$ ( $^{\circ}$ )	$\varphi$ ( $^{\circ}$ )	$C_a$ (MPa)	$N_{max}$ (MPa)	
45	0	$f_{-1}/2$	$f_{-1}/2$	✓
90	45	$f_{-1}/2$	$f_{-1}/2$	✓
90	135	$f_{-1}/2$	$f_{-1}/2$	✓
135	0	$f_{-1}/2$	$f_{-1}/2$	✓

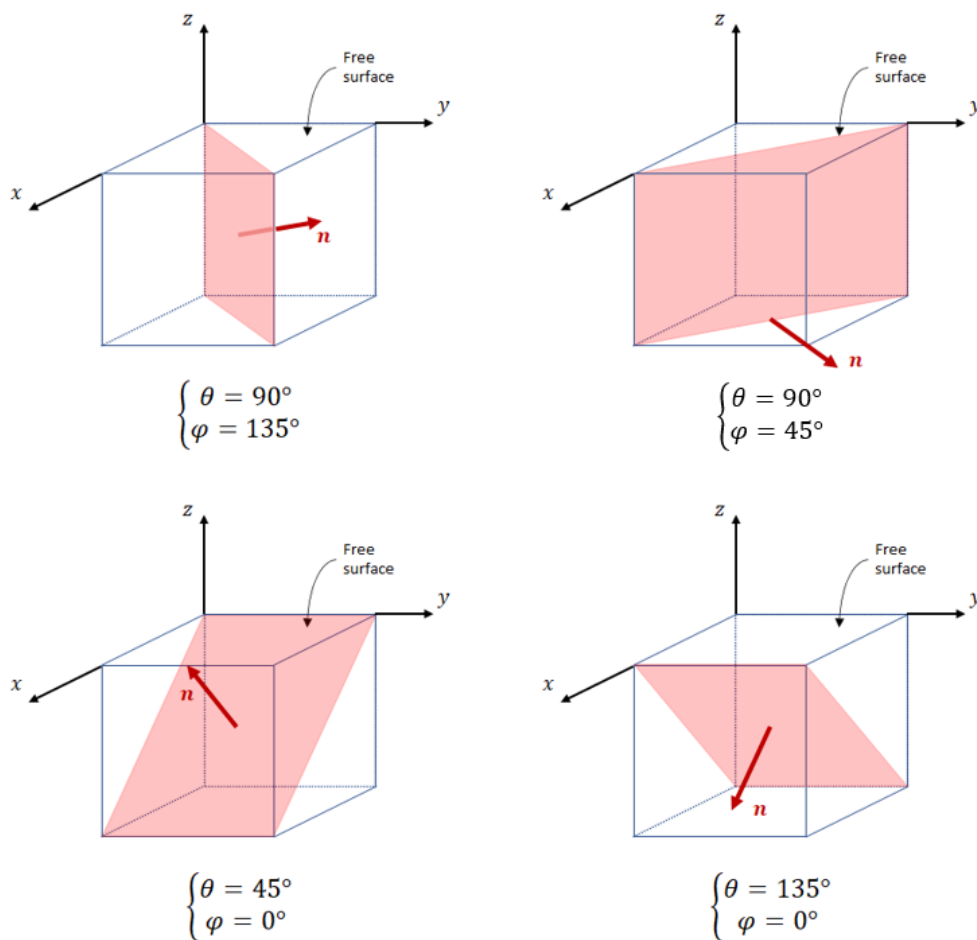


Figure 45 – Orientation of critical planes in uniaxial push-pull

### Additional comment on Matake

Matake's expression  $C_a + \mu N_{max} = t_{-1}$  establishes a linear relation between  $C_a$  and  $N_{max}$ , where both quantities act on the critical plane. Given that the examples above (pure torsion and push-pull) provide two combinations of  $(N_{max}, C_a)$ , one may plot the linear relation establishing a boundary between the safe and unsafe regions, which is useful for assessing the fatigue behaviour of a component in light of the infinite fatigue-life concept. Fig. 46 presents a plot relative to Matake's criteria applied to the loading condition shown in Fig. 43.

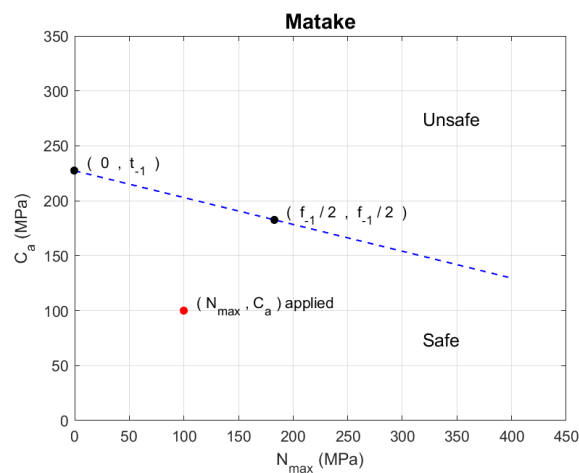


Figure 46 – Matake criterion applied to the loading condition presented in Fig. 43

Finally, by determining  $C_a$  and  $N_{max}$ , one may directly substitute such values in expressions (158)-(160), which correspond to the adapted versions of Matake, McDiarmid and Susmel & Lazzarin aiming to predict fatigue-life.

### Determining $C_a$ and $N_{max}$ for Findley

For the case where plane-stress is applied, at least one occurrence of critical plane is expected to occur at  $\theta$  corresponding to  $90^\circ$ . In the event of multiple critical planes, stress levels do not vary from one critical plane to another, meaning that one obtains the desired values of  $C_a$  and  $N_{max}$  if one of the critical planes is found. This allows one to restrict the inspection for critical planes to those that are perpendicular to the free surface of the specimen ( $\theta$  corresponding to  $90^\circ$ ).

For values of  $f_{-1}$  and  $t_{-1}$  respectively corresponding to 365.44 MPa and 227.34 MPa, the constant  $k$  can be determined via expression (131), which turns out to be 0.2518. Shear stress amplitude  $C_a$  and maximum value of the normal stress  $M_{max}$  were computed for a set of material planes, considering increments of  $\Delta\varphi$  of  $5^\circ$ .

In regard to the loading condition presented in Fig. 43, quantities of interest relative to Findley's criterion are presented in Table 17. A fifth column relative to Findley's fatigue damage parameter  $C_a + kN_{max}$  was included. Critical planes correspond to those where the fatigue damage parameter attains its maximum value.

Table 17 – Critical plane selection for Findley



$\theta$ ( $^\circ$ )	$\varphi$ ( $^\circ$ )	$C_a$ (MPa)	$N_{max}$ (MPa)	$C_a + kN_{max}$ (MPa)
90	0	100	100	125.1823
90	5	98.86277	100.7482	124.2334
90	10	95.51265	102.8387	121.4098
90	15	90.13878	105.8543	116.7953
90	20	83.07335	109.2202	110.5775
90	25	74.82526	112.317	103.1092
90	30	66.14378	114.5644	94.99369
90	35	58.11483	115.4676	87.19219
90	40	52.21257	114.6389	81.08126
90	45	50	111.8034	78.15463
90	50	52.21257	106.797	79.10648
90	55	58.11483	99.56187	83.18676
90	60	66.14378	90.13878	88.84277
90	65	74.82526	78.65903	94.63338
90	70	83.07335	65.3345	99.52605
90	75	90.13878	50.44673	102.8424
90	80	95.51265	34.33468	104.1589
90	85	98.86277	17.38142	103.2398
90	90	100	0	100
90	95	98.86277	17.38142	103.2398
90	100	95.51265	34.33468	104.1589
90	105	90.13878	50.44673	102.8424
90	110	83.07335	65.3345	99.52605
90	115	74.82526	78.65903	94.63338
90	120	66.14378	90.13878	88.84277
90	125	58.11483	99.56187	83.18676
90	130	52.21257	106.797	79.10648
90	135	50	111.8034	78.15463
90	140	52.21257	114.6389	81.08126
90	145	58.11483	115.4676	87.19219
90	150	66.14378	114.5644	94.99369
90	155	74.82526	112.317	103.1092
90	160	83.07335	109.2202	110.5775
90	165	90.13878	105.8543	116.7953
90	170	95.51265	102.8387	121.4098
90	175	98.86277	100.7482	124.2334

Accordingly, by encountering the critical plane, one obtains the associated values of  $C_a$  and  $N_{max}$ , which can be directly substituted into expression (157) for fatigue-life predicting.

Determining  $C_a$  and  $N_{max}$  for Carpinteri & Spagnoli

Application of the C&S model first requires determining fracture plane orientation. For combined sinusoidal normal and shear stresses, at least one fracture plane is expected to take place at  $\theta$  corresponding to  $90^\circ$ , once again allowing one to restrict the inspection for  $\theta = 90^\circ$ .

In regard to the loading condition presented in Fig. 43, Table 18 presents the stress levels computed for a number of material planes, considering steps of  $\Delta\varphi$  of  $5^\circ$ , where fracture planes (the ones that experience the maximum value of  $N_{max}$ ) are identified.

Table 18 – Fracture plane selection for C&S

$\theta$ ( $^\circ$ )	$\varphi$ ( $^\circ$ )	$C_a$ (MPa)	$N_{max}$ (MPa)
90	0	100	100
90	5	98.86277	100.7482
90	10	95.51265	102.8387
90	15	90.13878	105.8543
90	20	83.07335	109.2202
90	25	74.82526	112.317
90	30	66.14378	114.5644
90	35	58.11483	115.4676
90	40	52.21257	114.6389
90	45	50	111.8034
90	50	52.21257	106.797
90	55	58.11483	99.56187
90	60	66.14378	90.13878
90	65	74.82526	78.65903
90	70	83.07335	65.3345
90	75	90.13878	50.44673
90	80	95.51265	34.33468
90	85	98.86277	17.38142
90	90	100	0
90	95	98.86277	17.38142
90	100	95.51265	34.33468
90	105	90.13878	50.44673
90	110	83.07335	65.3345
90	115	74.82526	78.65903
90	120	66.14378	90.13878
90	125	58.11483	99.56187
90	130	52.21257	106.797
90	135	50	111.8034
90	140	52.21257	114.6389
90	145	58.11483	115.4676
90	150	66.14378	114.5644
90	155	74.82526	112.317
90	160	83.07335	109.2202
90	165	90.13878	105.8543
90	170	95.51265	102.8387
90	175	98.86277	100.7482

The two occurrences of fracture planes were summarised in Table 19. Such planes are symmetrical with respect to the specimen's longitudinal axis, where the first occurrence corresponds to  $\varphi_{f,1} = 35^\circ$  while the second corresponds to  $\varphi_{f,2} = 145^\circ$ , as shown in Fig. 47. The orientation of the second fracture plane can be equivalently obtained with  $\varphi$  corresponding to  $-35^\circ$ , evidencing the above-mentioned symmetry.

Table 19 – Critical plane selection for C&S

$\theta$ ( $^\circ$ )	$\varphi$ ( $^\circ$ )	$C_a$ (MPa)	$N_{max}$ (MPa)
90	35	100	100
90	145	100	100

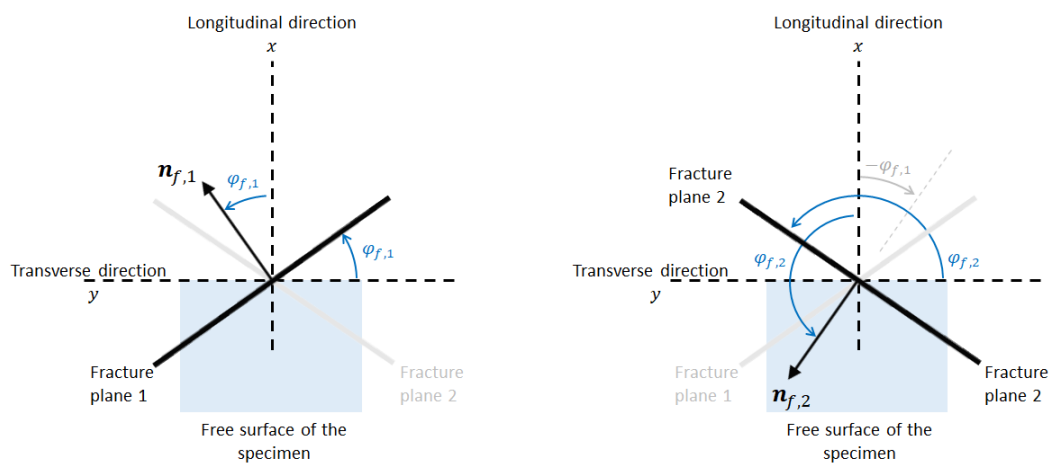


Figure 47 – Illustration of the fracture planes, where the second can also be described in terms of  $-\varphi_{f,1}$

Critical and fracture plane differ in their orientation by an angle  $\delta$ , which is determined via expression (136). For the DIN 42CrMo4 steel in question,  $\delta$  corresponds to  $41.377^\circ$ .

Orientation of the first critical plane  $\varphi_{c,1}$  is straightforwardly obtained by adding  $\delta$  to  $\varphi_{f,1}$ , as given by expression (137). Nevertheless, in order to maintain symmetrical consistency with the first critical plane, the orientation of the second critical plane  $\varphi_{c,2}$  is thus obtained by subtracting  $\delta$  out of  $\varphi_{f,2}$ , as shown in Fig. 48. In this illustration, a dog-bone specimen is presented where normal vectors relative to fracture and critical planes are omitted for better visualisation. Nevertheless, the rationale is the same.

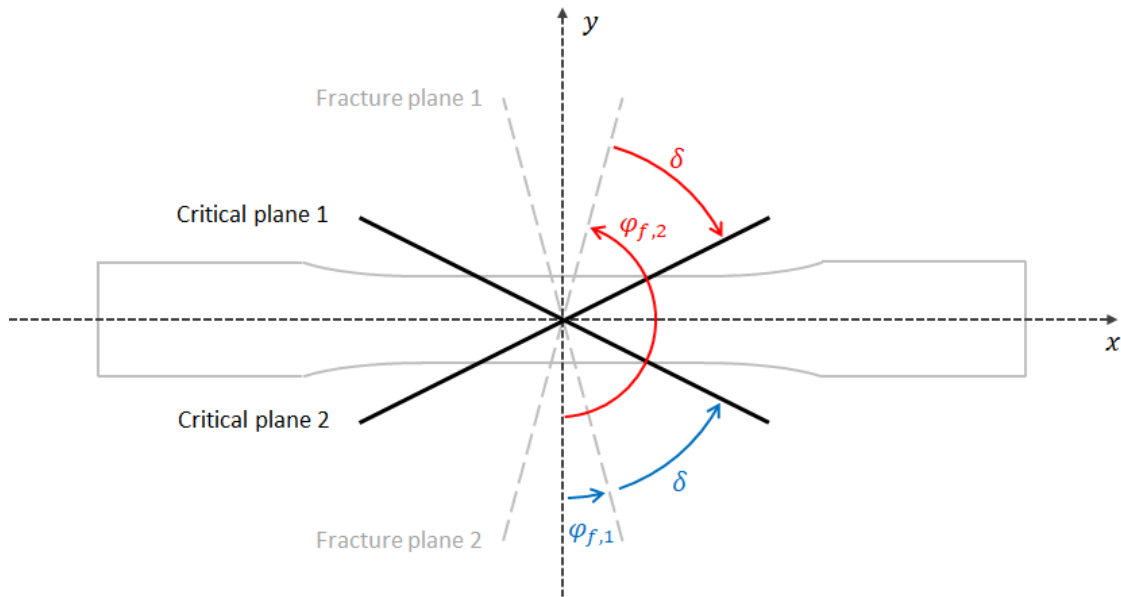


Figure 48 – Critical planes for C&amp;S

Critical plane orientations are therefore given by  $\varphi_{c,1}$  and  $\varphi_{c,2}$ , which correspond to  $76.377^\circ$  and  $103.623^\circ$ , leading to 100 MPa for both  $C_a$  and  $N_{max}$ . Such planes are therefore listed in Table 20.

Table 20 – Critical plane selection for C&amp;S

$\theta$ (°)	$\varphi$ (°)	$C_a$ (MPa)	$N_{max}$ (MPa)
90	76.377	100	100
90	103.623	100	100

Accordingly, by encountering the critical plane, one obtains the associated values of  $C_a$  and  $N_{max}$ , which can be directly substituted into expression (163) for fatigue-life predicting.